JAGIELLONIAN UNIVERSITY
FACULTY OF PHYSICS, ASTRONOMY
AND APPLIED COMPUTER SCIENCE
INSTITUTE OF PHYSICS

Diploma Thesis

Measurement of the neutral kaon regeneration cross-section in beryllium at P=110 MeV/c with the KLOE detector

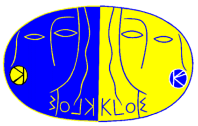

Izabela Balwierz

supervised by

prof. Paweł Moskal

CRACOW 2011

Abstract

The main result of this thesis is determination of the neutral kaon regeneration cross-section in beryllium for momentum of $p_K \approx 110$ MeV/c. It was obtained by analyzing data for $K_L \to K_S$ regeneration in the cylindrical beam pipe of the KLOE detector. The corresponding cross-sections for the KLOE drift chamber inner wall and the spherical beam pipe were also evaluated as well as values for aluminium and carbon. The K_L mesons were produced in the center of the detector in the collision region of e^+ and e^- beams of the DAΦNE collider that worked at the ϕ meson resonance peak. The analysis was based on identification of regenerated events $e^+e^- \to \phi \to K_S K_L \to \pi^+\pi^- K_S^{reg} \to \pi^+\pi^-\pi^+\pi^-$ and their extraction from the distributions of the vertex position of the K_L meson decays into $\pi^+\pi^-$. The regeneration cross-sections were determined based on the extracted number of regenerated events and number of the K_L mesons passing through the regenerator. Obtained results are equal to: $\sigma_{reg}^{Be} = (50.0 \pm 0.7^{stat} \pm 5.0^{syst})$mbarn for beryllium, $\sigma_{reg}^{BP} = (77.6 \pm 0.3^{stat} \pm 7.8^{syst})$mbarn for the beam pipe, $\sigma_{reg}^{DC} = (75.7 \pm 0.3^{stat} \pm 7.6^{syst})$mbarn for the drift chamber inner wall, $\sigma_{reg}^{Al} = (170 \pm 3^{stat} \pm 38^{syst})$mbarn for aluminium and $\sigma_{reg}^{C} = (61 \pm 1^{stat} \pm 11^{syst})$mbarn for carbon.

This thesis is dedicated to the memory of my two physics teachers:
R.I.P. Ph.D Jerzy Mucha
and R.I.P. M.Sc. Ryszard Zapała.

Acknowledgment

I would like to thank everybody who helped me during writing of this thesis and who had influence on its shape.

I am greatly indebted to R.I.P. Jerzy Mucha and Ryszard Zapała to whose memory this thesis is dedicated. I owe my decision to study physics to them and much more. I wish they could read this thesis.

I am extremely grateful to prof. Paweł Moskal for his invaluable help, suggestions, for immense patience in correcting this thesis and many other countless things.

I am greatly indebted to Antonio Di Domenico, Antonio De Santis, Erica De Lucia, Eryk Czerwiński, Wojciech Wiślicki and the whole KLOE and KLOE-2 collaboration for guiding me through the analysis.

I would like to express my appreciation to Fabio Bossi and Caterina Bloise for making it possible for me to work in the KLOE experiment and to visit Frascati.

I would like to also thank Jerzy Smyrski, Jarosław Zdebik, Marcin Zieliński and Wojciech Krzemień for hints and help during our group meetings.

I also thank Magdalena Skurzok, Michał Silarski, Tomasz Twaróg, Tomasz Bednarski and Szymon Niedźwiecki for great atmosphere during the last two years working in the Nuclear Physics Division of the Jagiellonian University.

Many thanks are due to my colleagues Małgorzata Mochol, Ada Umińska, Monika Josiekova, Sylvia Święcicki, Piotr Warchoł, Marcin Wysokiński and Karol Dąbrowski for great time spent during my whole studies.

I also thank my friends Katarzyna Galas, Agnieszka Dudziak and Anna Mielnikow on whom I could always rely during our long friendship.

I would like to express my appreciation to my parents, grandmothers, brother and sister for support they provided to me through my entire life.

Last but not least, I would like to thank Rafał Pytko for being always close to me.

"There are no stupid questions. There are only stupid answers."

Ph.D. Jerzy Mucha (1942 – 2010)

"You have to care for the friendship because you will not meet many people to whom you might give it."

M.Sc. Ryszard Zapała (1952 – 2008)

Contents

1. Introduction

Search for physics beyond the Standard Model and deviations from Quantum Mechanics enables to better understand the world of particles. Due to this fact, in many particle physics laboratories around the world, experiments aiming at testing basic principles of these theories and underlying discrete symmetries (C, P, CP, CPT) are intensively conducted.

One of these institutes is Laboratori Nazionali di Frascati (LNF) located in Italy near Rome, where the KLOE experiment operating at the DAΦNE collider was taking data during 1999-2006 years. Physics program of the KLOE experiment comprised also investigation of decays and temporal evolution of quantum entangled pairs of kaons produced in the ϕ meson decay. The KLOE detector permitted observing a variety of unique interference phenomena in the production and decay of neutral kaons. Such observations enable to test the linear superposition principle of quantum mechanics, the interplay of different conservation laws and the validity of various symmetry principles.

For this purpose, the DAΦNE e^+e^- accelerator was designed to work at the ϕ resonance peak. The total number of neutral kaon pairs produced during its operating was $\sim 8 \cdot 10^9$. Now the upgraded experiment, KLOE-2 [14], is about to start working at the same place.

Parameters that test quantum mechanics at KLOE are, among others, the decoherence and CPT violation parameters [10]: ζ_{00}, ζ_{SL}, γ, $\Re e(\omega)$ and $\Im m(\omega)$. They have been measured at KLOE using interferometric methods by fitting the theoretical function to the distribution of the difference of the decay times (Δt) between $CP-$violating decays of K_L ($K_L \to \pi^+\pi^-$) and K_S decays into two charged pions in $\phi \to K_L K_S \to \pi^+\pi^-\pi^+\pi^-$ reaction chain (Fig. 1.1). The uncertainties on this measurements were dominated by the statistical error. At KLOE-2 the statistical error on this parameters can be reduced by a factor of 10 because of about ten times higher luminosity and new detector close to the interaction point: Inner Tracker [13]. The uncertainties in this case will be dominated by the systematic errors.

One of the main sources of these systematic errors is due to the poor knowledge of the incoherent regeneration in the cylindrical beam pipe made of beryllium. In particular, for the measurement of the parameter $\Im m(\omega)$ this will be by far the dominant source of systematic uncertainty. This is due to the fact that when regeneration occurs, the K_L meson changes into the K_S meson that almost immediately decays into $\pi^+\pi^-$ ($K_L \to K_S \to \pi^+\pi^-$) that disturbs the measurement of $K_L K_S \to \pi^+\pi^-\pi^+\pi^-$ decays.

The cylindrical beam pipe is located ~ 4.4 cm from the interaction point, where neutral kaons are produced, and this distance corresponds to ~ 7 life times of K_S (τ_S). Another regenerator that has an influence on the region in which the fit was performed is the spherical beam pipe made of alloy of beryllium and aluminium. It has a radius of ~ 10 cm that corresponds to $\sim 17\tau_S$. The enhancement in the number of counts for $K_L K_S \to$

$\pi^+\pi^-\pi^+\pi^-$ decays, originating from regeneration ($K_L \to K_S \to \pi^+\pi^-$) in the spherical beam pipe is visible in the left panel of Fig. 1.1 as a peak around $17\tau_S$. In the right panel of Fig. 1.1 the most sensitive region for decoherence is shown, where the first regenerator (around $7\tau_S$) has its impact. There is also third regenerator which is the cylindrical drift chamber inner wall, situated ~ 25 cm from the ϕ meson decay point and made of carbon and aluminium. All of these materials are disturbing the $K_L K_S \to \pi^+\pi^-\pi^+\pi^-$ measurement and hence, studying the regeneration is crucial for improving the systematic precision in deriving of decoherence and $CPT-$violating parameters.

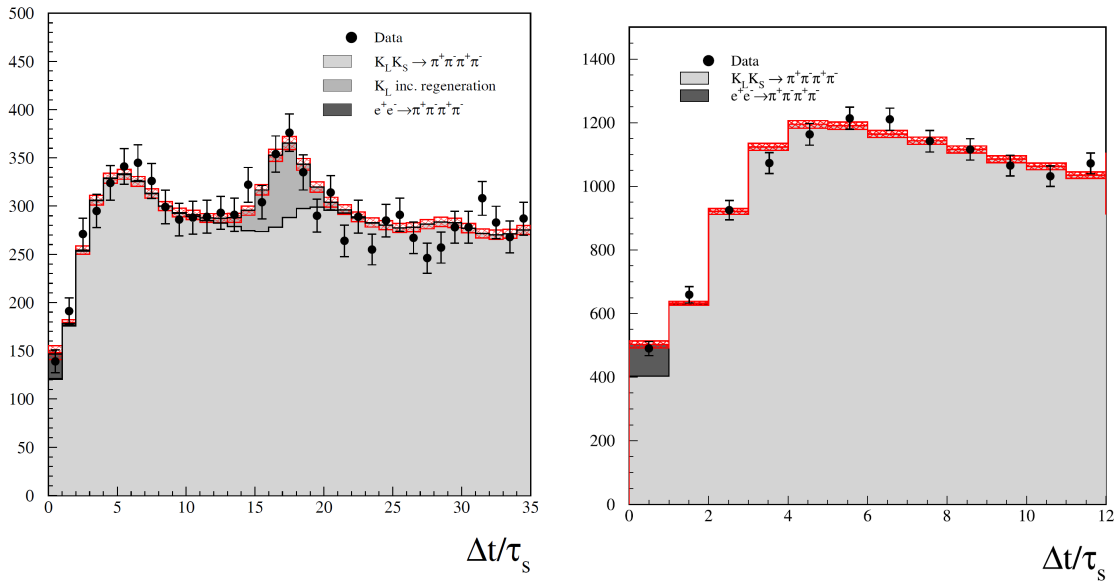

Figure 1.1: Fit to Δt distribution of the events $\phi \to K_L K_S \to \pi^+\pi^-\pi^+\pi^-$. In the left panel the region sensitive to both beam pipe regenerators is shown, whereas in the right panel the decoherence region is presented. The left figure is adapted from [15] and the right one from [16].

However, there is a lack of experimental data for K_S regeneration at low momenta, especially in the KLOE range ($p_K \approx 110$ MeV/c). In particular the only existing measurement in beryllium at this momentum value was performed in 1998 by the CMD-2 detector but is affected by large errors [39]: $\sigma_{reg}^{Be} = (55.1 \pm 7.7)$mbarn. In 1996 there were made theoretical evaluations of regeneration cross-sections in this momentum range for several materials [38]: $\sigma_{reg}^{Be} = (40.7 \pm 7.9)$mbarn, $\sigma_{reg}^{C} = (44.2 \pm 8.6)$mbarn and $\sigma_{reg}^{Al} = (18.6 \pm 3.6)$mbarn. Interestingly this evaluation predicts an unexpected increase of the regeneration cross-sections of about 20% passing from 100 to 120 MeV/c. In 2006 the first measurements of cross-sections for the KLOE materials were made with the statistics based on luminosity of ~ 328 pb^{-1}. The obtained results were [21]: $\sigma_{reg}^{DC} = (60.2 \pm 0.8^{stat} \pm 6.0^{syst})$mbarn for the drift chamber inner wall material (alluminium and carbon) and $\sigma_{reg}^{BP} = (59.6 \pm 0.6^{stat} \pm 6.0^{syst})$mbarn for the spherical beam pipe material (alluminium and beryllium). However, still the cross-section for the cylindrical beam pipe made solely of beryllium was missing.

The main aim of this thesis is measurement of the neutral kaon regeneration cross-section in beryllium for momentum of $p_K \approx 110$ MeV/c. Also the cross-sections for the

drift chamber inner wall and the spherical beam pipe will be evaluated. Using this results it is possible to estimate the cross-sections for aluminium and carbon and these results will be also presented. The KLOE data sample used in this analysis was collected by the KLOE collaboration in 2004-2005 years and corresponds to ~ 1.7 fb^{-1}, that is, $\sim 5.3 \cdot 10^9$ of ϕ mesons produced.

The thesis is divided into nine chapters. In chapter 2 a brief discussion of the phenomenology and the theoretical aspects of the neutral kaon system is presented. In chapter 3 the DAΦNE collider and the KLOE experiment are described. Next, in chapter 4 the phenomenology of the regeneration phenomena is explained. Chapter 5 is dedicated to the description of the method used to identify a K_L beam and $\phi \to K_S K_L \to \pi^+\pi^-\pi^+\pi^-$ decays. Further, in chapter 6 the general analysis of the regeneration phenomena is presented. Chapter 7 comprises the description of selection of the regeneration signal in order to extract number of regenerated events. Finally, chapter 8 is devoted to determination of the cross-sections. Chapter 9 summarizes the whole thesis and brings the conclusions and remarks.

This work is supplemented with Appendices where section A presents a derivation of a formula for the optical theorem, used to explain the phenomenology of the kaon regeneration. Appendix B describes calculations necessary to evaluate maximal angle for the coherent regeneration. Section C provides an analytical calculations of the impact point of the K_L meson on the regenerator. Appendix D describes generally MonteCarlo methods used to fit the simulated distributions to the data. Section E introduces evaluation of the contributions required to determine the total regeneration cross-section.

2. Physics of neutral kaons at KLOE

2.1 A little from kaon history

The neutral kaon system is one of the most interesting in particle physics and its impact on the development of this scientific area is over 60 years old. Kaons (both neutral and charged ones) were discovered in cosmic ray showers in 1947 by George D. Rochester and Clifford C. Butler [1]. On one photograph from cloud chamber they observed an uncharged elementary particle decaying into two lighter charged particles and, on the second one, charged particle decaying into two light particles, one of which was charged and the other uncharged. They explained this V-shaped tracks as the decays of new heavy particles with estimated mass of about half the proton mass. During the next several years many other observations of "V-particles" were made.

Decay times of this new particles were of the order of 10^{-10} s, characteristic of weak interactions. On the other hand, they were produced much faster, with a time scale of 10^{-23}, typical of strong interactions. Because of this difference in production and decay times, kaons were called "strange" particles. This problem was solved in 1953 by Murray Gell-Mann [2] and Kazuhiko Nishijima [3] who postulated the existence of a new quantum number called *strangeness* (S), conserved in electromagnetic and strong interactions but violated in weak interactions. The strangeness was defined by the following relation:

$$Q = I_3 + \frac{B+S}{2},$$

where Q denotes the electric charge, B the baryon number and I_3 the third component of isospin.

A strange particle cannot decay into any non-strange particle system through interactions that conserve Q, B and I_3. Hence, kaons can decay into particles with $S = 0$ only through weak interactions with a change of S value equal to ± 1. K mesons belong to isospin doublets ($I_3 = \pm\frac{1}{2}$) with strangeness $S = \pm 1$. A doublet with $S = +1$ consists of mesons K^+ ($= u\bar{s}$) and K^0 ($= d\bar{s}$). Their antiparticles, with strangeness $S = -1$, are K^- ($= s\bar{u}$) and $\bar{K}^0$ ($= s\bar{d}$) [5]. What Rochester and Butler observed on their photographs were weak decays of neutral and charged K mesons into:

$$\begin{aligned} K^0(\bar{K}^0) &\rightarrow \pi^+\pi^- \\ K^\pm &\rightarrow \pi^\pm\pi^0. \end{aligned}$$

Strange particles can be produced in pairs via strong interactions of non-strange particles with $\Delta S = 0$, for example:

$$\begin{aligned} \pi^- + p &\rightarrow K^0 + \Lambda \\ \pi^+ + p &\rightarrow K^+ + \bar{K}^0 + p. \end{aligned}$$

In 1955, Murray Gell-Mann and Abraham Pais [4] pointed out that K^0 and $\bar{K}^0$ could transform into each other via weak interaction with intermediate states of pions: $K^0 \leftrightarrow 2\pi \leftrightarrow \bar{K}^0$, $K^0 \leftrightarrow 3\pi \leftrightarrow \bar{K}^0$ ($|\Delta S| = 2$). It means that after some time, in a beam that initially consists of only K^0 pure states, there will be also $\bar{K}^0$ mesons. Since the charge conjugation (C) was supposed to be a valid symmetry for all interactions, Gell-Mann and Pais proposed to represent the kaon decay eigenstates as eigenstates of the operator C. As these eigenstates would decay through different channels, they should have different life times and masses. In particular the state with $C = -1$ would not decay into the 2π state, and would therefore have a longer life time than the state with $C = +1$ [23].

In 1957, Tsung D. Lee and Chen N. Yang [6] suggested experiments testing invariance of weak interaction under space inversion (P) and under charge conjugation (C). It occurred that above symmetries are violated in this interaction. In the same year, Lev Landau [7] proposed the CP symmetry that is combination of space inversion and charge conjugation. Replacing C with CP would not change Gell-Mann and Pais theory. Moreover, in 1964 Christenson, Cronin, Fitch and Turlay [8] announced a discovery of the decay into two pions for the long-lived kaon and by this demonstrated that CP was not conserved in weak interaction. The Branching Ratio (BR) of the CP-violating process $K_L \to \pi^+\pi^-$ was determined to be [8]:

$$BR\Big(\frac{K_L \to \pi^+\pi^-}{K_L \to \text{all}}\Big) = (2.0 \pm 0.4) \cdot 10^{-3}.$$

2.2 The neutral kaon system hamiltonian

The neutral kaon system was already described in many papers, therefore in this thesis only the most important issues are briefly summarized. More interested readers are referred to Ref. [10] and [24], for instance.

The neutral kaons oscillate, with frequency of about 5.3 GHz, between each other, that is between K^0 and $\bar{K}^0$ states. A neutral kaon, at the moment of production, can be described as a superposition of $\left|K^0\right\rangle$ and $\left|\bar{K}^0\right\rangle$:

$$|K(0)\rangle = a(0)\left|K^0\right\rangle + b(0)\left|\bar{K}^0\right\rangle, \tag{2.1}$$

and its time evolution after some time t (in the kaon rest frame) is:

$$|K(t)\rangle = a(t)\left|K^0\right\rangle + b(t)\left|\bar{K}^0\right\rangle + \sum_j c_j(t)\,|f_j\rangle\,. \tag{2.2}$$

Here the sum is made over all possible kaon decay final states $|f_j\rangle$ ($j = 1, 2, ...$), while a, b, c are time-dependent functions; a and b obey the Schrödinger-like equation:

$$i\frac{\partial}{\partial t}\begin{pmatrix} a(t) \\ b(t) \end{pmatrix} = \mathbf{H}\begin{pmatrix} a(t) \\ b(t) \end{pmatrix}, \tag{2.3}$$

where $\mathbf{H}$ is the effective, not hermitian hamiltonian. It can be, however, decomposed into its hermitian and anti-hermitian parts:

$$\mathbf{H} = \begin{pmatrix} H_{11} & H_{12} \\ H_{21} & H_{22} \end{pmatrix} = \mathbf{M} - \frac{i}{2}\mathbf{\Gamma} = \begin{pmatrix} M_{11} & M_{12} \\ M_{21}^* & M_{22} \end{pmatrix} - \frac{i}{2}\begin{pmatrix} \Gamma_{11} & \Gamma_{12} \\ \Gamma_{21}^* & \Gamma_{22} \end{pmatrix}, \tag{2.4}$$

where $\mathbf{M}$ and $\mathbf{\Gamma}$ are two hermitian matrices, called *mass* and *decay* matrices, and 1 and 2 stand for K^0 and $\bar{K}^0$ respectively. The conservation of discrete symmetries constrains the matrix elements of $\mathbf{H}$ so that:

$$\begin{aligned} CPT &: \quad H_{11} = H_{22}, \\ T &: \quad |H_{12}| = |H_{21}|, \\ CP &: \quad H_{11} = H_{22} \quad \text{and} \quad |H_{12}| = |H_{21}|. \end{aligned} \tag{2.5}$$

2.3 Quantum states of kaons

As already mentioned, the neutral kaon system can be described in the strangeness basis:

$$S\left|K^0\right\rangle = +1\left|K^0\right\rangle \qquad \text{and} \qquad S\left|\bar{K}^0\right\rangle = -1\left|\bar{K}^0\right\rangle$$

but this is not suitable for kaon decays, which occur via weak interactions that do not conserve strangeness. The combined CP operation in this basis gives:

$$CP\left|K^0\right\rangle = -\left|\bar{K}^0\right\rangle \qquad \text{and} \qquad CP\left|\bar{K}^0\right\rangle = -\left|K^0\right\rangle.$$

so K^0 and $\bar{K}^0$ are not CP eigenstates. One can see that these eigenstates can be constructed as [11]:

$$\left|K_1^0\right\rangle = \frac{1}{\sqrt{2}}\left[\left|K^0\right\rangle + \left|\bar{K}^0\right\rangle\right], \tag{2.6}$$

$$\left|K_2^0\right\rangle = \frac{1}{\sqrt{2}}\left[\left|K^0\right\rangle - \left|\bar{K}^0\right\rangle\right], \tag{2.7}$$

and hence:

$$CP\left|K_1^0\right\rangle = +\left|K_1^0\right\rangle \qquad \text{and} \qquad CP\left|K_2^0\right\rangle = -\left|K_2^0\right\rangle.$$

It occurs that in order to satisfy CP symmetry, states with $CP = +1$ (K_1^0) can only decay into 2π and states with $CP = -1$ (K_2^0) only into 3π. Decays into two- and three-pions channel have different energy thresholds so these kaon states should also have different decay times. In particular, state decaying into 3π has longer life time than that decaying into 2π.

However, due to weak interactions CP symmetry is violated and kaons decay into physical states which are eigenstates of the effective hamiltonian:

$$H = H_0 + H_w,$$

where H_0 governs the strong and electromagnetic interactions and conserves strangeness while H_w is a small perturbation governing weak interactions and not conserving strangeness.

The eigenvalues of the hamiltonian $\mathbf{H}$ can be derived from:

$$\det\left(\mathbf{H} - \lambda\mathbf{1}\right) = 0, \tag{2.8}$$

which, in the limit of CP and CPT (2.5), yields:

$$\lambda_{\pm} = \frac{1}{2}\left(H_{11} + H_{22} \pm \sqrt{4H_{12}H_{21}}\right) \overset{CPT}{=} H_{11} \pm \sqrt{H_{12}H_{21}}. \tag{2.9}$$

Having eigenvalues, the eigenstates $v_{\pm}$ can be computed from:

$$\begin{pmatrix} H_{11} - \lambda_{\pm} & H_{12} \\ H_{21} & H_{22} - \lambda_{\pm} \end{pmatrix} v_{\pm} = 0. \tag{2.10}$$

Finally the eigenvectors can be expressed as:

$$v_+ \equiv |K_S\rangle = \frac{1}{\sqrt{2(1+|\epsilon_S|^2)}}\left[(1+\epsilon_S)\left|K^0\right\rangle + (1-\epsilon_S)\left|\bar{K}^0\right\rangle\right], \tag{2.11}$$

$$v_- \equiv |K_L\rangle = \frac{1}{\sqrt{2(1+|\epsilon_L|^2)}}\left[(1+\epsilon_L)\left|K^0\right\rangle - (1-\epsilon_L)\left|\bar{K}^0\right\rangle\right], \tag{2.12}$$

where ϵ_S and ϵ_L are two small (of the order 10^{-3}) complex parameters describing the CP violation for K_S and K_L respectively.

In contrast to K^0 and $\bar{K}^0$ which differ in *production*, K_S and K_L states differ in *decay* modes. K_S being predominantly state with $CP = +1$ decays mostly into 2π system and K_L being state with $CP = -1$ decays into 3π state. It is often written that K_S is a *short-lived* kaon and K_L a *long-lived* kaon. It is also useful to define the eigenvalues:

$$\lambda_+ \equiv \lambda_S = m_S - i\frac{\Gamma_S}{2} \qquad \text{and} \qquad \lambda_- \equiv \lambda_L = m_L - i\frac{\Gamma_L}{2}, \tag{2.13}$$

and the differences:

$$\Delta m = m_L - m_S > 0 \qquad \text{and} \qquad \Delta\Gamma = \Gamma_S - \Gamma_L > 0. \tag{2.14}$$

The K_S and K_L properties are summarized in Tab. 2.1.

	K_S	K_L
mean life time	(89.53 ± 0.05)ps	(51.16 ± 0.20)ns
mass and Δm	$m_{K^0} = (497.614 \pm 0.024)$MeV, $\Delta m = (3.483 \pm 0.006) \cdot 10^{-12}$MeV	
main decay modes	$\pi^+\pi^-$ $(69.20 \pm 0.05)\%$ $\pi^0\pi^0$ $(30.69 \pm 0.05)\%$ $\pi^+\pi^-\gamma$ $(1.79 \pm 0.05) \cdot 10^{-3}$ $\pi^{\pm}e^{\mp}\nu_e$ $(7.04 \pm 0.08) \cdot 10^{-4}$ $\pi^{\pm}\mu^{\mp}\nu_{\mu}$ $(4.69 \pm 0.05) \cdot 10^{-4}$	$\pi^{\pm}e^{\mp}\nu_e$ $(40.55 \pm 0.12)\%$ $\pi^{\pm}\mu^{\mp}\nu_{\mu}$ $(27.04 \pm 0.07)\%$ $3\pi^0$ $(19.52 \pm 0.12)\%$ $\pi^+\pi^-\pi^0$ $(12.54 \pm 0.05)\%$ $\pi^{\pm}e^{\mp}\nu_e\gamma$ $(3.79 \pm 0.06) \cdot 10^{-3}$ $\pi^+\pi^-$ $(1.966 \pm 0.012) \cdot 10^{-3}$

Table 2.1: Selected information about K_S and K_L mesons [18]

2.4 Final state amplitudes and double decay rate distributions

At KLOE, neutral kaons are produced in a decay of the ϕ meson, which is a vector meson with $J^{PC} = 1^{--}$. Hence, to conserve the eigenvalues of P and C, kaon system needs to have also these values equal to -1. To satisfy this, the simplest initial state of the two kaons has to be antisymmetric and can be expressed as [10]:

$$|i\rangle = \frac{1}{\sqrt{2}} \left[\left|K^0(+\vec{p})\right\rangle \left|\bar{K}^0(-\vec{p})\right\rangle - \left|\bar{K}^0(+\vec{p})\right\rangle \left|K^0(-\vec{p})\right\rangle \right] \tag{2.15}$$

and as required: $C\,|i\rangle = -\,|i\rangle$ and $P\,|i\rangle = -\,|i\rangle$.

The strangeness basis $\{\left|K^0\right\rangle,\ \left|\bar{K}^0\right\rangle\}$, suitable to describe kaons production, can be changed to $\{|K_S\rangle, |K_L\rangle\}$ basis, appropriate to describe decays of kaons:

$$|i\rangle = \frac{N}{\sqrt{2}} \left[|K_S(+\vec{p})\rangle\, |K_L(-\vec{p})\rangle - |K_L(+\vec{p})\rangle\, |K_S(-\vec{p})\rangle \right], \tag{2.16}$$

where a normalization factor N is equal to:

$$N = \frac{\sqrt{(1+|\epsilon_S|^2)\,(1+|\epsilon_L|^2)}}{1-\epsilon_S\epsilon_L} \approx 1. \tag{2.17}$$

The short- and long-lived states evolve in time as pure exponentials:

$$\begin{aligned} |K_S(t)\rangle &= e^{-i\lambda_S t}\,|K_S\rangle\,, \\ |K_L(t)\rangle &= e^{-i\lambda_L t}\,|K_L\rangle\,. \end{aligned} \tag{2.18}$$

Therefore, according to quantum mechanics, the decay amplitude of the two kaons state (2.16) into final states f_1 and f_2 at kaon proper times t_1 and t_2 and with momenta $+\vec{p}$ and $-\vec{p}$ respectively, can be written as [10]:

$$\begin{aligned} A\,(f_1,t_1;f_2,t_2) &= \frac{N}{\sqrt{2}} \left[\langle f_1|T|K_S(t_1)\rangle \langle f_2|T|K_L(t_2)\rangle - \langle f_1|T|K_L(t_1)\rangle \langle f_2|T|K_S(t_2)\rangle \right] = \\ = \quad \frac{N}{\sqrt{2}} &\left[\langle f_1|T|K_S\rangle \langle f_2|T|K_L\rangle\, e^{-i\lambda_S t_1} e^{-i\lambda_L t_2} - \langle f_1|T|K_L\rangle \langle f_2|T|K_S\rangle\, e^{-i\lambda_L t_1} e^{-i\lambda_S t_2} \right] \end{aligned} \tag{2.19}$$

where T is the transition matrix whose explicit form is not needed here.

The double decay rate for $\phi \to K^0\bar{K}^0 \to f_1 f_2$ can be computed from equation (2.19), taking its complex conjunction and using the definitions of (2.13) and (2.14) [10]:

$$\begin{aligned} I(f_1,t_1;f_2,t_2) &= |A(f_1,t_1;f_2,t_2)|^2 = A(f_1,t_1;f_2,t_2)A^*(f_1,t_1;f_2,t_2) = \\ &= C_{12}\Big[|\eta_1|^2 e^{-\Gamma_L t_1 - \Gamma_S t_2} + |\eta_2|^2 e^{-\Gamma_S t_1 - \Gamma_L t_2} + \\ &- 2|\eta_1||\eta_2| e^{-\frac{(\Gamma_S+\Gamma_L)}{2}(t_1+t_2)} \cos(\Delta m(t_1-t_2) + \varphi_2 - \varphi_1) \Big], \end{aligned} \tag{2.20}$$

where φ_1 and φ_2 are phases and:

$$\begin{aligned} C_{12} &= \frac{|N|^2}{2} \left| \langle f_1|T|K_S\rangle \langle f_2|T|K_S\rangle \right|^2, \\ \eta_i &= |\eta_i| e^{i\varphi_i} \equiv \frac{\langle f_i|T|K_L\rangle}{\langle f_i|T|K_S\rangle}. \end{aligned} \tag{2.21}$$

If one wants to compare experimental data to this theoretical evaluations, it is easier to use one-dimensional time distributions with $\Delta t = t_1 - t_2$ instead of t_1 and t_2 as arguments. To obtain Δt distribution one has to integrate the formula (2.20) over $t = t_1 + t_2$ at a fixed difference of time Δt. Finally the formula yields [10]:

$$\begin{aligned} I(f_1, f_2; \Delta t \geq 0) &= \frac{C_{12}}{\Gamma_S + \Gamma_L}\Big[|\eta_1|^2 e^{-\Gamma_L \Delta t} + |\eta_2|^2 e^{-\Gamma_S \Delta t} + \\ &- 2|\eta_1||\eta_2| e^{-\frac{(\Gamma_S+\Gamma_L)}{2}\Delta t} \cos(\Delta m \Delta t + \varphi_2 - \varphi_1)\Big], \end{aligned} \tag{2.22}$$

valid for $\Delta t \geq 0$, while for $\Delta t < 0$ the substitutions $\Delta t \to |\Delta t|$ and $1 \leftrightarrow 2$ have to be applied. Both equations (2.20) and (2.22) show a time interference term which is a characteristic correlation between both kaon decays.

2.5 Quantum entanglement

Predictions about strongly correlated quantum mechanical systems were first revealed by Albert Einstein in 1935, in a joint paper with Boris Podolsky and Nathan Rosen [17]. They formulated a thought experiment whose outcome is counterintuitive and suggests that quantum mechanics is incomplete and nonlocal (*EPR paradox* − Einstein-Podolsky-Rosen paradox). In the experiment they considered two systems A and B which interact with each other and after some time they are separated. Then a measurement of a quantity Q in a system A is done and, since the relationship between the measured value in the system A and this quantity in the system B is known, the observer knows immediately, without any measurement on the system B, the value of Q for the second system. The same can be done for a quantity P in the system B since it was not disturbed. In general, in quantum mechanics, in the case of two physical quantities described by noncommuting operators, the knowledge of one precludes the knowledge of the other. Hence, the outcome of the experiment seems to violate it because after both measurements, the quantities Q and P of both systems are known with certainty. In their work, Einstein, Podolsky and Rosen concluded: *We are thus forced to conclude that the quantum-mechanical description of physical reality given by wave functions is not complete.*

The term *entanglement* was not first used by EPR but by Erwin Schrödinger. In his letter to Einstein he used the word Verschränkung, and then translated by himself as entanglement.

2.5.1 Identical final states in kaon decays

If one now considers that both K_L and K_S decay into any identical final states $f_1 = f_2$, for example $K_L \to \pi^+\pi^-$ and $K_S \to \pi^+\pi^-$, from equation (2.21) can be seen that $\eta_1 = \eta_2 = \eta$ and $\varphi_1 = \varphi_2$. Substituting this to (2.22) one obtains:

$$I(f_1 = f_2; |\Delta t|) = \frac{C_{12}|\eta|^2}{\Gamma_S + \Gamma_L}\Big[e^{-\Gamma_L|\Delta t|} + e^{-\Gamma_S|\Delta t|} - 2e^{-\frac{(\Gamma_S+\Gamma_L)}{2}|\Delta t|}\cos(\Delta m|\Delta t|)\Big]. \tag{2.23}$$

From the above equation results that the two kaons cannot decay into the same final states *at the same time*, so for $|\Delta t| = 0$, since:

$$I(f_1 = f_2; |\Delta t| = 0) = \frac{C_{12}|\eta|^2}{\Gamma_S + \Gamma_L}[1 + 1 - 2] = 0, \tag{2.24}$$

what is visible in Fig. 2.1, where $I(\pi^+\pi^-, \pi^+\pi^-; |\Delta t|)$ distribution is shown. What it really means is that, even though the two kaons are spatially separated, behavior of one of them is dependent on what the other does. This counterintuitive correlation is of the type first pointed out by EPR and is called *quantum entanglement*.

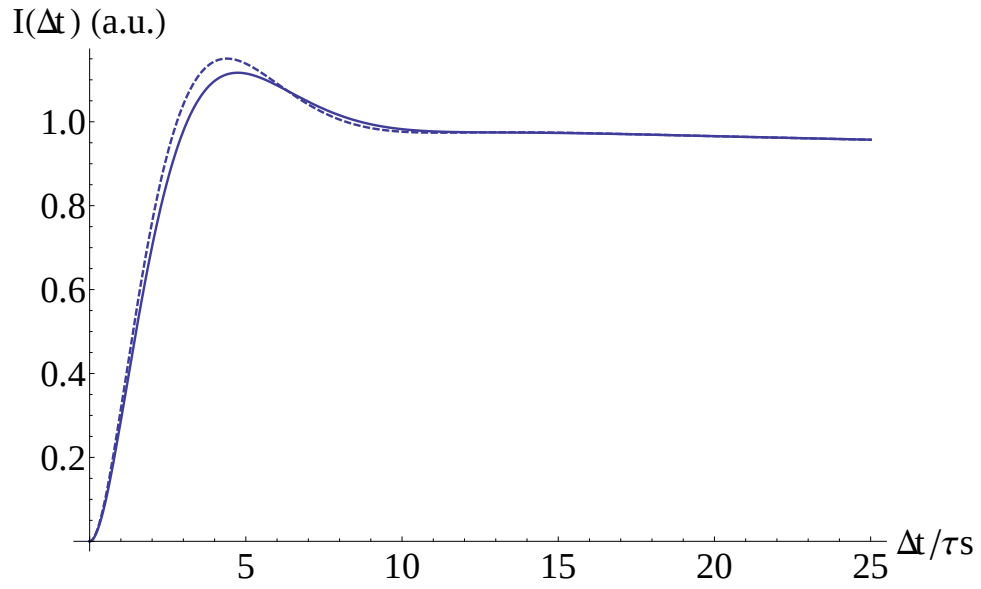

Figure 2.1: The solid line denotes $I(\pi^+\pi^-, \pi^+\pi^-; |\Delta t|)$ distribution as a function of $|\Delta t|$ in units of K_S life times τ_S. The dashed line is for Δm greater by 10% than it is listed in Tab. 2.1

Another interesting region in distribution in Fig. 2.1 is around $4\tau_S$. One can see that it is sensitive for Δm variations.

2.5.2 Decoherence parameter

In general decoherence denotes the transition of a pure state into an incoherent mixture of states [10], meaning that entanglement of particles is lost. The decoherence parameter ζ can be introduced by multiplying the interference term in equation (2.20) by a factor $(1 - \zeta)$:

$$\begin{aligned} I(f_1, t_1; f_2, t_2) &= C_{12}\Big[|\eta_1|^2 e^{-\Gamma_L t_1 - \Gamma_S t_2} + |\eta_2|^2 e^{-\Gamma_S t_1 - \Gamma_L t_2} + \\ &- 2(1-\zeta)|\eta_1||\eta_2| e^{-\frac{(\Gamma_S + \Gamma_L)}{2}(t_1 + t_2)} \cos(\Delta m(t_1 - t_2) + \varphi_2 - \varphi_1)\Big]. \end{aligned} \tag{2.25}$$

A value of $\zeta = 0$ corresponds to the usual quantum mechanics case, while the $\zeta = 1$ corresponds to the total decoherence, so kaons are no longer entangled. Different values correspond to intermediate situations between these two. Moreover, in general ζ depends

on the basis in which the initial state is expressed: $\{\left|K^0\right\rangle, \left|\bar{K}^0\right\rangle\}$ or $\{|K_S\rangle, |K_L\rangle\}$. Current measurements show that there are no deviations from quantum mechanics [16]:

$$\begin{aligned} \zeta_{SL} &= (0.3 \pm 1.8_{stat} \pm 0.6_{syst}) \cdot 10^{-2}, \\ \zeta_{0\bar{0}} &= (1.4 \pm 9.5_{stat} \pm 3.8_{syst}) \cdot 10^{-7}. \end{aligned} \tag{2.26}$$

Figure 2.2 shows sensitivity of the double decay rate distribution to the value of ζ. The biggest discrepancy is for Δt close to 0.

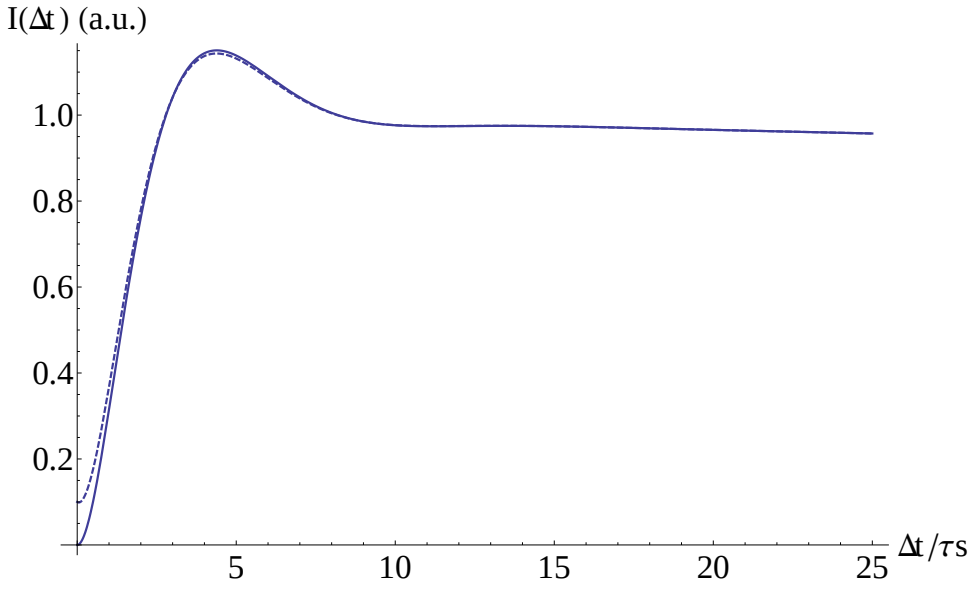

Figure 2.2: The solid line is the double decay rate as a function of $|\Delta t|$ for $\zeta = 0$ whereas the dashed one is for $\zeta = 0.05$.

3. The KLOE experiment at the DAΦNE collider

KLOE (**K LO**ng **E**xperiment) was located at the National Institute of Nuclear Physics (INFN) in Frascati near Rome. It was installed at the interaction point of the electron and positron beams of the DAΦNE (**D**ouble **A**nnular Φ-factory for **N**ice **E**xperiments) collider.

KLOE started data taking in 1999 and concluded in 2006 with integrated luminosity of ~ 2.5 fb^{-1}, when the collider operated around the mass of the ϕ-meson equal to (1019.456±0.029) MeV. During years 1999-2000 the DAΦNE performances were optimized, luminosity was instantaneously increasing [20] and also background contamination was steadily improving. Finally in 2001 DAΦNE reached peak luminosity at $\sim 5 \cdot 10^{31}$ cm^{-2}s^{-1} and in 2002 at $\sim 8 \cdot 10^{31}$ cm^{-2}s^{-1}, resulting in ~ 450 pb^{-1} of data in 2001-2002 run. The year 2003 was spent on detector and accelerator maintaining in order to increase DAΦNE luminosity. During 2004-2005 run a luminosity peak of $\sim 1.5 \cdot 10^{32}$ cm^{-2}s^{-1} has been reached, corresponding to ~ 2 fb^{-1} of data (Fig. 3.1). Year 2006 was spent on collecting 250 pb^{-1} of off-peak data [12].

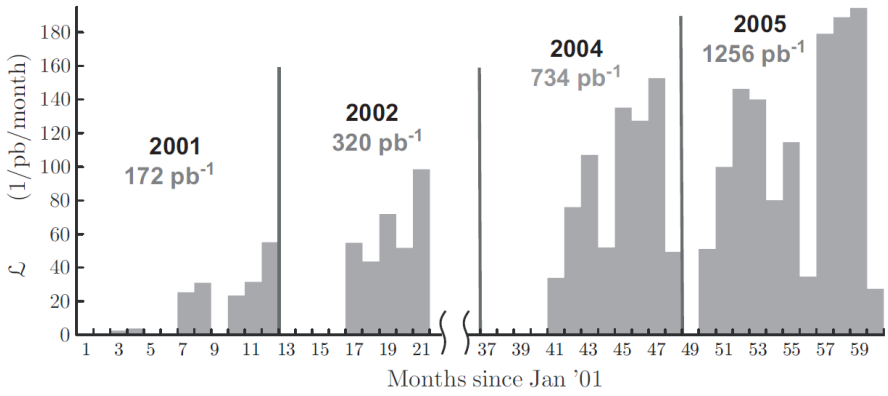

Figure 3.1: KLOE integrated luminosity as a function of time. The figure is adapted from [28].

The main goal of the KLOE experiment is the precise measurement of the $CP-$symmetry violation parameters in the decays of neutral kaons, especially the $K_L \to \pi^+\pi^-$ and $K_L \to \pi^0\pi^0$ decays [20]. Because of the large cross-section for the ϕ meson production equal to $\sigma(e^+e^- \to \phi) = 3.1\ \mu b$, during its six years of operating, DAΦNE was able to produce around 10^{10} of this particles and that is why it is called a ϕ-factory. The main ϕ decay channels are listed in Tab. 3.1.

Now a new experiment, KLOE-2 [14], is about to start collecting data at the same place. Compared to KLOE it is upgraded with new detectors mainly close to the interaction point [31] while the electromagnetic calorimeter and the drift chamber remain the same.

Decay	BR (%)
$\phi \to K^+K^-$	49.1
$\phi \to K_SK_L$	33.8
$\phi \to \rho\pi + \pi^+\pi^-\pi^0$	15.6
$\phi \to \eta\gamma$	1.26

Table 3.1: Main decay channels of the ϕ meson [18]

3.1 DAΦNE accelerator

The DAΦNE collider is a double-ring e^+e^- accelerator designed to obtain a peak luminosity of $\sim 5 \cdot 10^{32}$ cm^{-2}s^{-1}. It consists of three main components: a LINAC, an accumulation ring, and two collision rings (Fig. 3.2).

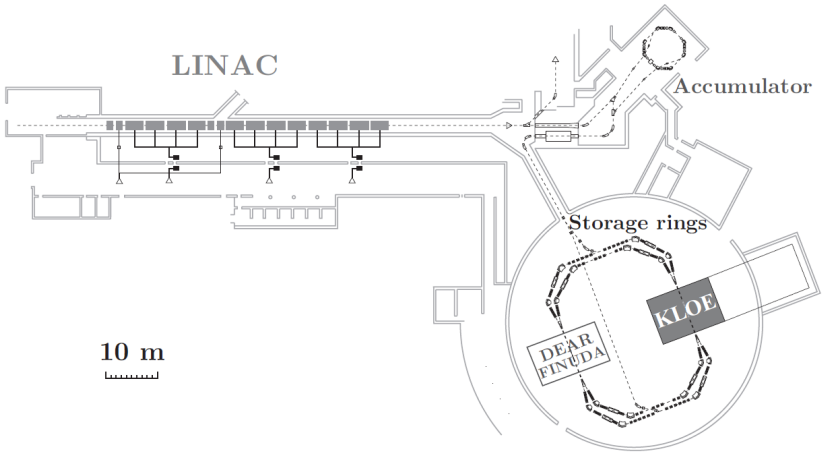

Figure 3.2: The DAΦNE facility scheme. The figure is adapted from [28].

Positrons and electrons, with intensities varying from one to 10^{11} particles in each bunch, are accelerated to energies from 25 to 750 MeV in a 60 m long LINAC (**Lin**ear **Ac**celerator) [22]. LINAC can work in two modes: the electron production and the positron production. Positrons require first accelerating electrons to about 250 MeV to an intermediate station (positron converter target) in the LINAC, where positrons are created [27]. In this place the conversion is obtained by interposing to the electron beam a metallic target and collecting the produced positrons by a capture system. The system allows the choice of 3 different targets, built with an alloy of 75% of tungsten and 25% of rhenium [26]. In the electron mode the positron converter metallic target is extracted and the separator is turned off so that the electron beam can go directly to the LINAC end [25].

Accelerated positrons and electrons are accumulated and cooled in accumulator and transferred to the two crossing storage rings, in which around 120 bunches of both electrons and positrons are stored. Each bunch collides with its counterpart once per turn [27] in the **I**nteraction **P**oint (IP) with a crossing angle $\theta_x \simeq 25$ mrad. Therefore, the ϕ meson is produced with a momentum of about 13 MeV in the horizontal plane [20]. Main properties of the accelerator are listed in Tab. 3.2.

Parameter	Value
Energy of e^+ and e^-	510 MeV
Trajectory length	97.69 m
RF frequency	368.26 MHz
Bunch length	$\sigma_x = 0.2$cm, $\sigma_y = 20\mu$m, $\sigma_z = 3$cm
Number of colliding bunches	up to 120
Beam crossing angle	25 mrad
Luminosity	$\sim 5 \cdot 10^{32}$cm^{-2}s^{-1}

Table 3.2: The DAΦNE design parameters [22].

The KLOE experiment was situated at the one of the two collision points at DAΦNE. In the second one two other experiments: DEAR and FINUDA were working.

3.2 Main detectors

The design of KLOE was driven by the intent of being a definitive high precision experiment for the K_L decays into charged and neutral particles, while the size was dictated by the mean decay length of the K_L meson [23].

Transverse view of the detector is shown in Fig. 3.3.

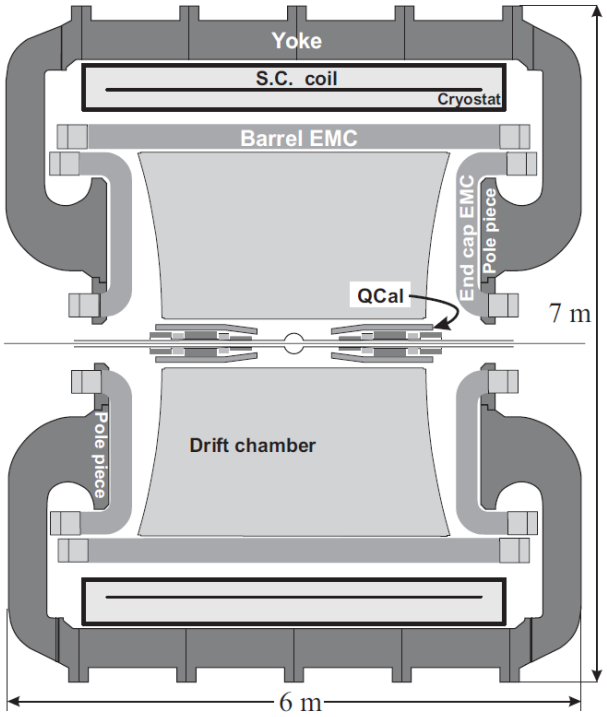

Figure 3.3: Scheme of the KLOE detector. The figure is adapted from [28].

The K_L and K_S mesons, which are created in the ϕ decays at DAΦNE, are moving with velocity equal to about (1/5)c. The mean life time of K_S is equal to ∼80 ps and for K_L ∼51 ns, so the K_S mean decay length is about 0.6 cm while K_L ∼3.5 m (it means that

after this distance, 63% of kaons will decay). KLOE active part has 2 m radius, so it is able to catch about 40% of long-lived neutral kaon decays. Moreover, KLOE detector must be able to track particles with momenta covering the range from 50 to 500 MeV, to detect photons with energy from 20 to 500 MeV with high efficiency and to measure the cluster energy, time and position in order to determine the decay point of the neutral kaons.

The detector was composed of a cylindrical drift chamber (DC) (to register charged particles' tracks), surrounded by an a electromagnetic calorimeter (EmC) (to register particles' energies, times and positions), both inserted in a superconducting coil which produces an axial magnetic field of 0.52 T, parallel to the beam axis (to obtain particles' momenta) [20].

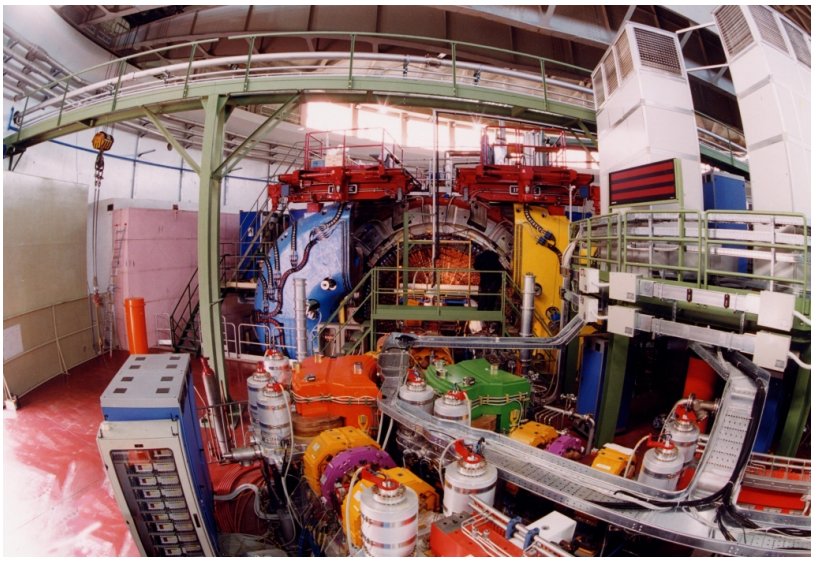

Figure 3.4: KLOE at DAΦNE ring in the accelerator's building. The figure is adapted from [19].

3.2.1 Drift Chamber

As mentioned in section (3.2), design of the KLOE **D**rift **C**hamber (DC) [29] was motivated by the request of high precision detection of charged secondary products from a decay. The drift chamber should be also as transparent as it is possible for the detection of neutral particles in calorimeter [23]. Moreover, high and uniform efficiency in the reconstruction of secondary vertices is required in large volume [19]. Space resolution is limited by the multiple Coulomb scattering which increases with the atomic number of the material.

The KLOE drift chamber works as every gas detector, based on multiplication mechanism. When charged particle travels through gas it undergoes repeated collisions with electrons inside the gas atoms and ionizes the medium. Electrons of the ion pairs created along the particle's trajectory drift to the positive voltage wires [27]. Close to the wire, due to high intensity electric field they collide with other gas molecules which leads to further emission of electrons, resulting in electron multiplication and signal detection at the wire's end. Particle's trajectory is bent in a magnetic field and from this curvature it is also possible to determine particle's momentum.

To meet the desirable performances, the KLOE drift chamber was constructed from over 50 thousand of wires, arranged in 58 cylindrical layers around the beam pipe, giving a total of more than 12.5 thousand of square drift cells (2x2, 3x3 cm^2) (Fig. 3.5 right). Wires belonging to the same layer are parallel to each other, while each layer is slightly tilted (stereo angle) with respect to the neighbouring ones [24] in order to reconstruct the z coordinate along the cylinder axis. The diameter and length of DC are 4 m and 3.3 m, respectively. The chamber is filled with 90% of helium and 10% of isobutan. Momentum reconstruction from the curvature of its track has a fractional accuracy of $\frac{\sigma_p}{p} \simeq 0.5\%$ [27]. The spatial resolution is below 200 μm in the transverse plane ("φ-coordinates") and the accuracy of vertex reconstruction is about $\simeq$ 1 mm. On the left side of Fig. 3.5 the drift chamber barrel before installing it in the detector is shown.

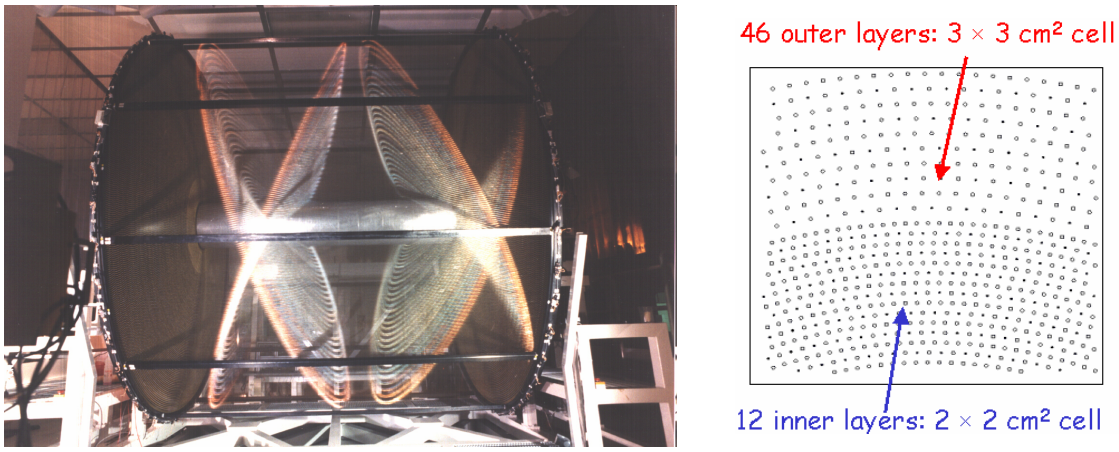

Figure 3.5: Left: KLOE Drift Chamber, right: cells geometry. The figures are adapted from [19].

3.2.2 Electromagnetic Calorimeter

The KLOE calorimeter [30] (Fig. 3.6 left) was designed with many requirements in order to be an extremely high precision tool to measure neutral kaons decays. It should detect low energy photons with high efficiency, have a good energy resolution and excellent time and space resolution to determine vertices of K_S and K_L neutral decays. Another requirement is ability to distinguish $CP-$violating events $K_L \to \pi^0\pi^0$ from $K_L \to \pi^0\pi^0\pi^0$ (together with information from the drift chamber) [19]. Therefore, splitting and merging of signals should be minimized and the calorimeter should cover as much of the 4π angle as it is possible. Hence, it is not only a calorimeter but also a time-of-flight detector.

In an electromagnetic calorimeter the incoming particle (a photon, electron or positron) interacting with matter through pair production or bremsstrahlung process (dominant at high energies) gives rise to repeated interactions in cascade, so called electromagnetic shower, until all its energy is spent inside the medium. The energy deposited by the electromagnetic shower in the active volume of the calorimeter is detected, being proportional to the energy of the incoming particle.

The chosen solution for EmC is a sampling calorimeter, composed of about 200 lead passive layers (Fig. 3.6 right), each of 1.2 mm thickness, comprising scintillating fiber

layers of 1 mm diameter. Light is propagating along the fibers of each module and reaches its ends where photomultipliers are situated.

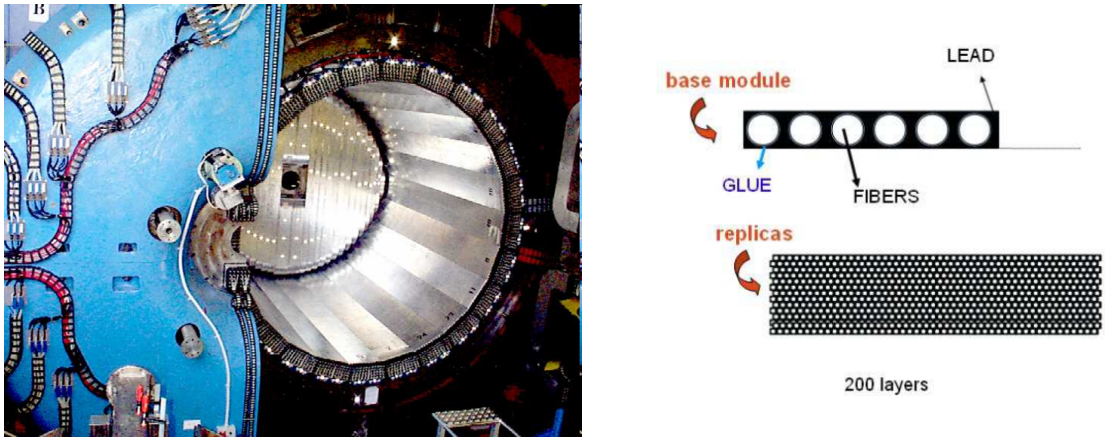

Figure 3.6: Left: KLOE electromagnetic calorimeter (figure adapted from [19]). Right: single layer construction (figure adapted from [22]).

The whole calorimeter consists of a "barrel" and two "end caps". The barrel is divided into 24 trapozoid-shape modules (Fig. 3.7), 23 cm thick, placed along beam direction and it surrounds the drift chamber. The end caps close hermetically the calorimeter, allowing to cover 98% of 4π angle. Each endcap is made of 32 vertical modules with length varying from 0.7 to 3.9 m, bent on both sides in a C-shape [30].

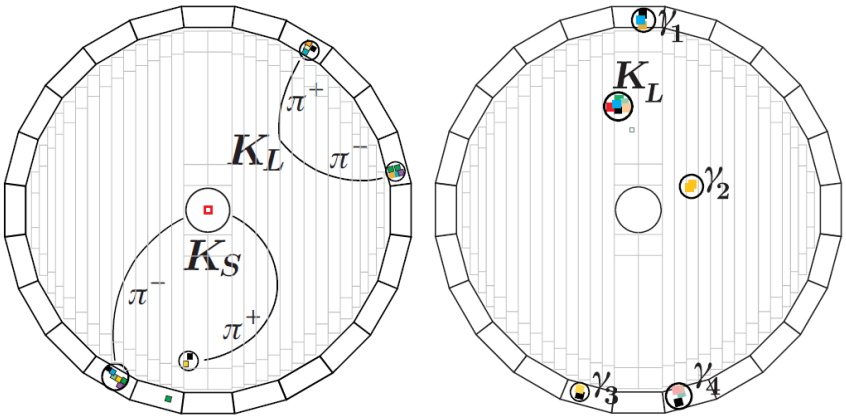

Figure 3.7: Left: $CP-$violating event $K_LK_S \to \pi^+\pi^-\pi^+\pi^-$ registered at the KLOE calorimeter. Right: direct detection of K_L (K_L *crash*) in the calorimeter endcap from the decay $K_LK_S \to K_L\pi^0\pi^0 \to K_L4\gamma$. Figure is adapted from [27].

Spatial, energetic and time resolutions of this calorimeter, for a photon's energy in a range from 20 to 500 MeV, are equal to [22]:

$$\sigma(x) = 1 \text{ cm}, \ \sigma(E) = \frac{5.7\%}{\sqrt{E(\text{GeV})}}, \ \sigma(t) = \frac{54 \text{ ps}}{\sqrt{E(\text{GeV})}}$$

3.3 Interaction region

The beam pipe at the interaction point was designed with requirement that all the K_S mesons decay in the vacuum and $K_L \rightarrow K_S$ regeneration is minimized in the crucial interference region, so for the $\Delta t \approx 0$ (Sec. 2.5.1). Moreover, the beam pipe material should be chosen in the way that nuclear interactions and photon absorption is minimized [23]. The beam pipe at the KLOE interaction point is shown in Fig. 3.8. The geometry of elements situated in this region, called also regenerators, is shown in Fig. 3.9.

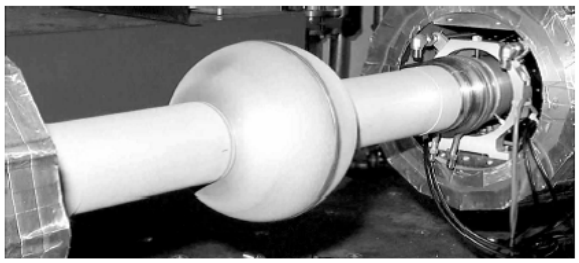

Figure 3.8: Beam pipe at the e^+e^- interaction point. The figure is adapted from [27].

The beam pipe has a spherical shape with 10 cm radius and a center at the e^+e^- interaction point. It is made of an alloy of 62% beryllium and 38% of aluminium and its thickness is ~500 μm. The mean decay length of K_S is about 0.6 cm so the distance of 10 cm corresponds to ~17 life times of short-lived kaon. This assures that all K_S decays are contained inside the sphere. The beam pipe has also a 50 μm thin layer of cylindrical-shape beryllium with radius of 4.4 cm. It guarantees electrical continuity to the pipe inside the sphere [20]. In the new KLOE-2 detector it is changed to 30 μm and 3.7 cm radius. In addition to the spherical and cylindrical beam pipe, the regeneration may also occur on the inner wall of the drift chamber. It is a cylindrical-shape 750 μm thick carbon fiber and 150 μm thick aluminium and has 25 cm radius.

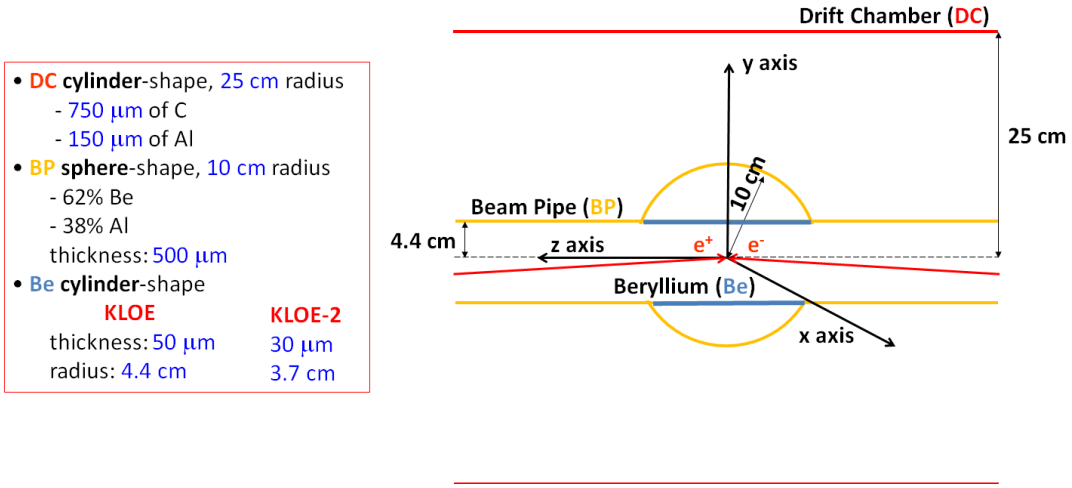

Figure 3.9: Scheme of the regenerators' location at KLOE.

3.4 MonteCarlo simulations

The KLOE MonteCarlo simulation program, GEANFI, is based on GEANT3 libraries [42], often used for high energy physics or astrophysics experiments. It reproduces all known processes rescaled according to a defined luminosity. All relevant machine parameters like $\sqrt{s}$ and $\vec{p}_\phi$ are entered in the MonteCarlo simulation run-by-run [23]. GEANFI includes also an accurate description of the KLOE detector geometry and material composition, which includes:

- the interaction region,
- the drift chamber,
- the calorimeter (barrel and endcaps),
- the magnetic field.

Moreover, a set of dedicated routines were elaborated to simulate each sub-detector response. Hadronic interactions are simulated using the GHEISHA hadronic showers generator. It has been necessary to carry out a dedicated simulation, since the hadronic showers package in the GEANT3 and FLUKA libraries does not simulate the hadronic interactions in the energy range interested for the KLOE experiment. The hadronic cross sections for low energy kaons, especially for regeneration processes, have been improved with respect to the original GHEISHA library [23].

4. Phenomenology of $K_L \to K_S$ regeneration

The term *regeneration* has been introduced in 1955 by Pais and Piccioni in their work [33] where they predicted creation of short-lived K_S mesons when long-lived K_L mesons traverse matter. This phenomena was experimentally discovered in 1961 by Good and co-workers [34].

Regeneration originates from the fact that the K^0 meson interacts differently with matter (so generally with protons and neutrons) than $\bar{K}^0$. These are strong interactions that must conserve strangeness and charge as well as barion and lepton numbers. Hence, several reactions which $\bar{K}^0$ can undergo, e.g.:

$$\bar{K}^0 + p \to \Lambda^0 + \pi^+ \quad (\bar{d}s + uud \to uds + \bar{d}u)$$
$$\bar{K}^0 + n \to \Lambda^0 + \pi^0 \quad (\bar{d}s + udd \to uds + \bar{d}d)$$

are not possible for K^0. Therefore, the total cross-section for interaction of $\bar{K}^0$ with nucleon N is bigger than the corresponding total cross-section of K^0:

$$\sigma_T(\bar{K}^0 N) \geq \sigma_T(K^0 N), \tag{4.1}$$

where the equality is valid in the asymptotic region [36].

From the optical theorem (see Appendix A) we have that the total effective scattering cross-section of the scatterer is equal to (A.3):

$$\sigma_T = \Im m f(0) \frac{4\pi}{k}, \tag{4.2}$$

where $f(0)$ is the forward scattering amplitude (so for angle equal to zero) and k denotes the wave number of kaon. From expression (4.1) and (4.2) one obtains:

$$|\Im m \bar{f}(0)| > |\Im m f(0)|.$$

Assuming that the real part of $f(0)$ is not correspondingly bigger than $\Re e \bar{f}(0)$, it follows that:

$$|\bar{f}(0)| > |f(0)|.$$

4.1 Interaction of K_L with matter

To understand how the regeneration phenomena occurs we can treat the regenerating material as a scattering medium. Let us consider that long-lived neutral kaon is passing through material. An incident pure K_L state is written in a form (2.12):

$$|i\rangle = |K_L\rangle = \frac{1}{\sqrt{2(1+|\epsilon_L|^2)}} \left[(1+\epsilon_L) \left| K^0 \right\rangle - (1-\epsilon_L) \left| \bar{K}^0 \right\rangle \right].$$

As it was discussed above, the two components $\left|K^0\right\rangle$ and $\left|\bar{K}^0\right\rangle$, are acting differently, and the final state after scattering in the material reads:

$$|f\rangle = \frac{1}{\sqrt{2(1+|\epsilon_L|^2)}}\left[f(\vartheta)\,(1+\epsilon_L)\left|K^0\right\rangle - \bar{f}(\vartheta)\,(1-\epsilon_L)\left|\bar{K}^0\right\rangle\right],$$

where ϑ denotes the scattering angle and $f(\vartheta)$ the scattering amplitude for K^0 and $\bar{f}(\vartheta)$ for $\bar{K}^0$. If we change the basis from $\{\left|K^0\right\rangle, \left|\bar{K}^0\right\rangle\}$ to $\{|K_S\rangle, |K_L\rangle\}$ ((2.11) and (2.12)), we obtain expression:

$$|f\rangle = \frac{1}{2}\left[f(\vartheta) + \bar{f}(\vartheta)\right]|K_L\rangle + \frac{1}{2}\left[f(\vartheta) - \bar{f}(\vartheta)\right]|K_S\rangle, \tag{4.3}$$

which explicitly shows that the emerging state $|f\rangle$ contains a K_S component since $f(\vartheta) \neq \bar{f}(\vartheta)$. This component is *regenerated* from the K_L beam.

For simplicity let us define:

$$f_{reg}(\vartheta) \equiv \frac{f(\vartheta) - \bar{f}(\vartheta)}{2}.$$

Then equation (4.3) reads:

$$|f\rangle = \frac{1}{2}\left[f(\vartheta) + \bar{f}(\vartheta)\right]|K_L\rangle + f_{reg}(\vartheta)\,|K_S\rangle. \tag{4.4}$$

In particular, in the forward direction ($\vartheta = 0$) the amplitude of K_S regenerated by one scattering center is proportional to $f(0) - \bar{f}(0)$. If one now considers two scattering centers, the question arises whether these two scatterers will act coherently or incoherenthy [36].

4.2 Coherent and incoherent regeneration

If the K_L meson hits two scattering centers A and B situated at a distance d from each other, then the resulting K_S wave will depend on the phase of the incoming wave at the scattering center. The phase shift between the outgoing waves from near-by scattering centers can result in a coherent or incoherent action, depending on the density and the size of the medium and on the kaon momentum [36]. Fig. 4.1 depicts schematically the discussed scattering. C denotes the plane perpendicular to the momentum vector of scattered K_S, where the difference of phases is relevant.

In this plane amplitudes due to the scattering at centers A and B read:

$$\begin{aligned} |\psi_A\rangle_S &= e^{ip_S d\cos\vartheta} f_{reg}(\vartheta)\,|K_S\rangle, \\ |\psi_B\rangle_S &= e^{ip_L d} f_{reg}(\vartheta)\,|K_S\rangle, \end{aligned} \tag{4.5}$$

where p_S and p_L are momenta of K_S and K_L, respectively. Hence, the phase difference of both waves in the plane C is equal to:

$$\Delta = d(p_S\cos\vartheta - p_L). \tag{4.6}$$

The intensity of K_S scattered under ϑ angle on centers A and B is calculated as:

$$\begin{aligned} &|\,\langle K_S|\psi_A + \psi_B\rangle_S\,|^2 = |f_{reg}(\vartheta)|^2\left[e^{ip_L d} + e^{ip_S d\cos\vartheta}\right]^2 = \\ = \;& |f_{reg}(\vartheta)|^2 \cdot 2\left[1 + \cos[d(p_S\cos\vartheta - p_L)]\right] = |f_{reg}(\vartheta)|^2 \cdot 2(1+\cos\Delta). \end{aligned} \tag{4.7}$$

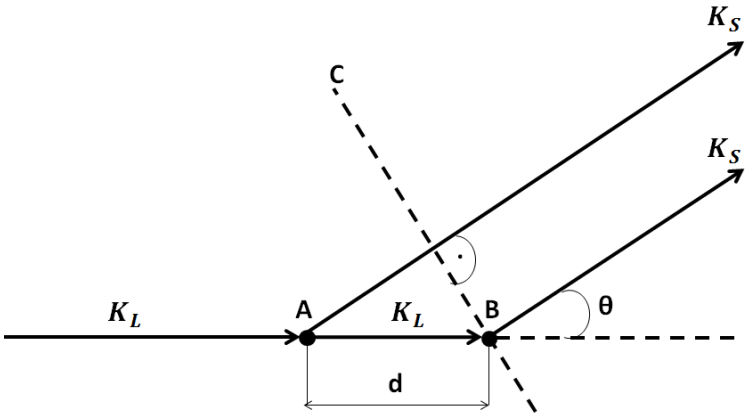

Figure 4.1: Scheme of regeneration in two scattering centers.

If now $\Delta \lesssim 1$ one has:

$$|\langle K_S|\psi_A + \psi_B\rangle_S|^2 \approx 4|f_{reg}(\vartheta)|^2 = |f_{reg}(\vartheta) + f_{reg}(\vartheta)|^2, \tag{4.8}$$

so *coherent* addition of the contributions from the two scattering centers.

On the other hand, if $\Delta \geqslant 1$ and one has many scattering centers, the contribution from $\cos\Delta$ is average to zero:

$$\langle \cos\left[d(p_S\cos\vartheta - p_L)\right]\rangle_N \approx 0;$$

Then for N scattering centers the intensity is N times the intensity from one scattering centre:

$$|\langle K_S|\psi_1 + ... + \psi_N\rangle_S|^2 \approx N|f_{reg}(\vartheta)|^2 = N|\langle K_S|\psi_1\rangle_S|^2 \tag{4.9}$$

and scattering centers act *incoherently.*

Now one can ask what is the limiting angle for coherence? Making approximation that $\cos\vartheta \approx 1 - (\vartheta^2/2)$, the coherence condition reads:

$$d(p_S\cos\vartheta - p_L) = d\left(p_S - p_L - p_S\frac{\vartheta^2}{2}\right) = d\left(\Delta p - p_S\frac{\vartheta^2}{2}\right) \lesssim 1, \tag{4.10}$$

where Δp is the recoil momentum of the nucleon (scattering center) after kaon scattering. The maximal distance d_{max} between two scattering centers when they still act coherently must satisfy:

$$d_{max}\left(\Delta p - p_S\frac{\vartheta^2}{2}\right) \approx 1.$$

In the forward direction ($\vartheta = 0$) from above formula and relation (B.7) (see Appendix B) one obtains:

$$d_{max} \approx \frac{1}{\Delta p} = \frac{1}{\Delta m}\frac{p_L}{m_L}. \tag{4.11}$$

For kaons produced in the ϕ decay: $p_L \approx 110$ MeV/c and taking into account that $\Delta m \approx 3.5 \cdot 10^{-6}$ eV and $m_L \approx 498$ MeV one obtains ($1/\text{eV} \approx 0.197$ μm):

$$d_{max} \approx 0.06 \cdot 10^6 \text{ 1/eV} \approx 1.25 \text{ cm} \approx 2 \lambda_{K_S}, \tag{4.12}$$

where λ_{K_S} denotes the mean K_S decay length. Now one can see that for K_L originating from the ϕ decay at KLOE, regeneration that occurs in the forward direction is always coherent since nuclei in material are always closer to each other than 1.25 cm. However, the probability of coherent regeneration is negligible for KLOE as it will be discussed in the next section.

If we consider scattering angles different from $\vartheta = 0$, from coherence condition comes that this angle is maximal when:

$$d\left(\Delta p - p_S \frac{\vartheta_{max}^2}{2}\right) \approx 0.$$

Hence:

$$\begin{aligned} \Delta p &\approx p_S \frac{\vartheta_{max}^2}{2} \\ \vartheta_{max}^2 &\approx \frac{2\Delta p}{p_S} \sim 10^{-12} \text{ rad} \\ \vartheta_{max} &\approx 10^{-6} \text{ rad}, \end{aligned} \tag{4.13}$$

where $p_S = \Delta p + p_L$.

According to different scattering ways we expect therefore different regeneration processes:

1. **Coherent (transmission) regeneration** : It appears in the strictly forward direction ($\vartheta \lesssim 10^{-6}$ rad) and coherent addition of amplitudes is from a region of $\sim 2\lambda_{K_S}$ so few centimeters length.

2. **Incoherent (elastic, diffraction) regeneration** : It is elastic scattering on nuclei with incoherent addition of amplitudes. The action of the nucleons inside the nucleus is coherent and momentum transfer small, not able to excite the nucleus.

3. **Inelastic regeneration** : This is inelastic scattering with momentum transfer big enough to break up the nucleus or to excite it. This type of process can be neglected at the KLOE detector.

4.3 Regeneration probability

To connect the elementary scattering amplitude $f(\vartheta) - \bar{f}(\vartheta)$ with the macroscopic observed regeneration probability one has to consider coherent and incoherent regeneration separately.

1. For the **coherent** regeneration one can define the emerging state from a pure K_L beam while passing through a regenerator as [36]:

$$|K_L\rangle \to |K_L\rangle + \rho_{coh} |K_S\rangle , \tag{4.14}$$

where, in the approximation of thin regenerator ($d/l_S \ll 1$, d=regenerator thickness, $l_S = K_S$ decay length), ρ_{coh} is:

$$\rho_{coh} = \frac{\pi i}{p_K}(f(0) - \bar{f}(0))nd$$

with density of scattering centers equal to:

$$n = \frac{\rho N_A}{A}$$

and p_K is the kaon momentum, ρ the regenerator density, A the atomic weight and N_A the Avogadro number.

For purposes of this thesis, it is interesting to calculate the intensity of (K_L + ρ_{coh} K_S) $\to \pi^+\pi^-$ decays per time unit. Using eq. (2.20) one can obtain that [37]:

$$\begin{aligned} P_\pm &= \Gamma(K_S \to \pi^+\pi^-) \cdot \Big[|\rho_{coh}|^2 \mathrm{e}^{-\Gamma_S t} + |\eta_\pm|^2 \mathrm{e}^{-\Gamma_L t} + \\ &+ 2|\rho_{coh}||\eta_\pm| \mathrm{e}^{-\frac{\Gamma_S+\Gamma_L}{2}t} \cos\left[\Delta m \cdot t + \varphi(\rho_{coh}) - \varphi(\eta_\pm)\right]\Big] \end{aligned} \tag{4.15}$$

where (2.21):

$$\eta_\pm = \frac{\langle \pi^+\pi^-|T|K_L\rangle}{\langle \pi^+\pi^-|T|K_S\rangle}$$

and t is the kaon proper time and $\Gamma(K_S \to \pi^+\pi^-)$ the decay width. One can define the probability of $\pi^+\pi^-$ decays in excess of pure $K_L \to \pi^+\pi^-$ decays occurring without regenerator as [37]:

$$R_\pm = \int_0^\infty \left[P_\pm(t) - \Gamma(K_S \to \pi^+\pi^-)|\eta_\pm|^2 \mathrm{e}^{-\Gamma_L t}\right] dt \tag{4.16}$$

thus this is the probability of the coherent regeneration for $K_L \to K_S \to \pi^+\pi^-$ decays.

2. For the **incoherent** addition of amplitudes one has that differential cross-section for one nucleus is given by [36]:

$$\frac{\mathrm{d}\sigma_{inc}}{\mathrm{d}\Omega}(\vartheta) = |f_{reg}(\vartheta)|^2 = \frac{|f(\vartheta) - \bar{f}(\vartheta)|^2}{4}. \tag{4.17}$$

Integrating formula (4.17) over solid angle one gets that:

$$\sigma_{inc} = \int |f_{reg}(\vartheta)|^2 \mathrm{d}\Omega. \tag{4.18}$$

For a thin regenerator ($d/l_S \ll 1$), the probability of incoherent regeneration reads [37]:

$$P_{inc} = n\ \sigma_{inc}\ d. \tag{4.19}$$

In the Tab. 4.1 are listed quantitative theoretical evaluations of the incoherent (P_{inc}) and coherent ($R_\pm$) regeneration probabilities as well as modulus of the complex parameter ρ_{coh} for the KLOE regenerators.

regenerator	material	d (μm)	P_{inc}	$\lvert\rho_{coh}\rvert$	$R_{\pm}$
BP	Be	0.05	$2.5 \cdot 10^{-5}$	$\sim 10^{-4}$	$\sim 10^{-7}$
DC	C	0.7	$3.5 \cdot 10^{-4}$	$0.98 \cdot 10^{-3}$	$2.6 \cdot 10^{-6}$
	Al	0.05	$0.56 \cdot 10^{-5}$	$0.34 \cdot 10^{-4}$	$8.7 \cdot 10^{-8}$

Table 4.1: Regeneration probabilities evaluated for momenta $p_K \approx 110$ MeV/c from theoretical calculations obtained in the paper [37], made for the beam pipe (BP) and the drift chamber inner wall (DC) regenerators.

As can be inferred from the above table, the incoherent process dominates at KLOE over coherent one, both for the beam pipe (BP) and the drift chamber inner wall (DC) regenerators.

5. Selection of $K_S K_L \to \pi^+\pi^-\pi^+\pi^-$ events

In order to measure the regeneration cross-sections for the KLOE detector, one has to identify regenerated K_S (K_S^{reg}) decays in the close vicinity of the cylindrical and the spherical beam pipe and the drift chamber inner wall, for events where the K_L mesons pass the regenerators (for the KLOE regenerators' description see Sec. 3.3). Experimentally the best for this analysis at KLOE is $e^+e^- \to \phi \to K_S K_L \to \pi^+\pi^- K_L \to \pi^+\pi^- K_S^{reg} \to \pi^+\pi^-\pi^+\pi^-$ reaction chain, since $K_S \to \pi^+\pi^-$ decay is cleaner and easier to reconstruct than the $K_S \to \pi^0\pi^0$. Therefore, in this chapter the procedures used to identify $K_S \to \pi^+\pi^-$ decays and to select events containing decays of the K_L mesons will be described.

In this thesis data set collected by means of the KLOE detector in 2004-2005 years was used. It corresponds to an integrated luminosity of $\sim$1.7 fb^{-1} (Fig. 3.1). The appropriate MonteCarlo sample was simulated with GEANFI (Sec. 3.4). The number of events simulated for each run is equivalent to expectations based on the experimentally derived run luminosity. Moreover, set of MonteCarlo events consisting of all the ϕ decays are simulated, with K_S and K_L decaying accordingly to experimentally determined branching ratios [18].

5.1 ϕ meson production

At KLOE, the e^+e^- beam crossing angle is equal to 25 mrad (Tab. 3.2) which results in a nonzero boost of the produced ϕ meson. The boost fluctuations can be described by gaussians with average momentum [37]:

$$\langle p_\phi^x \rangle \approx -15 \text{ MeV/c}, \quad \left\langle p_\phi^y \right\rangle \approx 0, \quad \langle p_\phi^z \rangle \approx 0$$

and r.m.s. widths are: $\sigma_{p_\phi^x} \approx 0.014$ MeV/c, $\sigma_{p_\phi^y} \approx 0$, $\sigma_{p_\phi^z} \approx 1.043$ MeV/c, where x, y and z are radial, vertical and longitudinal axes, respectively, defined in Fig. 5.1. This boost causes that K_L and K_S momentum spectra are spread in the laboratory frame.

As a very first data selection, a set of requirements is imposed on kinematics of the e^+e^- system in the initial state. Based on the Bhabha scattering events for each run it is required [23]:

- the average value of y and z components of ϕ total momentum must satisfy: $|p_\phi^y| < 3$ MeV/c, $\quad |p_\phi^z| < 3$ MeV/c;
- the average total energy in the center of mass: $|\sqrt{s} - m_\phi| < 5$ MeV;
- the average position of the beam crossing point: $|x_\phi| < 3$ cm, $|y_\phi| < 3$ cm, $|z_\phi| < 5$ cm;
- the spread in the beam interaction region: $\sigma_x < 3$ cm, $\quad \sigma_z < 3$ cm.

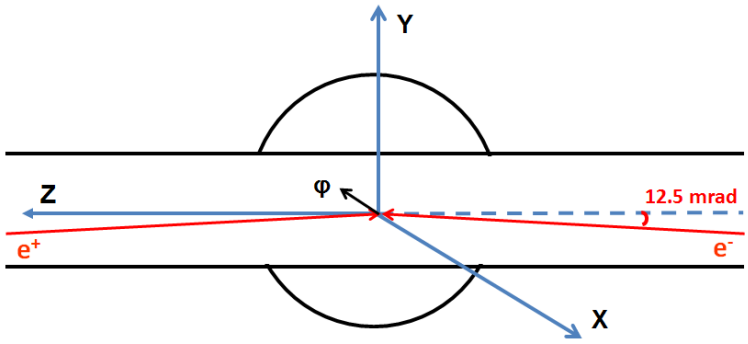

Figure 5.1: The reconstruction coordinate system of particles' decays at KLOE.

The distribution of the ϕ meson momentum coordinates as well as total value are shown in Fig. 5.2.

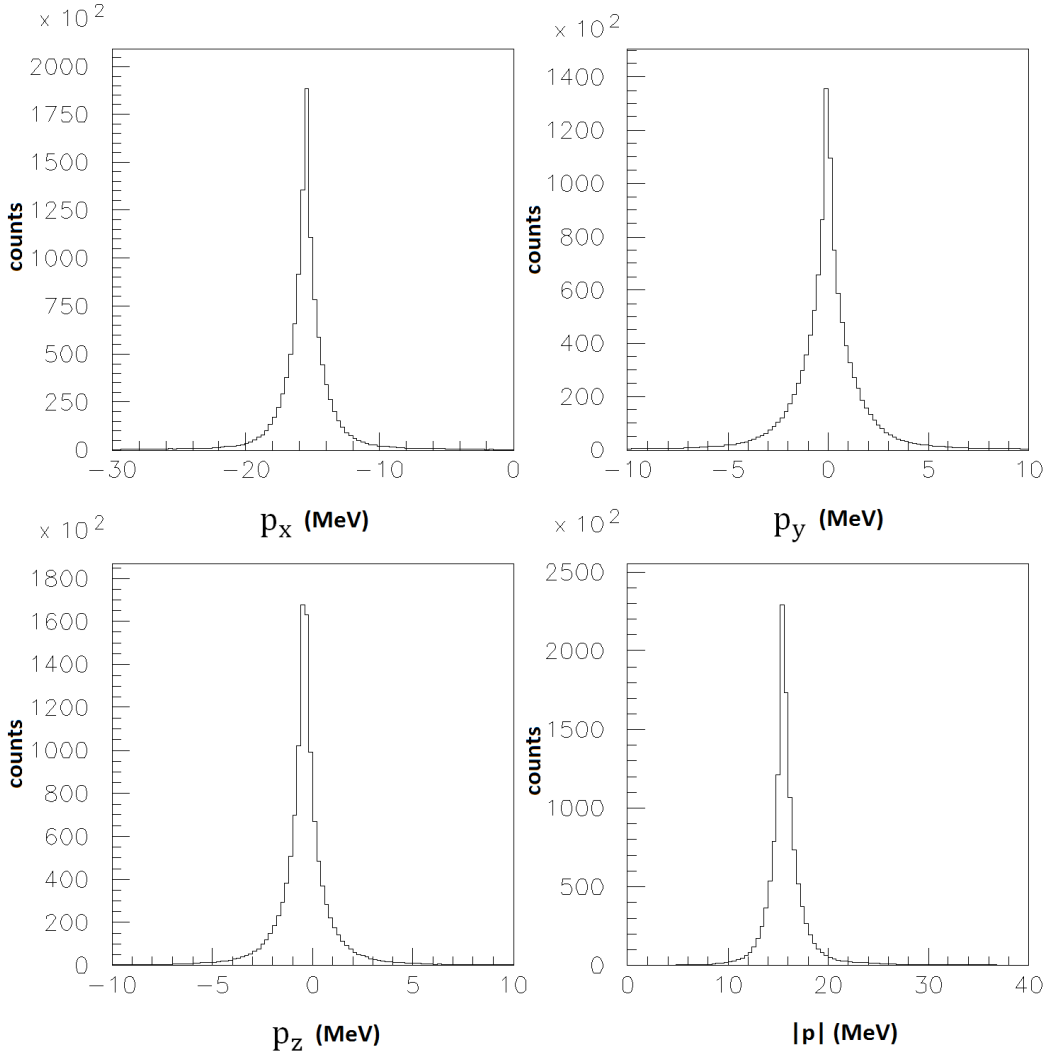

Figure 5.2: Experimental distribution of the ϕ meson momentum in the KLOE reference frame.

In Fig. 5.3 the distribution of ϕ decay point, integrated over all runs, is presented. One can see, that average z position is equal to $\langle z_\phi \rangle \approx 0.7$ cm.

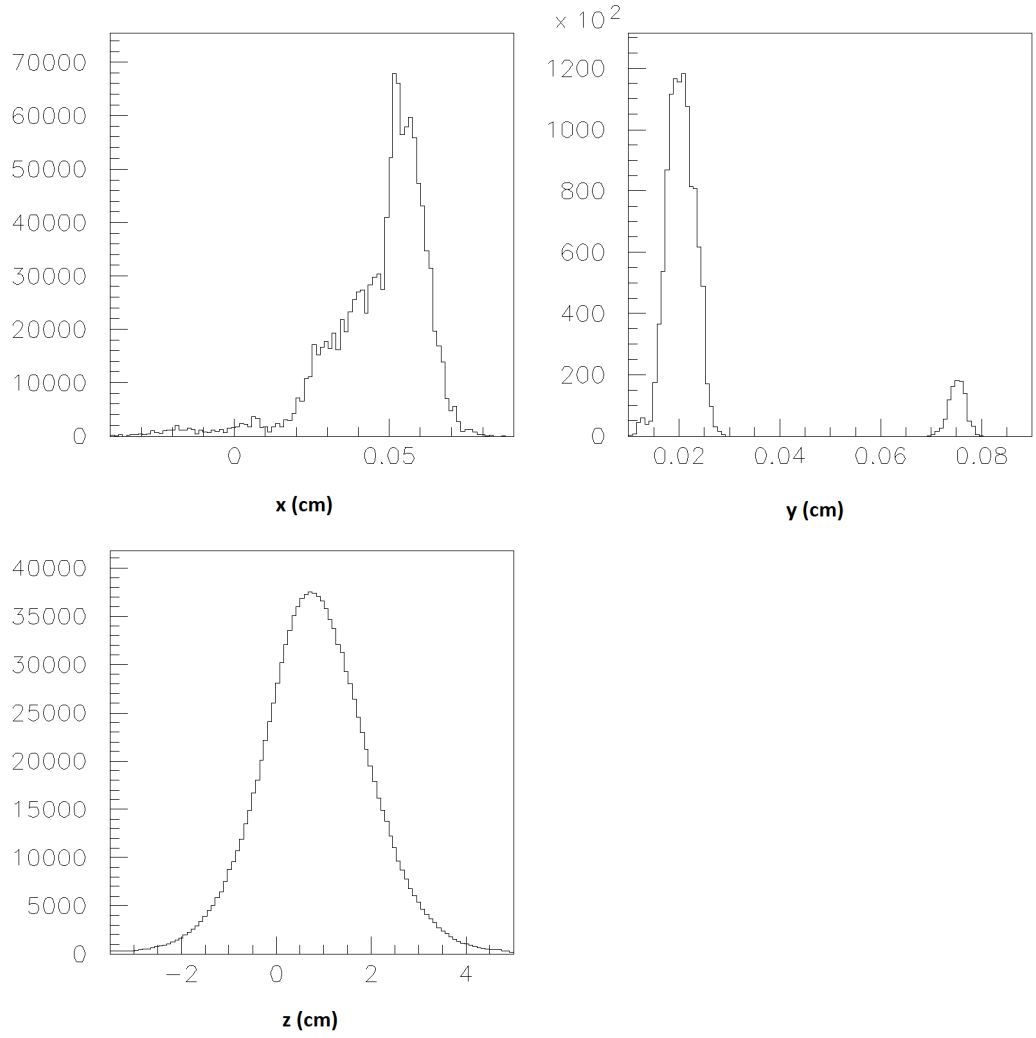

Figure 5.3: Experimental distribution of the position of ϕ decay point in the KLOE reference frame.

5.2 Identification of $K_S \to \pi^+\pi^-$ and $K_L \to \pi^+\pi^-$ decays (K_L *tag*)

The K_L mesons candidates are identified by presence of $K_S \to \pi^+\pi^-$ decays close to the interaction region. This type of selection at KLOE is called the K_L *tag*. After identification of the K_S meson originating from the ϕ meson decay, one searches for K_L that was produced with the opposite momentum vector in the ϕ rest frame (Fig. 5.4). Therefore, the K_L tagged decay is searched along the line of its supposed momentum, defined by the momentum of K_S and ϕ:

$$\vec{p}_{K_L^{tag}} = \vec{p}_\phi - \vec{p}_{K_S}$$

and the nominal position of the production vertex, $\vec{x}_\phi$

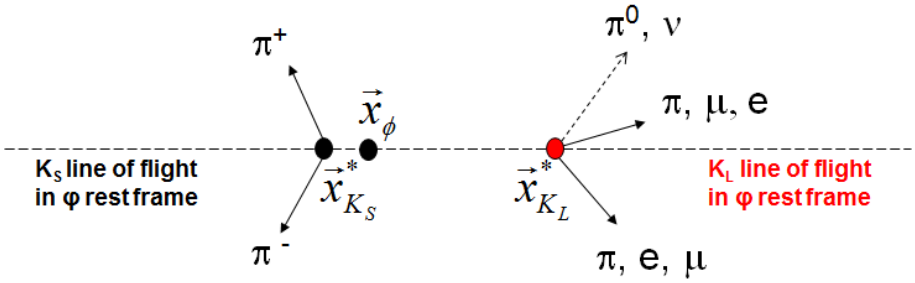

Figure 5.4: Schematically presented reconstruction of K_L *tag* line of flight.

The event selection starts with the identification of a $K_S \to \pi^+\pi^-$ originating from the ϕ decay by requiring:

- two and only two bent tracks connected to a vertex, corresponding to particles with opposite charge;
- the vertex within a cylindrical *fiducial volume*, centered on the nominal ϕ position, obtained run-by-run from Bhabha events:

$$\rho = \sqrt{x_{K_S}^2 + y_{K_S}^2} < 10 \text{ cm} \quad \text{and} \quad |z_{K_S}| < 20 \text{ cm}, \tag{5.1}$$

  where the cylindrical fiducial volume is due to the fact that the σ_z is larger than the ones along x and y;
- the invariant mass of the two charged particles' system (calculated assuming that the observed tracks corresponds to π^+ and π^- mesons) must be within 15 MeV of the neutral kaon mass:

$$|M_{inv} - m_{K^0}| < 15 \text{ MeV} \quad \text{where} \quad M_{inv}^2 = E_{tot}^2 - |\vec{p}_{tot}|^2 \,,$$

$$\vec{p}_{tot} = \vec{p}_{\pi^+} + \vec{p}_{\pi^-} \quad \text{and} \quad E_{tot} = \sqrt{m_\pi^2 + |\vec{p}_{\pi^+}|^2} + \sqrt{m_\pi^2 + |\vec{p}_{\pi^-}|^2} \tag{5.2}$$

- a difference between the total K_S momentum (p_K^*) and the total momentum of the two pions calculated in the ϕ rest frame (p_{tot}^*) must be less than 20 MeV/c. The K_S momentum is given by the two-body kinematics of $\phi \to K_SK_L$:

$$\begin{aligned} |p_{tot}^* - p_K^*| \quad &< \quad 20 \text{ MeV/c} \\ p_{tot}^* = |\vec{p}_{\pi^+}^{\,*} + \vec{p}_{\pi^-}^{\,*}| \quad &\text{and} \quad p_K^* = \sqrt{\frac{s}{4} - m_{K^0}^2} \end{aligned} \tag{5.3}$$

  where $\vec{p}_{\pi^+}^{\,*} + \vec{p}_{\pi^-}^{\,*}$ is the sum of the two pions momenta in the ϕ rest frame and p_K^* is approximately equal to ~ 110 MeV/c, $m_{K^0} \approx 498$ MeV is neutral kaon mass and the value of $\sqrt{s}$ is obtained from Bhabha events on the run-by-run basis.

If more than one vertex satisfies these criteria, then the one closest to the nominal e^+e^- interaction point is identified as the K_S decay vertex. The tagging efficiency for finding $K_S \to \pi^+\pi^-$ and $K_L \to 2\pi$ decays near interaction point amounts to about $\sim$72% [40].

In Fig. 5.5 and Fig. 5.6 distributions of K_L and K_S momenta in the laboratory frame obtained from the two charged particles' system ($|\vec{p}_K| = |\vec{p}_+ + \vec{p}_-|$) and from $\sqrt{s}$ ($|\vec{p}_{K_L}^{\,tag}|$ and $|\vec{p}_{K_S}^{\,tot}|$) are presented. The difference in these two spectra is due to the fact that total momenta of $\vec{p}_{K_L}^{\,tag}$ and $\vec{p}_{K_S}^{\,tot}$ are calculated in the ϕ rest frame as $\sqrt{s}/2$ and corrected with ϕ meson momentum $\vec{p}_\phi$ whereas the direction is taken from tagging. In these momenta distributions, the decrease around 110 MeV/c in number of registered events originates from the fact that in the laboratory frame the emission angles of kaons are not isotropic because of nonzero momentum of the ϕ meson in the laboratory.

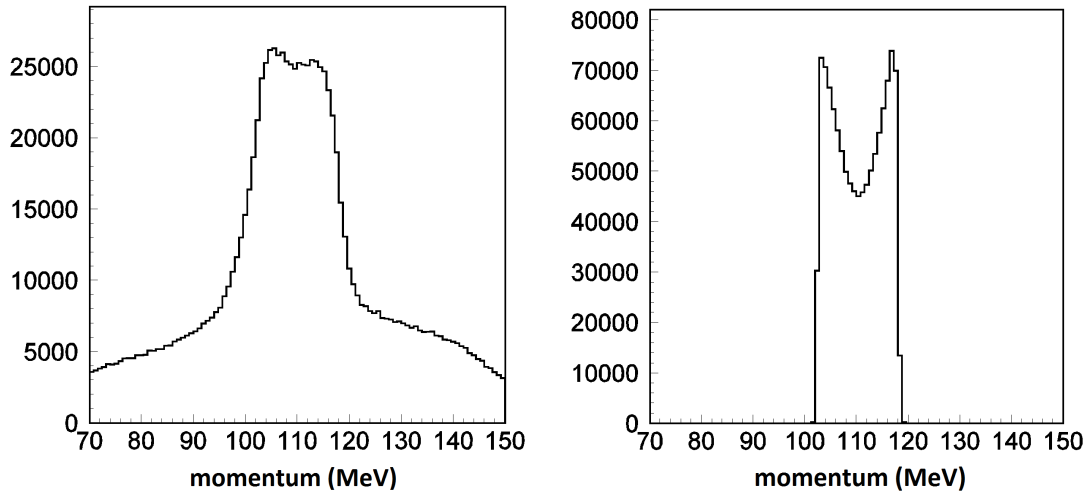

Figure 5.5: Experimental K_L meson momentum distribution obtained from pions momenta (left) and from $|\vec{p}_{K_L}^{\,tag}|$ momentum (right) in the laboratory frame.

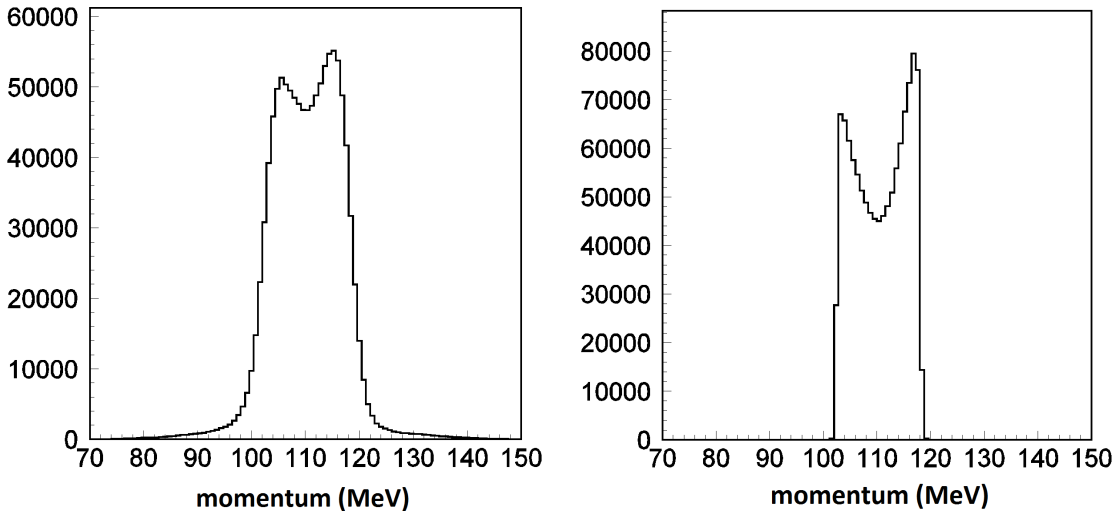

Figure 5.6: Experimental K_S meson momentum distribution obtained from pions momenta (left) and from $|\vec{p}_{K_S}^{\,tot}|$ momentum (right) in the laboratory frame.

Moreover, for finding events $K_S^{reg} \to \pi^+\pi^-$, interesting for regeneration studies, it is additionally required:

- two and only two bent tracks connected to a vertex, corresponding to particles with opposite charge, lying near the K_L tagged line of flight;
- the invariant mass of these two particles (assuming that the observed tracks corresponds to π^+ and π^- mesons) must be within 5 MeV of the neutral kaon mass: $|M_{inv} - m_{K^0}| < 5$ MeV/c.

Finally, for the purpose of this analysis, another cut is applied:

- K_L decays occur up to 50 cm from the interaction point.

5.3 Signal and background events in MonteCarlo

The effect of the described cuts on the data was studied both for the signal and background events, using MonteCarlo simulated sample with an equivalent luminosity of $\sim$1.7 fb^{-1}. Out of $\sim 3.4 \cdot 10^8$ K_L tagged events, $\sim 1.2 \cdot 10^6$ remain after initial cuts described in the previous section. Contributions from various channels are shown in Tab. 5.1. In addition,

%	decay channel	%	decay channel
45.33	$K_L \to \pi^\pm e^\mp \nu_e$	0.54	$K_L \to K_S \to \pi^+\pi^-\gamma$
21.93	$K_L \to K_S \to \pi^+\pi^-$	0.42	$K_L \to \pi^+\pi^-\pi^0$
12.77	$K_L \to \pi^+\pi^-$	0.33	$K_L \to \pi^+\pi^-\gamma$
10.41	$K_L \to \pi^\pm \mu^\mp \nu_\mu$	0.23	$K_L \to \gamma\gamma$
7.42	$K_L \to \pi^\pm e^\mp \nu_e \gamma$	0.12	$K_L \to \pi^0\pi^0\pi^0$

Table 5.1: Components of the MonteCarlo set after initial cuts.

there is about $\sim$ 0.5% of decays originating from nuclear interactions of the K_L meson with calorimeter wall nuclei. As can be inferred from Tab. 5.1, signal events constitute $\sim$ 22% and the dominant sources of background are:

1. $K_L \to \pi^\pm e^\mp \nu_e$ called $Ke3$ where electron is wrongly identified as pion and neutrino is not registered ($\sim$ 45%).
2. CP-violating events $K_L \to \pi^+\pi^-$ ($\sim$ 13%).
3. $K_L \to \pi^\pm \mu^\mp \nu_\mu$ called $K\mu 3$ where muon is wrongly identified as pion and neutrino is not registered ($\sim$ 10%).
4. $K_L \to \pi^\pm e^\mp \nu_e \gamma$ called $Ke3\gamma$ where electron is wrongly identified as pion and both neutrino and gamma are not registered ($\sim$ 7%).

6. General analysis of K_S regeneration in the KLOE detector

The spherical and the cylindrical beam pipe and the drift chamber of the KLOE detector act as regenerators while K_L is traversing them. However, apart from these three materials, one should also expect background events from regenerated kaons in the drift chamber gas and wires and in the air between the beam pipe and the drift chamber [37].

The beam pipe and the drift chamber inner wall of the KLOE detector can be considered as regenerators in which the incoherent process dominates over coherent one (Tab. 4.1). Therefore, due to the smallness of the coherent effect, in this thesis only the measurement of the incoherent regeneration cross-sections on BP and DC is discussed, while the coherent regeneration is only considered as a negligible background.

6.1 Spatial and temporal distributions of kaon decays

After initial selection of data described in Sec. 5.2, a sample of $\phi \to K_S K_L \to \pi^+\pi^-\pi^+\pi^-$ events was extracted including $\phi \to K_S K_L \to \pi^+\pi^- K_S^{reg} \to \pi^+\pi^-\pi^+\pi^-$ events with regeneration but also $CP-$violating $\phi \to K_S K_L \to \pi^+\pi^-\pi^+\pi^-$ decays. In figures 6.1 and 6.2, the spatial distributions of K_S and K_L vertices in planes $y - x$ and $\rho - z$ are shown, where ρ denotes cylindrical coordinate (transverse radius).

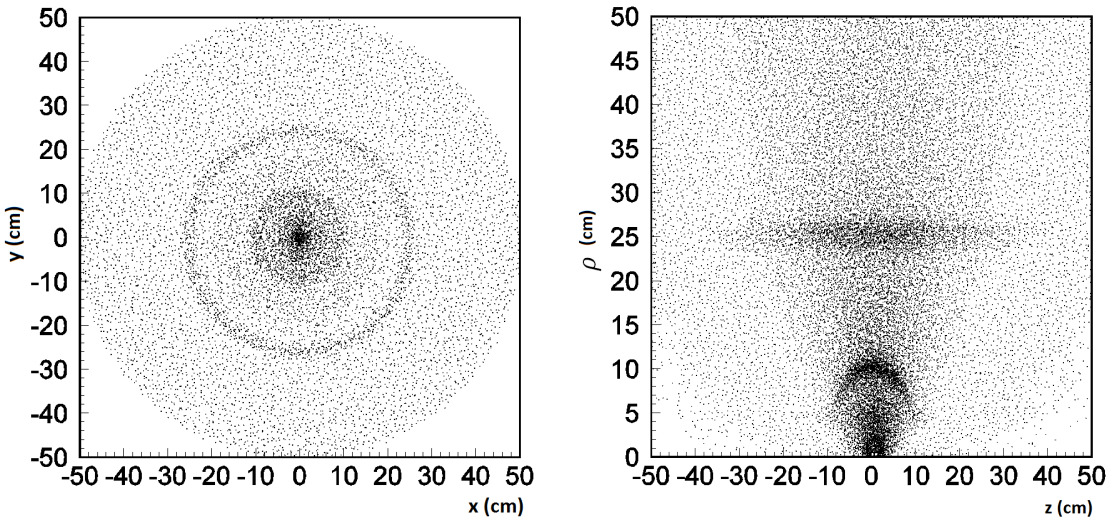

Figure 6.1: Experimental spatial distributions of reconstructed K_L vertex. Left: y versus x, right: ρ versus z.

In Fig. 6.1 is clearly visible the structure induced by the decay points of regenerated events. In the transverse $(x - y)$ plane it is possible to see the cylindrical regenerators (Be and DC) as concentric rings with radii of ∼4.4 cm, ∼25 cm, respectively, and as a circle

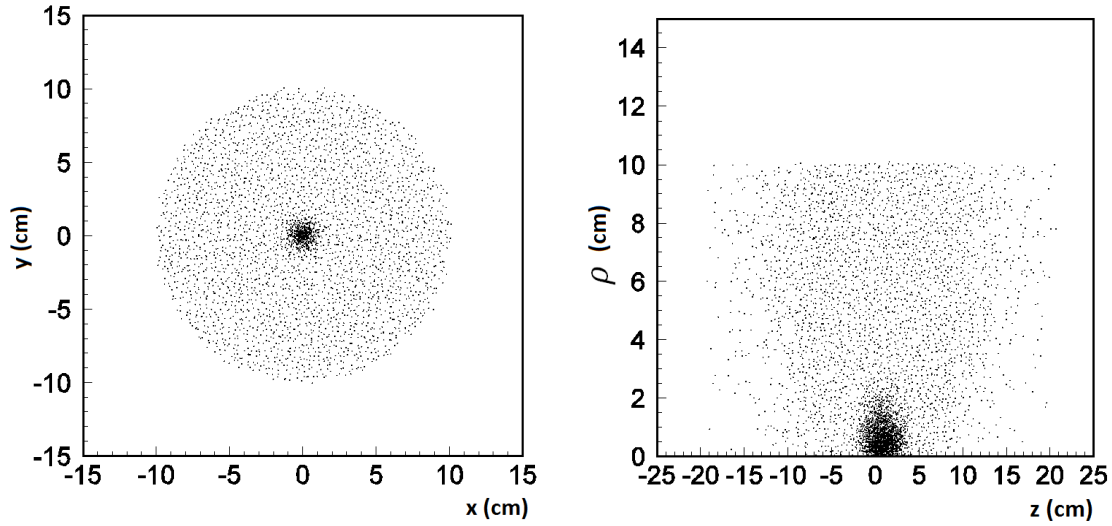

Figure 6.2: Experimental spatial distributions of K_S vertex. Left: y vs x, right: ρ vs z.

with radius of ∼10 cm, while in the polar plane $(\rho - z)$ all the regenerators can be seen according to their geometry: lines for cylinders (Be and DC) and arcs for the spherical one (BP). In the case of K_S decays, in Fig. 6.2 they occur very close to the interaction point, due to its short mean decay length value.

The $K_L \to K_S^{reg} \to \pi^+\pi^-$ regenerated events should be visible as enhancement close to the regenerators' positions in the K_L decay distance distribution, where this distance is calculated taking into account ϕ decay point $\vec{x}_\phi$:

$$d_{L,S} = \sqrt{(x_{L,S} - x_\phi)^2 + (y_{L,S} - y_\phi)^2 + (z_{L,S} - z_\phi)^2} \tag{6.1}$$

and where $\vec{x}_{K_{L,S}} = (x_{L,S}, y_{L,S}, z_{L,S})$ is kaon vertex. Indeed, in the right panel of $d_{L,S}$ distributions in Fig. 6.3, one can see peaks at: ∼4.4 cm, ∼10 cm and ∼25 cm. In the left panel also distribution for K_S is shown and its mean value agrees with kaon mean decay length equal to ∼0.6 cm. In both distributions the width of a bin equal to $1\tau_S \sim 0.6$ cm corresponds to the experimental resolution of the KLOE detector.

Increase in number of counts for K_L decays is reflected also in the K_L proper decay time distribution. The proper decay time of kaons is calculated as:

$$t^*_{L,S} = \frac{t_{L,S}}{\gamma} = \frac{1}{\gamma}\frac{d_{L,S}}{v_{L,S}}, \qquad \text{where} \qquad v_{L,S} = c \cdot \beta_{L,S},$$
$$\beta_{L,S} = \frac{|\vec{p}^{\,\pi^+}_{L,S} + \vec{p}^{\,\pi^-}_{L,S}|}{\sqrt{|\vec{p}^{\,\pi^+}_{L,S} + \vec{p}^{\,\pi^-}_{L,S}|^2 + m^2_{K^0}}} \qquad \text{and} \qquad \gamma_{L,S} = \frac{1}{\sqrt{1 - \beta^2_{L,S}}} \tag{6.2}$$

Here $\gamma_{L,S}$ denotes the Lorentz factor, $\beta_{L,S}$ is velocity of K_L and K_S in the laboratory frame and c is the velocity of light. In Fig. 6.4, the proper decay times distributions for both K_S and K_L are presented. For K_S the mean value agrees with its mean decay time equal to ∼0.9 ns.

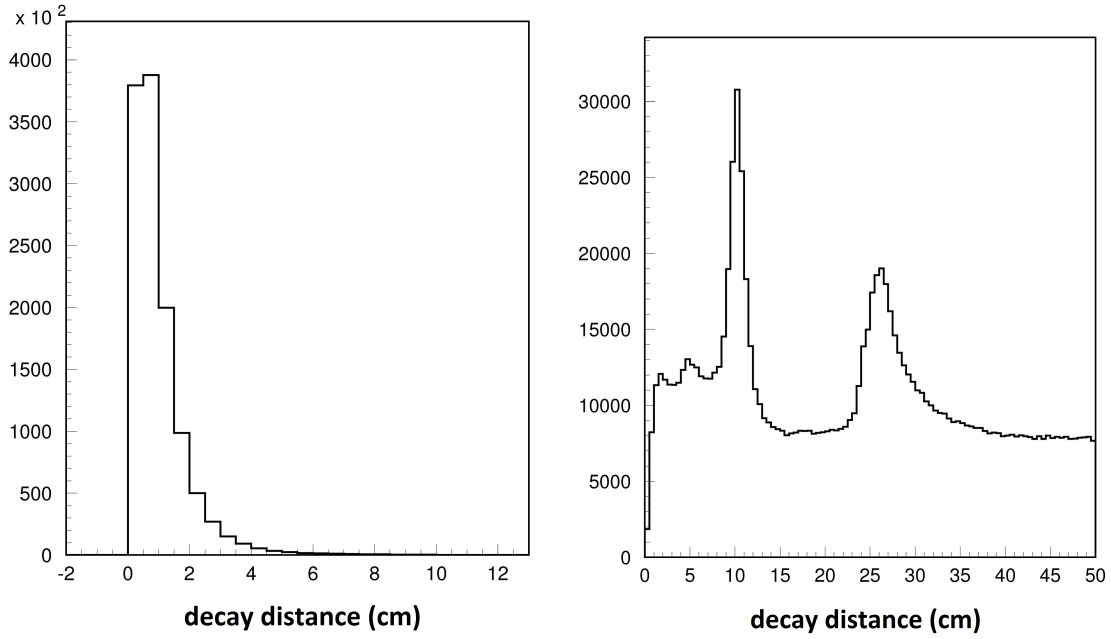

Figure 6.3: Experimental distributions of kaon decay distances. Left: K_S, right: K_L.

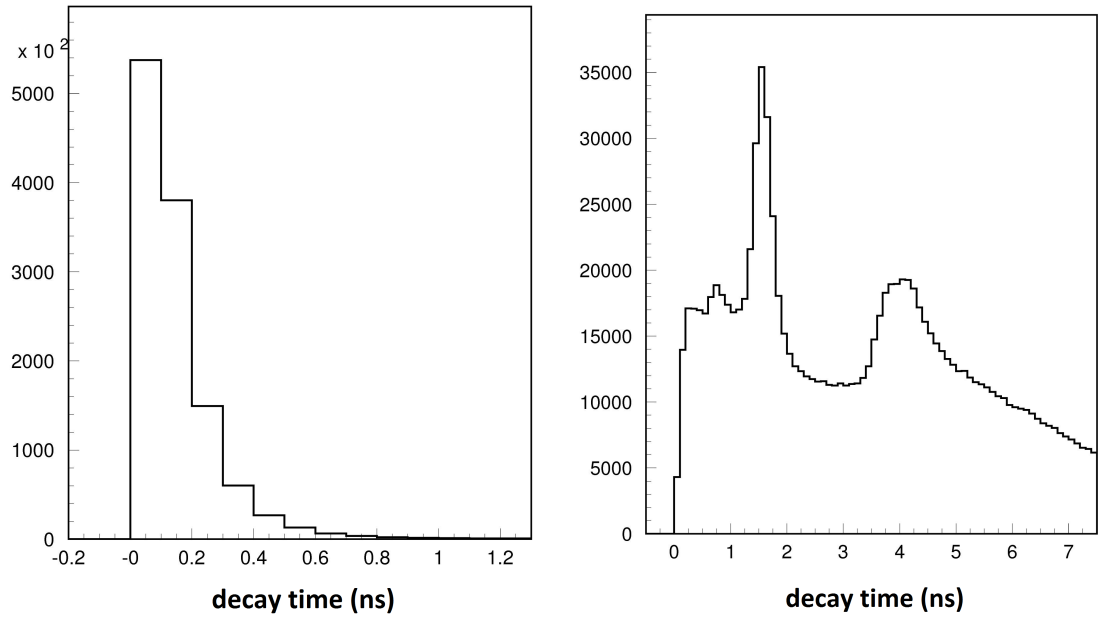

Figure 6.4: Experimental distributions of kaon proper decay times. Left: K_S, right: K_L.

Another very useful distributions are K_L decay distances in ρ and r coordinates, where ρ and r read:

$$\begin{aligned} r &= \sqrt{x_{K_L}^2 + y_{K_L}^2 + z_{K_L}^2} \\ \rho &= \sqrt{x_{K_L}^2 + y_{K_L}^2} \end{aligned} \tag{6.3}$$

As the drift chamber inner wall and the beryllium beam pipe are cylindrical, the $K_L \to K_S$ regeneration is visible in ρ distribution as symmetrical peaks (Fig. 6.5) whereas regeneration in the spherical beam pipe manifests itself as a symmetrical enhancement in r distribution (Fig. 6.6). Experimental results are shown in the left panels and results of the MonteCarlo simulations in the right panels. In the latter, regeneration as well as main background components originating from semileptonic and $CP-$violating events are shown. Absolute values of simulated contributions were adjusted according to the total luminosity and corresponding branching ratios.

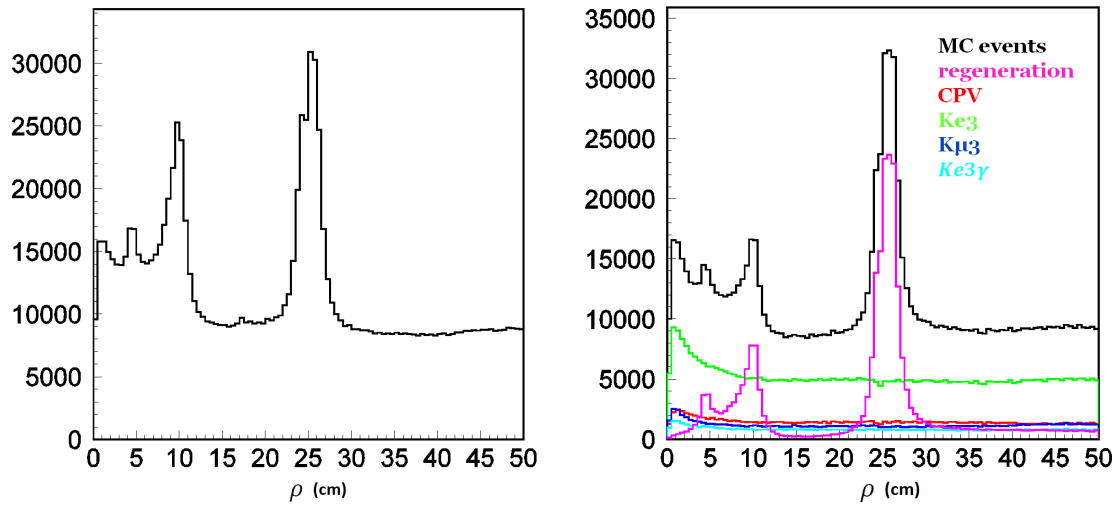

Figure 6.5: Distributions of K_L decay distances in ρ coordinate. Left: data, right: MonteCarlo simulations.

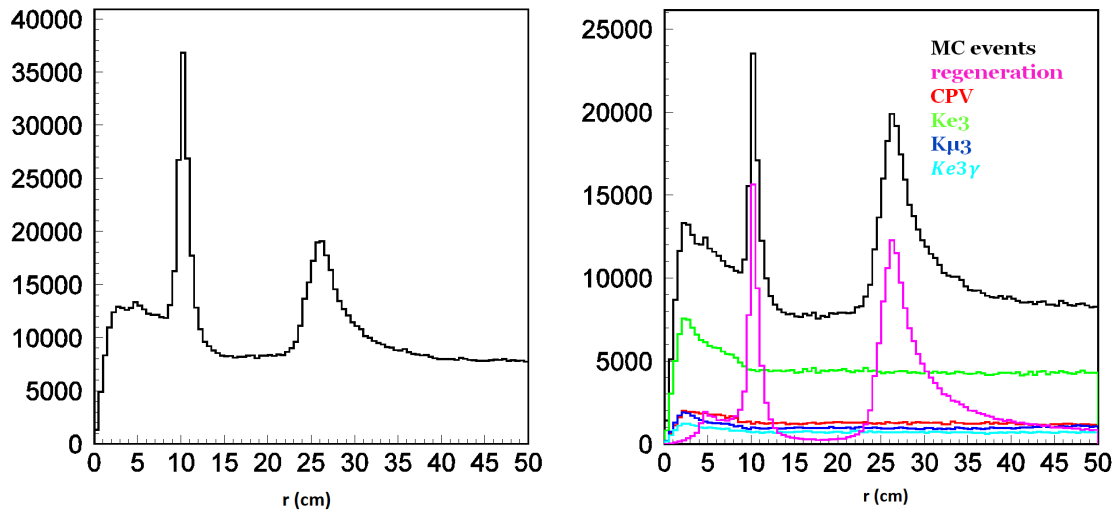

Figure 6.6: Distributions of K_L decay distances in r coordinate. Left: data, right: MonteCarlo simulations.

Now one can plot the regenerated K_S (K_S^{reg}) decay length distributions for appropriate fiducial volumes, defined as:

$$\begin{aligned} Be &: \quad 3.4 < \rho < 5.4 \text{ cm}, \ |z| < 1 \text{ cm} \\ BP &: \quad 9 < r < 11 \text{ cm} \\ DC &: \quad 24 < \rho < 26 \text{ cm}, \ |z| < 1 \text{ cm} \end{aligned} \tag{6.4}$$

so ±1cm from the regenerating surfaces. This is very tight cut to assure that only regenerated events are accepted.

The reconstruction of the flight path l of K_S^{reg} is calculated as a difference between K_L^{tag} impact point on the regenerator and the $K_S^{reg} \to \pi^+\pi^-$ vertex. The first one is obtained by looking for the point of intersection of K_L^{tag} line of flight with cylinder (for regeneration in the Be and DC) or with sphere (for BP). For the detailed calculations the reader is referred to Appendix C. The decay length l of regenerated K_S reads:

$$l = \sqrt{(x_{K_L} - x)^2 + (y_{K_L} - y)^2 + (z_{K_L} - z)^2},$$

where $\vec{x}_{K_L} = (x_{K_L}, y_{K_L}, z_{K_L})$ are coordinates of $K_L \to K_S^{reg} \to \pi^+\pi^-$ vertex for appropriate fiducial volumes and (x, y, z) denote coordinates of the K_L^{tag} impact point. Both of them are illustrated in Fig. 6.7.

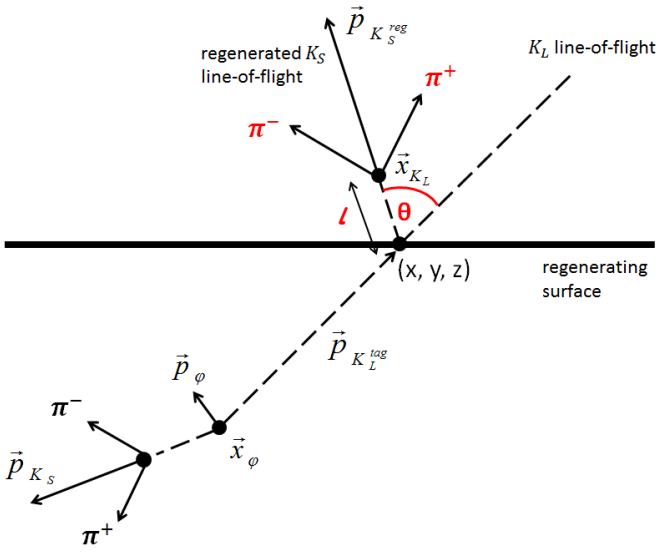

Figure 6.7: Illustration of reconstruction of the K_S^{reg} decay length l.

In the left panel of Fig. 6.8, distributions of the decay distances l for all three regenerators are presented. After detailed examination one can see that for the drift chamber (DC), the mean value is slightly different from K_S mean decay length equal to ∼0.6 cm. This is due to the very tight fiducial volume cut (6.4) and the fact that the KLOE drift chamber is shifted slightly down with respect to the reconstruction coordinate system. In the right panel of Fig. 6.8 the proper decay times are shown, calculated according to equation (6.2). Also here, for DC there are deviations from the mean value equal to ∼0.9 ns and the reasons for this are the same.

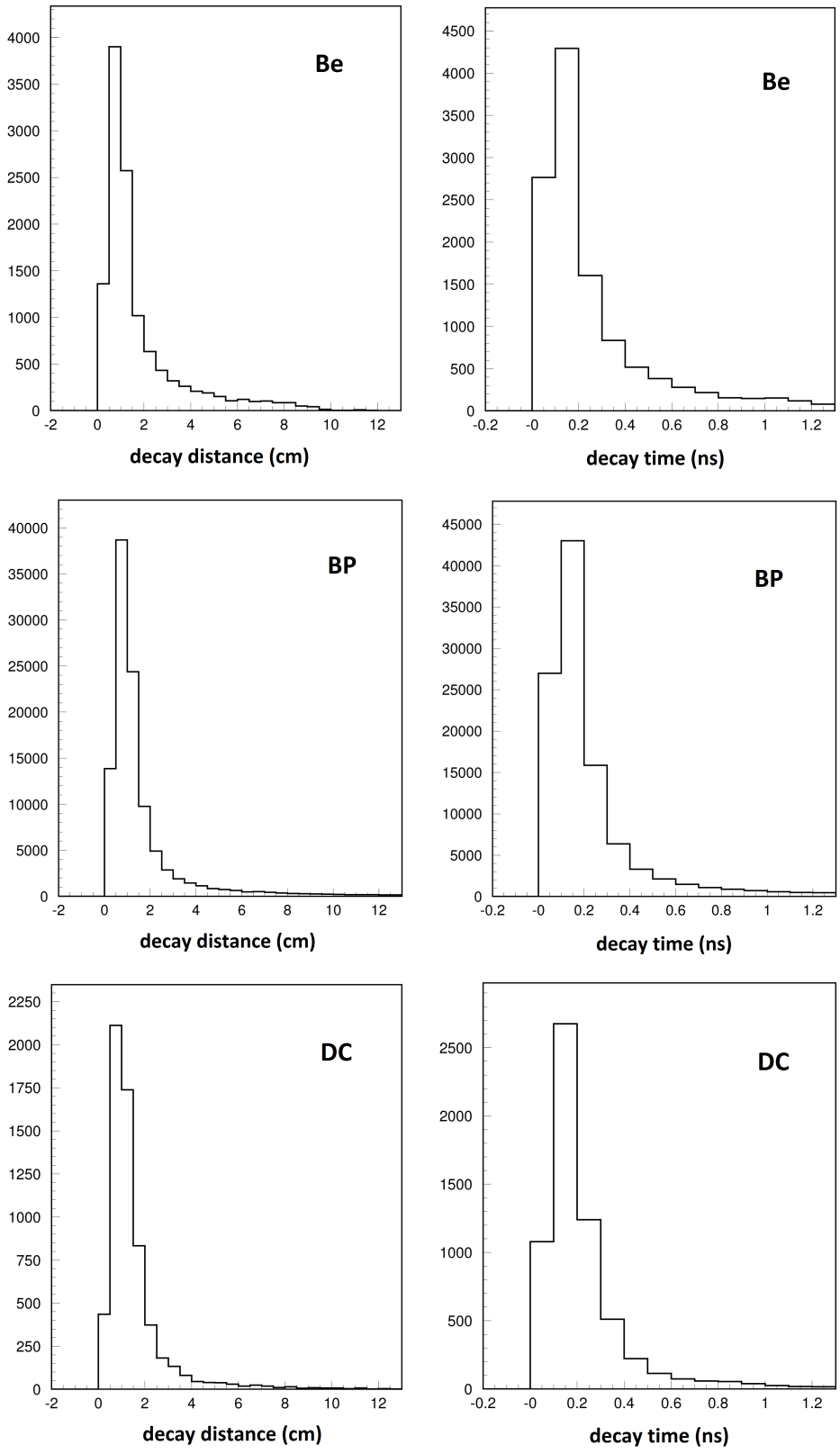

Figure 6.8: Experimental distributions of regenerated K_S decay distances (left) and times (right) for appropriate regenerators (as indicated in the figures).

6.2 K_L semileptonic decays

In the simulated sample the background for regenerated events consists mostly of semileptonic decays as can be inferred from Tab. 5.1. In fact $K_L \to \pi^{\pm}e^{\mp}\nu_e$ ($Ke3$), $K_L \to \pi^{\pm}\mu^{\mp}\nu_\mu$ ($K\mu 3$) and $K_L \to \pi^{\pm}e^{\mp}\nu_e\gamma$ ($Ke3\gamma$) decays constitute $\sim 63\%$ of all events. They are misidentified as $\pi^+\pi^-$ events because of wrong identification of electron or muon as a pion. Hence, value of the invariant mass of the two charged particles from semileptonic decays should be less than invariant mass of $\pi^+\pi^-$ system from K_S^{reg} decay and in this way one can suppress most of the semileptonic background. To do so the cut $|M_{inv} - m_{K^0}| < 5$ MeV/c was already applied in Sec. 5.2, where invariant mass was explicitly calculated as:

$$M_{inv} = \sqrt{2(m_\pi^2 + \sqrt{(m_\pi^2 + |\vec{p}_{\pi^+}|^{\,2})(m_\pi^2 + |\vec{p}_{\pi^-}|^{\,2})} - \vec{p}_{\pi^+} \cdot \vec{p}_{\pi^-})} \tag{6.5}$$

In Fig. 6.9 the distribution of the difference between the K_L invariant mass and nominal neutral kaon mass ($M_{inv} - m_{K^0}$) after the applied cut is shown.

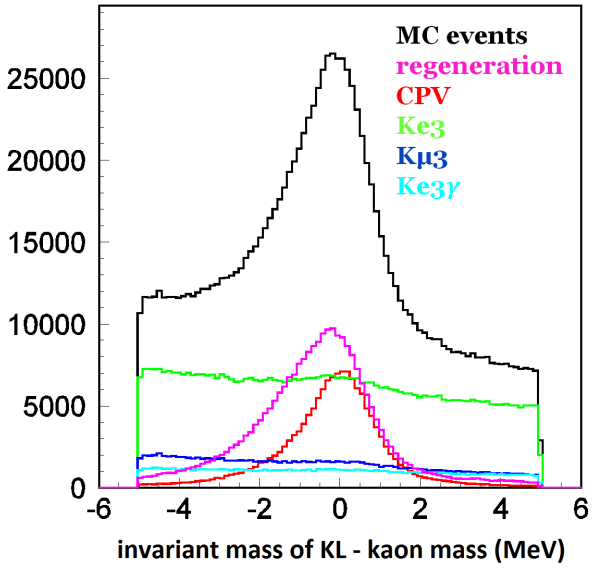

Figure 6.9: Simulated distribution of difference between reconstructed K_L invariant mass and nominal kaon mass.

Another very useful variable for distinguishing background components is Q_{miss}:

$$Q_{miss} = \sqrt{E_{miss}^2 + |\vec{p}_{miss}|^2}, \tag{6.6}$$

where missing energy E_{miss} and missing momentum $\vec{p}_{miss}$ read:

$$E_{miss} = E_{K_L} - E_{\pi^+} - E_{\pi^-} = \sqrt{m_{K^0}^2 + |\vec{p}_{K_L}|^2} - \sqrt{m_\pi^2 + |\vec{p}_{\pi^+}|^2} - \sqrt{m_\pi^2 + |\vec{p}_{\pi^-}|^2}$$

$$|\vec{p}_{miss}| = |\vec{p}^{\,\prime tag}_{K_L} - \vec{p}_{\pi^+} - \vec{p}_{\pi^-}| \tag{6.7}$$

and $\vec{p}^{\,\prime tag}_{K_L}$ denotes K_L^{tag} momentum calculated based on $\sqrt{s}$ and the supposed direction for the tagged kaon. $\vec{p}_{\pi^+}$, $\vec{p}_{\pi^-}$ are momenta of charged particles originating from K_L decay and E_{π^+} and E_{π^-} are calculated assuming that the charged particles where pions.

In fact the distribution of Q_{miss} enables to distinguish very clearly $CP-$violating events from most of all the other components. It is visible in Fig. 6.10 where $CP-$violating events appear as a peak for small values of Q_{miss} variable. Semileptonic events manifest themselves as symmetrical peaks around ~ 20 MeV and ~ 50 MeV whereas regenerated events cover full range from 0 to ~ 180 MeV. One can also plot $Q_{miss}(M_{inv} - M_K)$ distribution (Fig. 6.11) where regenerated events appear as vertical line for values equal to zero.

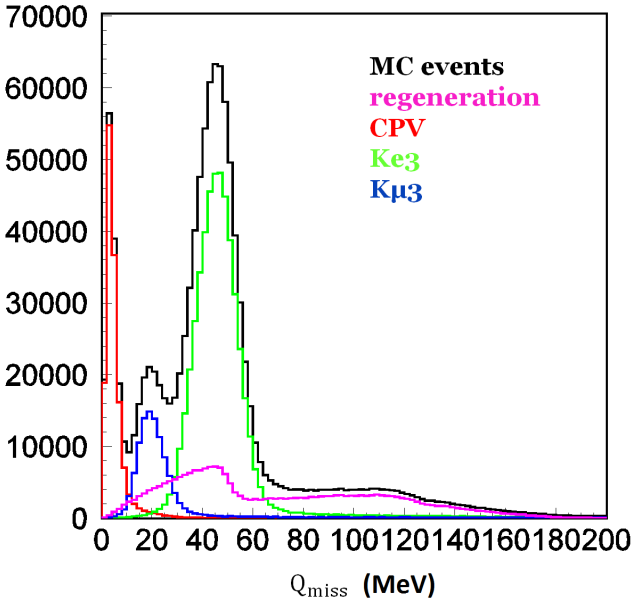

Figure 6.10: Simulated distribution of Q_{miss} variable.

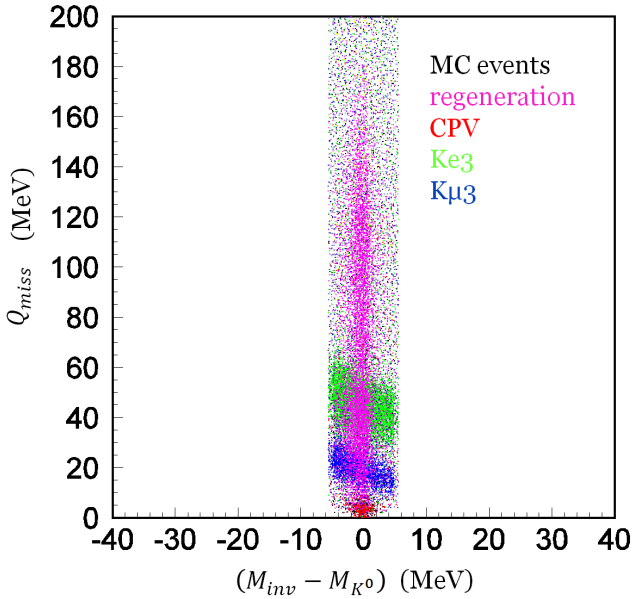

Figure 6.11: Simulated distribution of $Q_{miss}(M_{inv} - M_K)$. The applied K_L invariant mass cut ± 5 MeV around neutral kaon mass is here visible.

While the Q_{miss} distribution allows separation of $CP-$violating events from regenerated ones, most semileptonic background that was not reduced by invariant mass cut can be suppressed by using Δp variable, defined as:

$$\Delta\,|\vec{p}\,| = \left|\vec{p}_{K_L}^{\,tag}\right| - |\vec{p}_{\pi^+} + \vec{p}_{\pi^-}| \tag{6.8}$$

where definitions of variables are the same as for Q_{miss}. The Δp distribution of simulated events is shown in Fig. 6.12 where it is possible to notice that regenerated events also occur for the values greater than 10 MeV/c. One can infer that it is due to the fact that there is some momenta transfer to regenerator during regeneration and this difference between momentum of K_L^{tag} and from both reconstructed pions may be interpreted as inelastic regeneration in the material nuclei that is simulated in MonteCarlo. This events can be also visible in the $Q_{miss}(\Delta p)$ distribution. In the right panel of Fig. 6.13 one can see that some of regenerated events are visible as bent line. However, this events are not visible in the data in the left panel of Fig. 6.13, so one can infer that inelastic regeneration is simulated in the KLOE MonteCarlo with weight that is not properly set. Hence, one can apply Δp cut in the range where there are also $CP-$violating events (i.e. $-10 < \Delta p < 20$) MeV/c and by doing this suppress most of the semileptonic background.

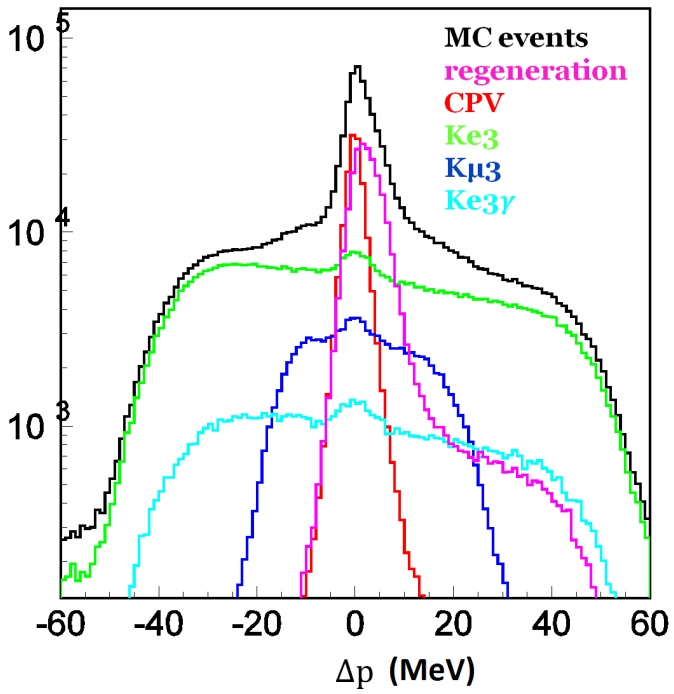

Figure 6.12: Simulated distribution of Δp variable. As indicated inside the figure, contributions from various decays are given in descending order, starting from total contribution and further with regeneration, CPV, $Ke3$, $K\mu 3$, $Ke3\gamma$.

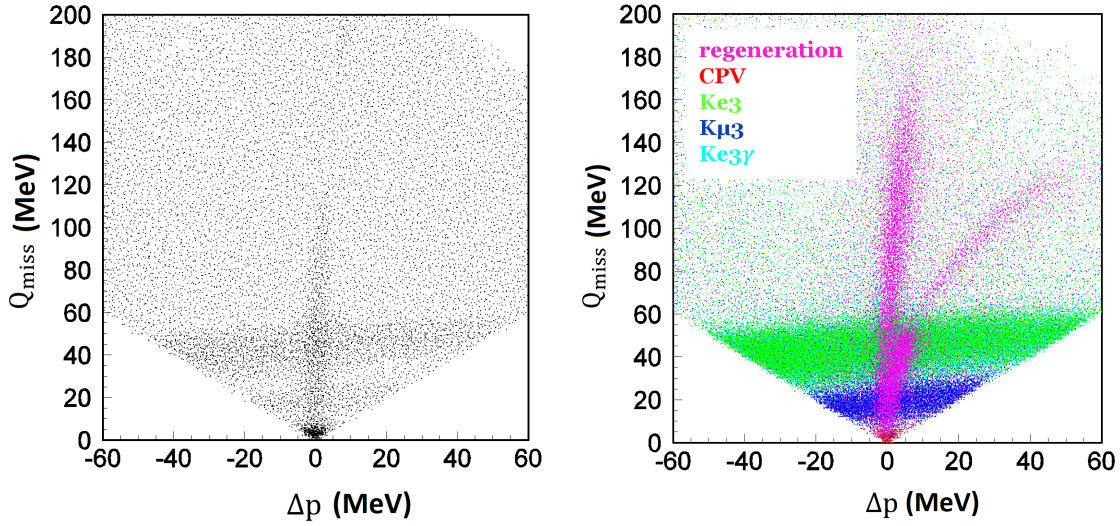

Figure 6.13: $Q_{miss}(\Delta p)$ distributions. Left: data, right: MonteCarlo simulations.

6.3 Regeneration angle distributions

At KLOE maximum angle for coherent regeneration is equal to $\vartheta_{max} \approx 10^{-6}$ rad (4.13) and the probability of coherent regeneration is about two orders of magnitude smaller than for incoherent one (Tab. 4.1). Hence, regeneration at KLOE occurs mostly incoherently with the change of the direction of kaon momentum under some ϑ angle. In Fig. 6.14 this angle is schematically presented.

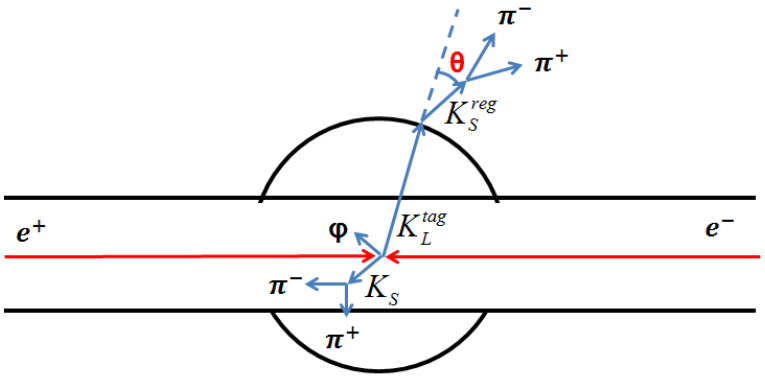

Figure 6.14: Scheme illustrating definition of the regeneration angle.

The regeneration angle is defined as:

$$\vartheta = \text{acos}\ \frac{\vec{p}_{K_L}^{\,tag} \cdot (\vec{p}_{\pi^+} + \vec{p}_{\pi^-})}{|\vec{p}_{K_L}^{\,tag}| \cdot |\vec{p}_{\pi^+} + \vec{p}_{\pi^-}|}. \tag{6.9}$$

Fig. 6.15 shows distributions of this angle. The left plot shows experimental results whereas the right one is obtained from the MonteCarlo simulations. In the latter one can see that contributions originating from different decays are distributed around different angles. For

regenerated events the maximum is seen at angle equal to $\sim 25°$ and also an enhancement is seen at angle of about $\sim 60°$. These two peaks originate from different material composition of the beam pipe (25°) and the drift chamber inner wall (60°). $CP-$violating events correspond to maximum at $\sim 2°$ since they occur without change of the momentum direction. $K\mu 3$ decays are visible around $\sim 10°$ while $Ke3$ and $Ke3\gamma$ around $\sim 20°$.

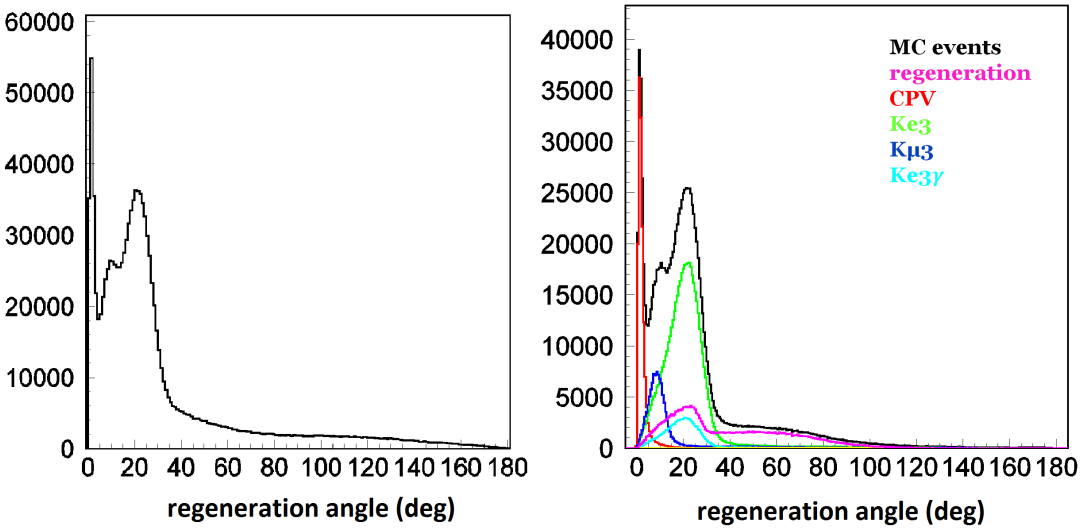

Figure 6.15: Regeneration angle distribution. Left: data, right: MonteCarlo simulations.

These different angular distributions of semileptonic decays originate from the fact that electron and muon have not the same masses. In the selected events of $Ke3$, $K\mu 3$ and $Ke3\gamma$ decays neutrino carries small momentum fraction due to the invariant mass cut around neutral kaon mass. Hence, in $Ke3$ decay electron gains higher momentum than muon in $K\mu 3$ because electron is lighter. Therefore, ϑ angle will be bigger for semileptonic decays with electrons and so one can infer that maxima in Fig. 6.15 at $\sim 10°$ and $\sim 20°$ are due to the kinematic cuts applied in the analysis.

One can also plot distribution of regeneration angle versus transverse radius $\vartheta(\rho)$ (Fig. 6.16) and distribution of kaon momentum from two registered charged particles versus regeneration angle $p(\vartheta)$ (Fig. 6.17). Here also semileptonic events are spread at certain angles whereas regenerated events cover all angular range.

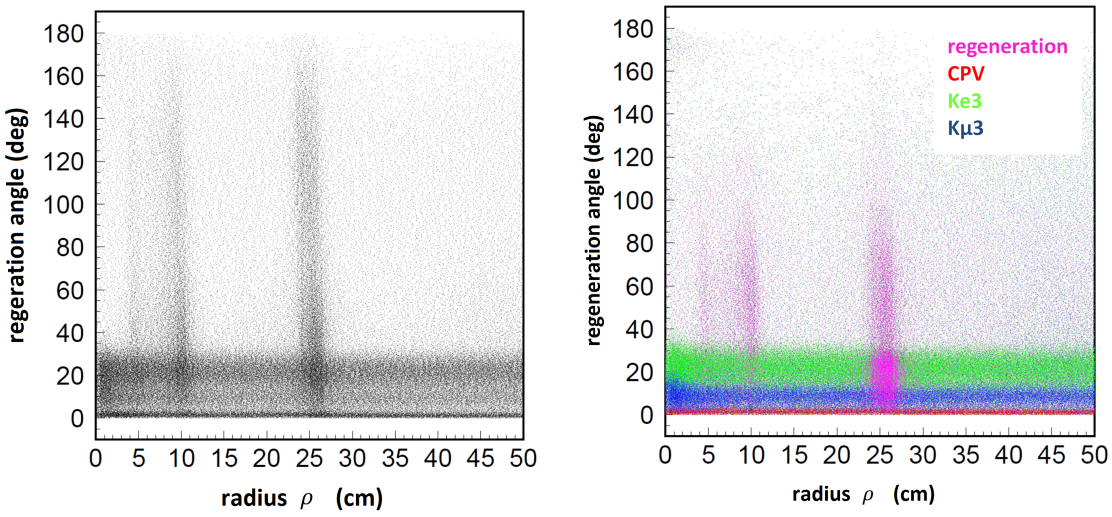

Figure 6.16: Regeneration angle versus transverse radius ρ distributions. Left: data, right: MonteCarlo simulations.

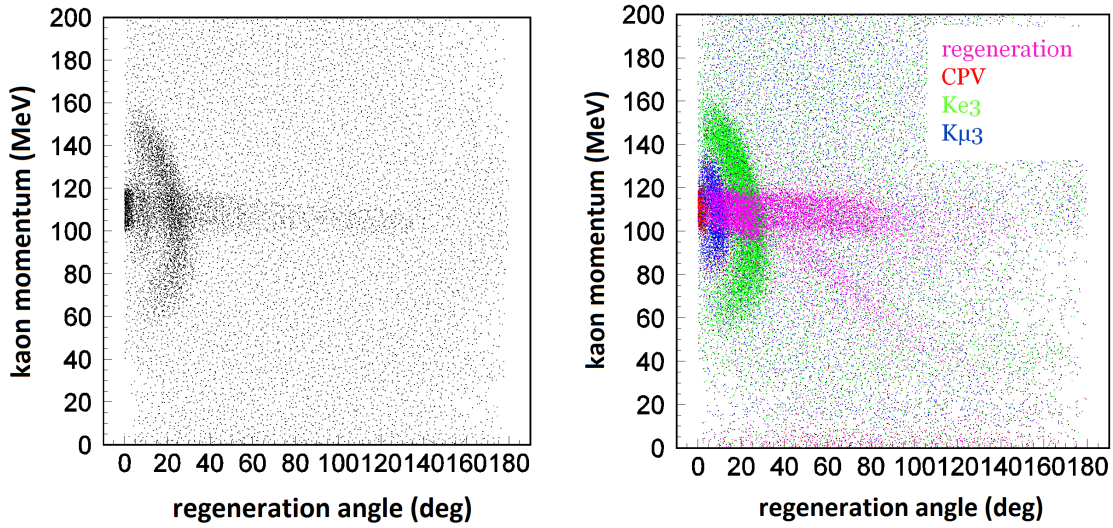

Figure 6.17: Distributions of kaon momentum obtained from two registered charged particles versus regeneration angle. Left: data, right: MonteCarlo simulations.

7. Regeneration signal selection

In order to extract number of regenerated events and to minimize the background additional cuts concerning regeneration signal selection were performed and are described in this chapter. Since the closest regenerators are ~ 4.4 cm and ~ 10 cm from the interaction point, further cuts on identification of the K_S meson originating from the ϕ meson decay were carried out so as not to misidentified them with regenerated K_S^{reg} decays. The cuts were applied on the following variables:

- K_S invariant mass,
- K_S vertex position,
- K_S momentum nominal value in the ϕ rest frame.

Moreover, in order to select regenerated $K_L \to K_S^{reg} \to \pi^+\pi^-$ decays and to separate peaks originating from both beam pipe regenerators, two cuts were also performed on:

- total momentum difference between K_L and $\pi^+\pi^-$,
- K_L^{tag} tagged polar angle.

Quantitative description of the applied cuts follows in the next sections.

7.1 Background suppression

7.1.1 K_S invariant mass distribution

The first selection requirement is that invariant mass of K_S must stay in the range:

$$492.5 \text{ MeV} < M_{inv} < 502.5 \text{ MeV},$$

where (5.2):

$$M_{inv}^2 = E_{tot}^2 - |\vec{p}_{tot}|^2.$$

In Fig. 7.1 this distribution is presented with marked selection area.

7.1.2 K_S decay vertex

Another cut is K_S vertex position that must stay in the fiducial volume defined as (5.1):

$$\rho < 2 \text{ cm}, \quad |z_{K_S} - z_\phi| < 3 \text{ cm}.$$

In Fig. 7.2 the distribution of K_S vertex position is shown with selection area marked by blue arrows.

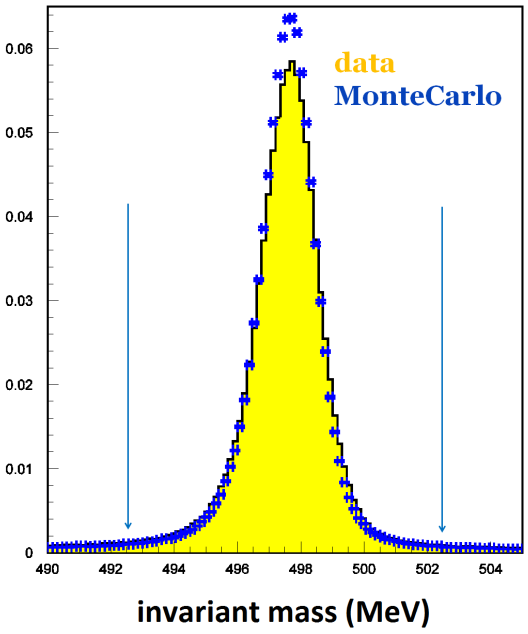

Figure 7.1: Distribution of invariant mass of K_S obtained from data (yellow) and from the MonteCarlo simulations (blue). Differences are due to the resolution differences. Arrows indicate selection area and the distributions are normalized to unity.

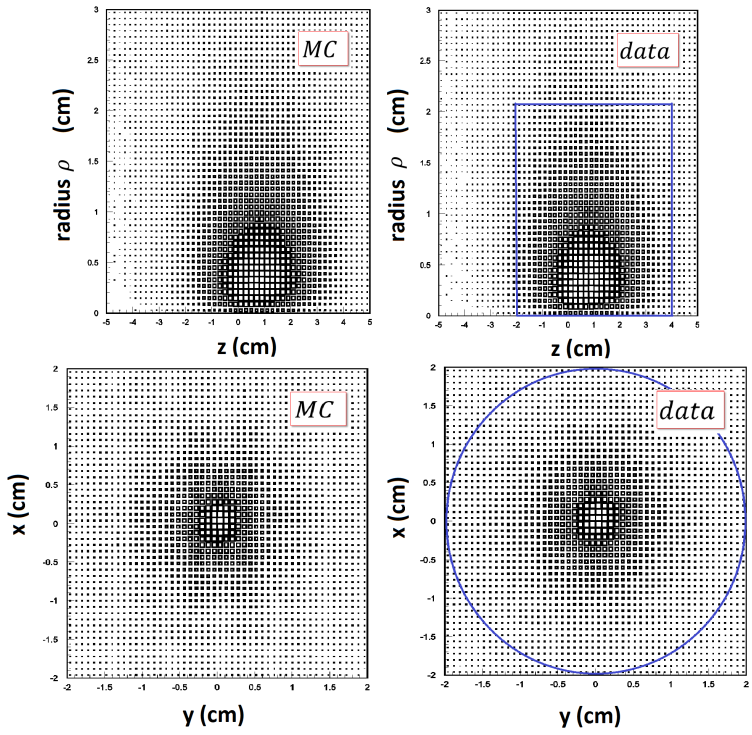

Figure 7.2: Distributions of K_S vertex position in $\rho - z$ (first row) and $x - y$ plane (second row). The selection area is marked in blue. Note that in the upper panel the axes have not the same scale.

7.1.3 K_S momentum distribution

The last cut on the K_S meson kinematics is its momentum nominal value in the ϕ rest frame, that reads (5.3):

$$\left| |\vec{p}^{\,*}_{\pi^+} + \vec{p}^{\,*}_{\pi^-}| - \sqrt{\frac{s}{4} - m^2_{K^0}} \right| < 10 \text{ MeV/c}$$

The Lorentz transformation of pion momentum into the ϕ rest frame ($\vec{p}^{\,*}_{\pi^+}$ and $\vec{p}^{\,*}_{\pi^-}$) was performed as:

$$\vec{p}^{\,*}_{\pi} = \vec{p}^{\,lab}_{\pi} + \gamma\vec{\beta}_{\phi}\left(\frac{\gamma}{\gamma+1}\vec{\beta}_{\phi}\cdot\vec{p}^{\,lab}_{\pi} - E_{\pi}\right),$$

where $\vec{\beta}_{\phi} = \frac{\vec{p}_{\phi}}{E_{\phi}}$ and $\vec{p}^{\,lab}_{\pi}$ is pion momentum vector in the laboratory frame, $\gamma = 1/\sqrt{1-|\vec{\beta}_{\phi}|^2}$ and $E_{\pi} = \sqrt{m^2_{\pi} + |\vec{p}^{\,lab}_{\pi}|^2}$.

In Fig. 7.3 this distribution with marked selection area is presented. After all the cuts made on K_S in this chapter one is assured that clear K_S sample is selected.

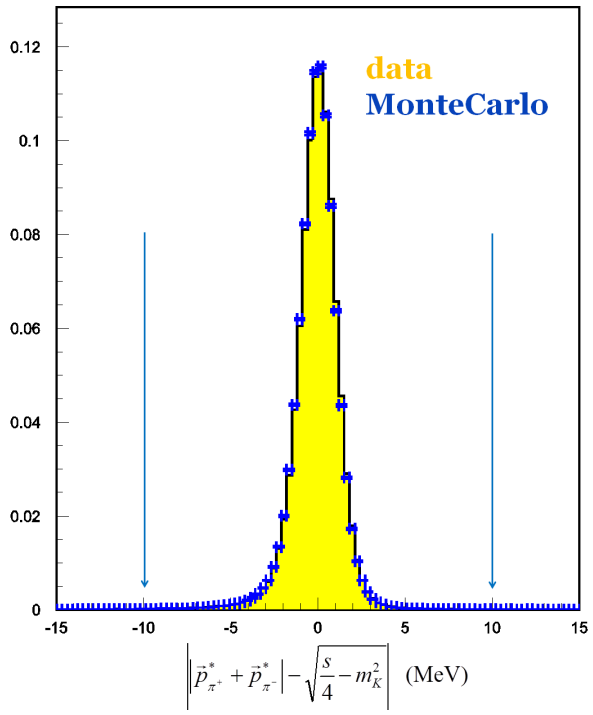

Figure 7.3: Distribution of a difference between reconstructed and expected value of the K_S meson momentum in the ϕ meson rest frame. Arrows indicate selection area and the distributions are normalized to unity.

7.1.4 Total momentum difference between K_L^{tag} and $\pi^+\pi^-$

The most efficient selection of regenerated events by which also background is much suppressed is Δp variable cut, that is the total momentum difference between K_L^{tag} and $\pi^+\pi^-$

defined as (6.8):

$$\Delta|\vec{p}| = |\vec{p}_{K_L}^{\,tag}| - |\vec{p}_{\pi^+} + \vec{p}_{\pi^-}|.$$

It is shown in Fig. 7.4, where selection area is marked, that it is required that the values of Δp must stay in a range:

$$-10 \text{ MeV} < \Delta p < 20 \text{ MeV}.$$

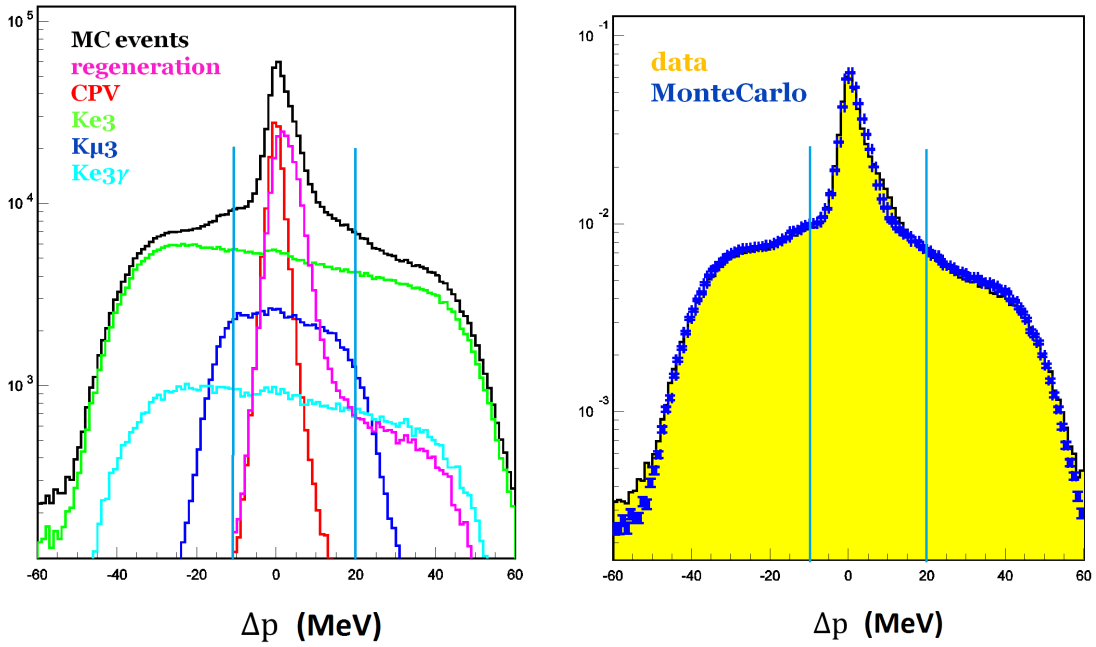

Figure 7.4: Distribution of Δp variable obtained after all previous cuts from the MonteCarlo simulations (left and right blue) and from data (right yellow). The selection area is marked by blue lines and the distributions are normalized to unity.

Cut	S/B (%)
initial cuts	21.3
M_{inv} of K_S	22.4
K_S vertex position	22.5
p_{K_S} nominal value	22.5
Δp	43.0

Table 7.1: Signal to background ratio for kaons decaying within Be-BP fiducial volume: $0 < \rho < 16$ cm.

By applying the above cut, the background is much reduced and the signal to background ratio (S/B) is nearly twice amplified as can be inferred from Tab. 7.1. In this table S/B values determined in a range $0 < \rho < 16$ cm are quoted and after all cuts discussed in this section. This fiducial volume comprises the cylindrical (Be) and the spherical (BP) beam pipe region.

7.2 Separation of regeneration maxima in transverse radius distribution

The aim of all the previous cuts was to decrease background in regeneration signal selection, especially in the region where both beam pipe regenerators are situated ($0 < \rho < 16$ cm). However, in this region peak from regeneration in the cylindrical beam pipe around $\sim$ 4.4 cm and in the spherical beam pipe $\sim$ 10 cm overlap as can be seen in Fig. 7.5.

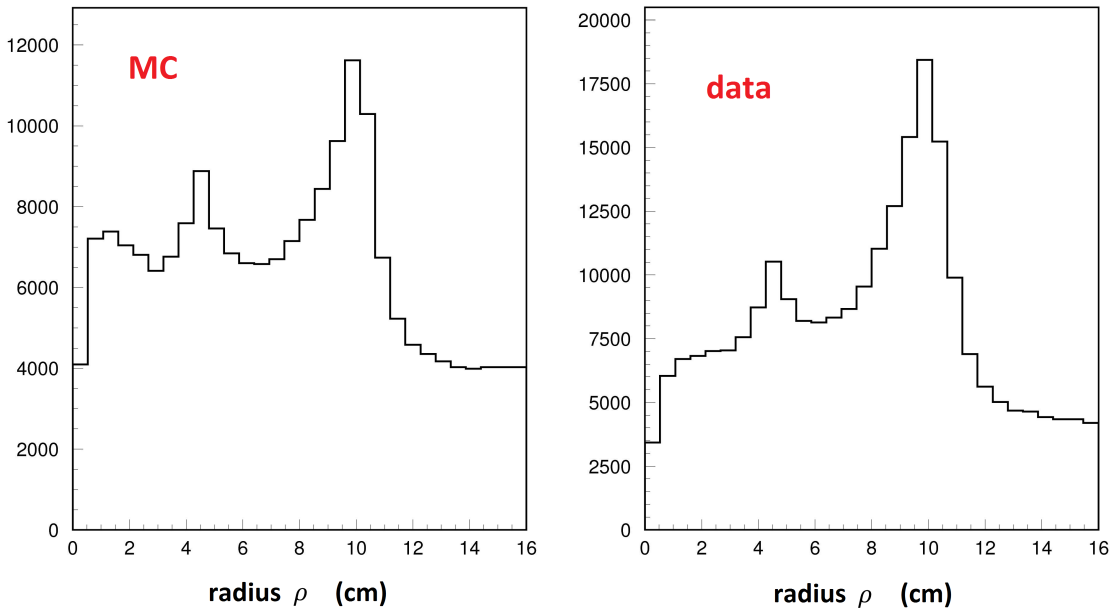

Figure 7.5: Distributions of registered K_L decay vertex positions, as determined after cuts described in the previous sections, obtained from data (right) and the MonteCarlo simulations (left).

Hence, additional constraint is imposed on the angle between momentum vector of tagged K_L and z axis (polar angle θ) in order to exclude from the analysis a region where BP and and Be are close to each other. This angle is schematically presented in Fig. 7.6 and marked by red color. The applied cut is shown in Fig. 7.7 and is equal to:

$$\theta = \sphericalangle(K_L\ tag, z) \in (60^\circ; 120^\circ).$$

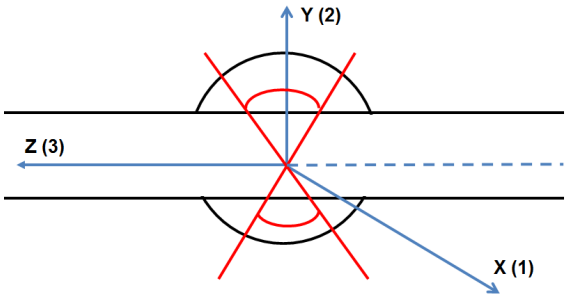

Figure 7.6: Schematically presented range of K_L polar angle used in the analysis.

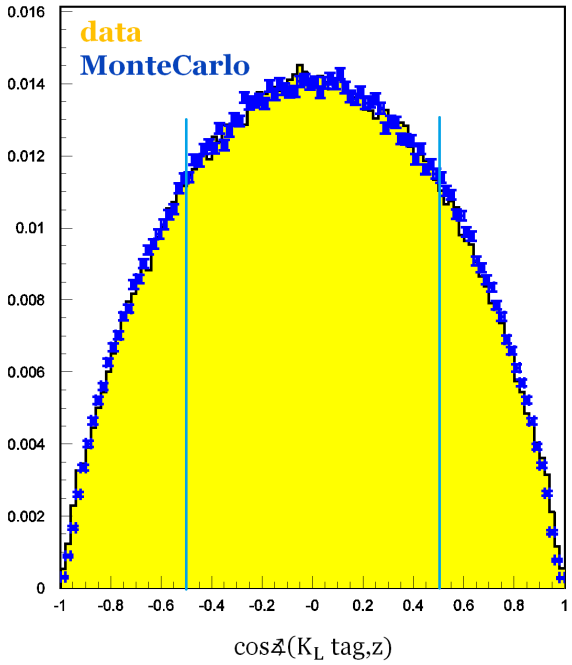

Figure 7.7: Distribution of K_L polar angle obtained from data (yellow) and MonteCarlo (blue). The selection area is marked by blue lines and the distributions are normalized to unity.

After K_L polar angle cut the signal to background ratio increases to: S/B=45.5%. In Fig. 7.8 transverse radius distribution is shown for events for which $\theta = \sphericalangle(K_L\ tag, z) \in (60°; 120°)$.

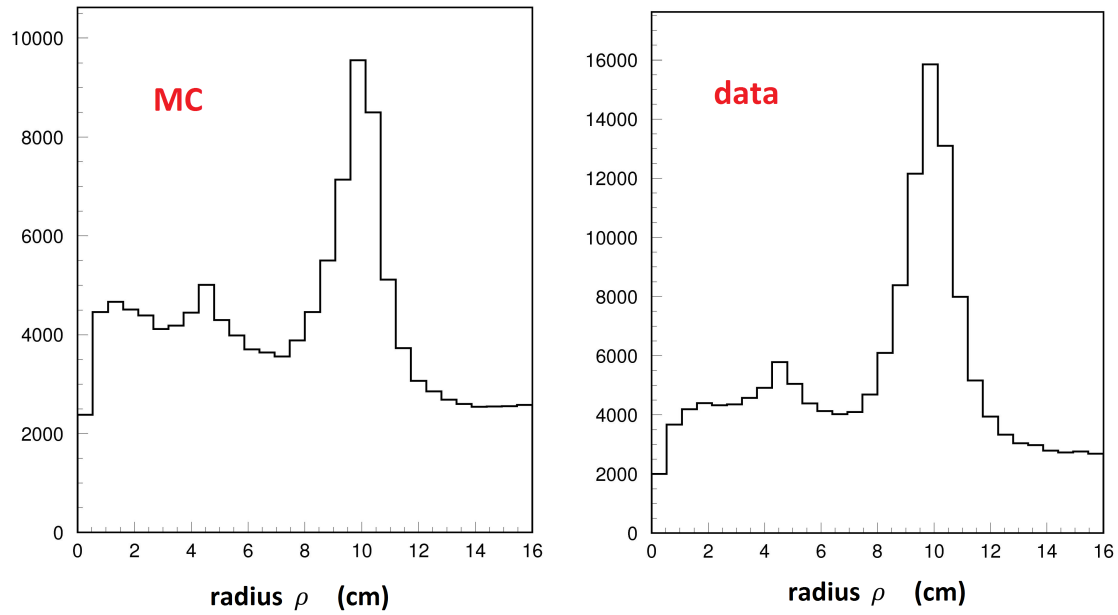

Figure 7.8: Distributions of transverse radius ρ after polar angle cut obtained from data (right) and the MonteCarlo simulations (left).

Finally, one can see in Fig. 7.9 the difference between transverse radius distributions after initial cuts described in chapter 5 and after all the cuts discussed in this chapter. It is visible that application of cuts on K_S (invariant mass, vertex position and momentum nominal value) and K_L (Δp and polar angle) increased the signal to background ratio and improved separation of maxima originating from regeneration in Be and BP.

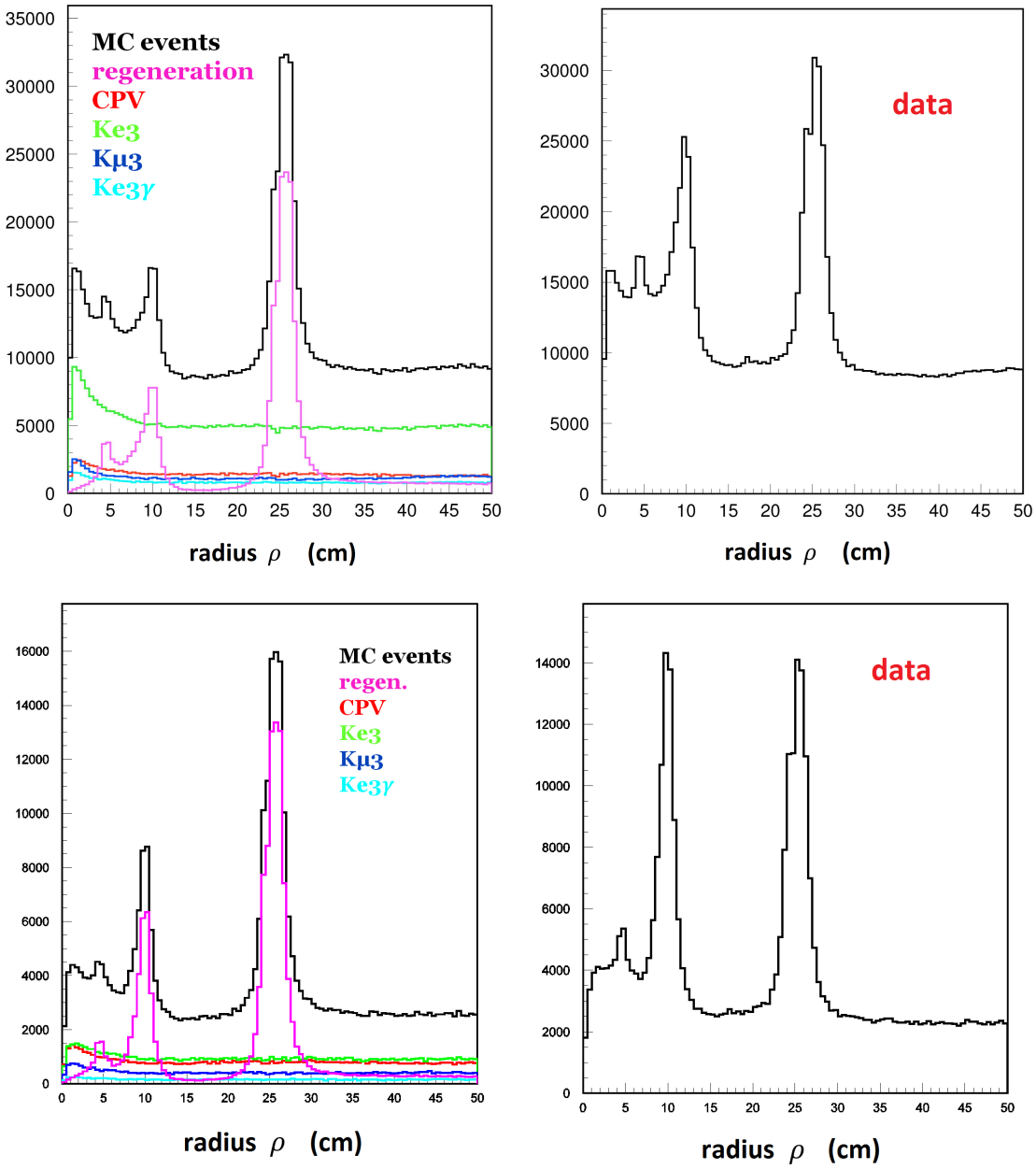

Figure 7.9: Distributions of transverse radius ρ before (1st row) and after (2nd row) regeneration signal selection cuts presented in this chapter. The distributions were obtained from data (2nd column) and the MonteCarlo simulations (1st column).

8. Determination of the regeneration cross-sections

In this chapter, comparison between simulated and experimental distributions of transverse radius ρ is performed in order to extract number of regenerated events in the beam pipe and the drift chamber regions. Finally, cross-sections for regeneration in beryllium (Be), the spherical beam pipe (BP) and the drift chamber inner wall (DC) are calculated. Obtaining these values it is possible to extract regeneration cross-sections for aluminum (Al) and carbon (C), which is also presented in this chapter.

8.1 Choice of fiducial volumes

Because the cylindrical and spherical beam pipe are close to each other, the fit is carried out simultaneously for both of them and separately for the drift chamber. Hence, there are two fiducial volumes (regions of the regenerating surface) which are defined as:

$$Be - BP: \ \rho \in (0; 16)\text{cm}, \quad DC: \ \rho \in (18; 34)\text{cm},$$

where transverse radius ρ is defined in eq. (6.3). One can see in Fig. 8.1 and Fig. 8.2 the data as well as distributions from the MonteCarlo simulations for kaons decay vertices. In each case a clear signals from $K_L \to K_S$ regeneration is seen over a continuous background originating from CPV and semileptonic decays of K_L.

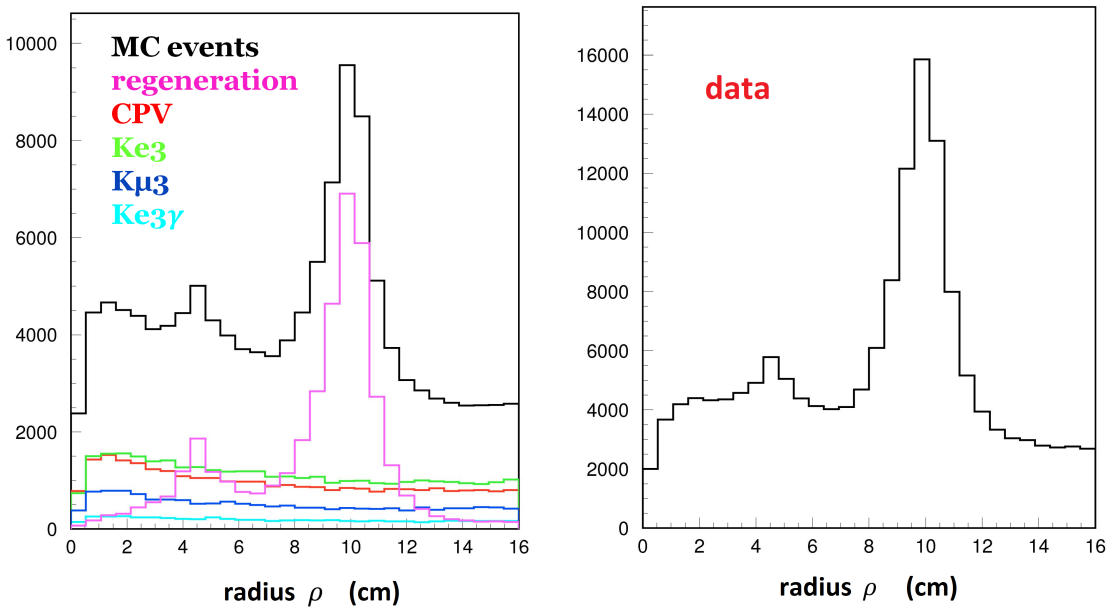

Figure 8.1: Distributions of the transverse radius ρ for the Be-BP region after all applied cuts obtained from data (right) and from the MonteCarlo simulations (left).

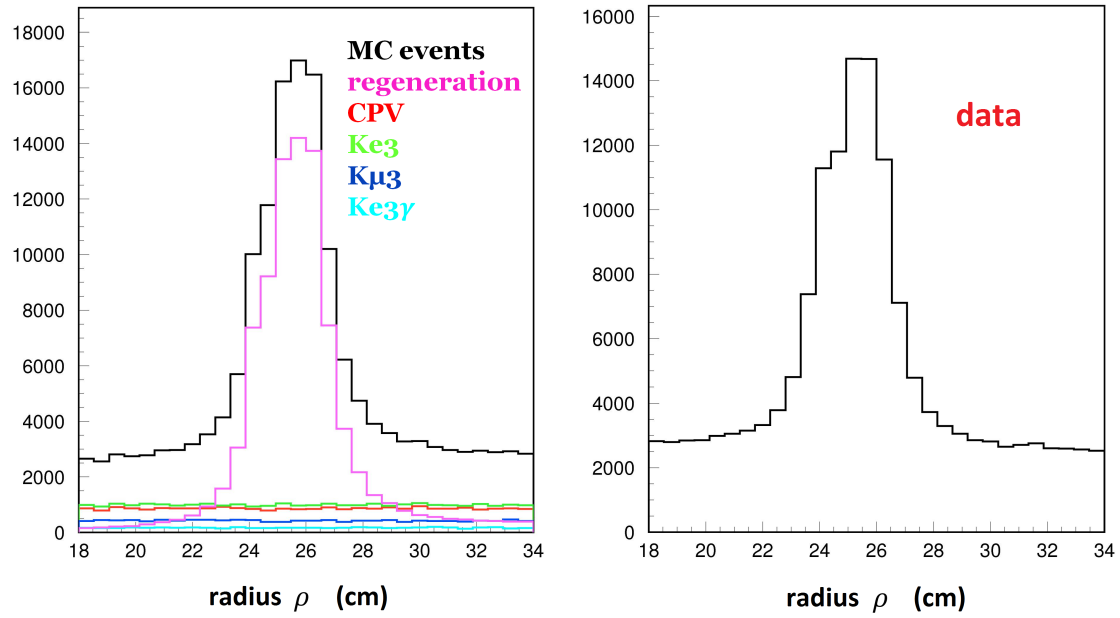

Figure 8.2: Distributions of the transverse radius ρ for the DC region after all applied cuts obtained from data (right) and from the MonteCarlo simulations (left).

8.2 Fit of the MonteCarlo simulations to the data

The MonteCarlo histograms are fit to the data performing maximization of likelihood using Poisson statistics that explanation can be found in Appendix D. The shapes of the background and signal are fixed, as obtained from the MonteCarlo simulations, and their amplitudes are taken as free parameters. From the fit normalization factors for background and signal are obtained. From Fig. 8.1 and Fig. 8.2 it is visible that semileptonic and CPV background have similar shapes so one can add them and fit together. The regeneration from the MonteCarlo simulations in Be, BP and DC is split and fit separately. Hence, for the Be-BP region one has three scale factors and two in the DC region:

- Be-BP (0-16 cm): 3 scale factors - regeneration in Be, regeneration in BP, background (semileptonic and CPV)
- DC (18-34 cm): 2 scale factors - regeneration in DC and background (semileptonic and CPV)

In Fig. 8.3 and Fig. 8.4 the results of the fits are presented. The width of a bin (0.6 cm), corresponds to $1\tau_S$ and is equal to the experimental resolution of the KLOE detector. The obtained number of regenerated events are:

- N_{reg}^{fit}(Be): 5487 events
- N_{reg}^{fit}(BP): 64662 events
- N_{reg}^{fit}(DC): 70357 events

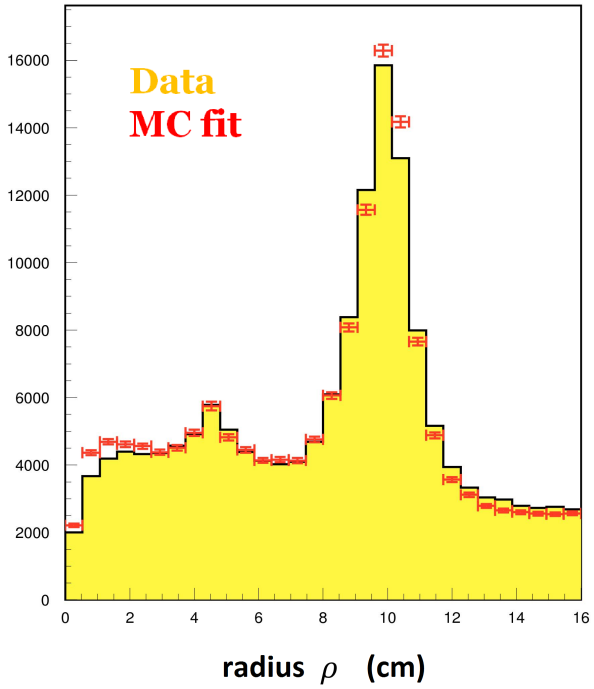

Figure 8.3: Result of the fit in the Be-BP region.

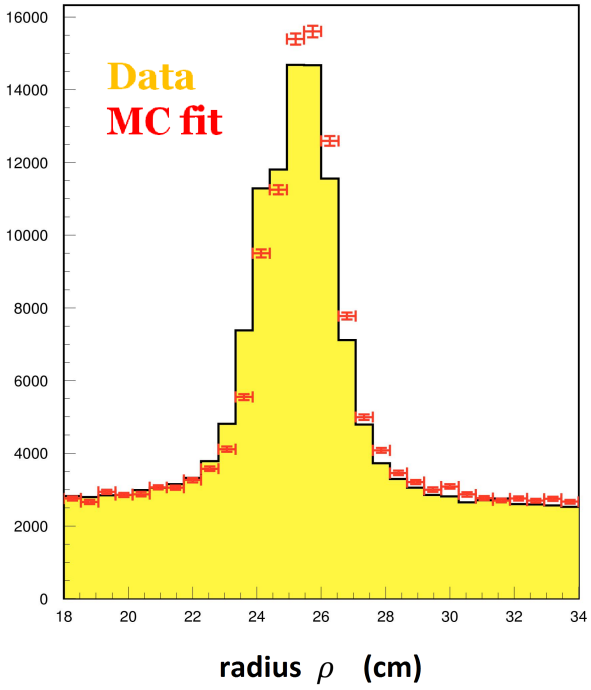

Figure 8.4: Result of the fit in the DC region.

8.3 Results for the KLOE regenerators

The cross-section for regeneration depends on the probability of regeneration P_{reg}, density of scattering centers n_t and the thickness of the regenerating surface Δx_t:

$$\sigma_{reg} = \frac{P_{reg}}{n_t \cdot \Delta x_t}, \tag{8.1}$$

where:

$$n_t = N_A \frac{\rho_t}{A_t} \tag{8.2}$$

and N_A is Avogadro number, ρ_t denotes target density and A_t its molar mass.

Probability of the regeneration reads:

$$P_{reg} = \frac{N_{reg}}{N_{K_L}}, \tag{8.3}$$

where N_{reg} is the number of regenerated events obtained from the fit N_{reg}^{fit} and corrected for total efficiency ε_{tot}:

$$N_{reg} = \frac{N_{reg}^{fit}}{\varepsilon_{tot}}, \tag{8.4}$$

while N_{K_L} denotes the number of tagged K_L that reach regenerator and that can be approximately calculated from:

$$N_{K_L} = N_{K_L}^{tag} \mathrm{e}^{-\langle l \rangle / \lambda_L} - N_{reg}, \tag{8.5}$$

where λ_L is the mean decay length of K_L, $N_{K_L}^{tag}$ number of tagged K_L and $\langle l \rangle = \rho \cdot \left\langle \frac{1}{\sin\theta} \right\rangle$ is average path length of K_L meson between its production point and regenerating surface.

For determination of the all above contributions to the cross-section formula, the reader is referred to Appendix E where appropriate calculations were made. The obtained values are:

- **Number of tagged K_L:** $N_{K_L}^{tag}$=344 551 947
- **Number of regenerated events obtained from the fit:**

$$\begin{aligned} DC &: N_{reg_{DC}}^{fit} = 70357 \pm 265 \\ BP &: N_{reg_{BP}}^{fit} = 64662 \pm 254 \\ Be &: N_{reg_{Be}}^{fit} = 5487 \pm 74 \end{aligned}$$

- **Average density of scattering centers:**

$$\begin{aligned} DC &: \langle n_t \cdot \Delta x_t \rangle_{DC} = 6.960 \cdot 10^{21} \mathrm{cm}^{-2} \\ BP &: \langle n_t \cdot \Delta x_t \rangle_{BP} = 4.982 \cdot 10^{21} \mathrm{cm}^{-2} \\ Be &: \langle n_t \cdot \Delta x_t \rangle_{Be} = 0.6459 \cdot 10^{21} \mathrm{cm}^{-2} \end{aligned}$$

- **Average length of covered by the K_L meson until the regenerating surface:**

$$\begin{aligned} DC &: \mathrm{e}^{-\langle l\rangle_{DC}/\lambda_L} = 0.9256 \\ BP &: \mathrm{e}^{-\langle l\rangle_{BP}/\lambda_L} = 0.9708 \\ Be &: \mathrm{e}^{-\langle l\rangle_{Be}/\lambda_L} = 0.9865 \end{aligned}$$

- **The total efficiency $\varepsilon_{tot} = \varepsilon_{rec} \cdot \varepsilon_{sel} \cdot \varepsilon_{tag}^{bias}$:**

$$\begin{aligned} \varepsilon_{tag}^{bias} &= 0.987 \\ Be - BP &: \varepsilon_{rec} \cdot \varepsilon_{sel} = 0.4250 \\ DC &: \varepsilon_{rec} \cdot \varepsilon_{sel} = 0.5069 \end{aligned}$$

Having all the above values one has to substitute them into the formula for cross-section (8.1) and the results, taking into account statistical error (Appendix E), are equal to:

$$\begin{aligned} \sigma_{reg}^{Be} &= \frac{P_{reg}^{Be}}{\langle n_t \cdot \Delta x_t\rangle_{Be}} = (49.96 \pm 0.67^{stat})\text{mbarn} \\ \sigma_{reg}^{BP} &= \frac{P_{reg}^{BP}}{\langle n_t \cdot \Delta x_t\rangle_{BP}} = (77.60 \pm 0.31^{stat})\text{mbarn} \\ \sigma_{reg}^{DC} &= \frac{P_{reg}^{DC}}{\langle n_t \cdot \Delta x_t\rangle_{DC}} = (75.70 \pm 0.29^{stat})\text{mbarn} \end{aligned}$$

8.4 Systematic uncertainties

The following sources of the systematic uncertainties in the determination of the regeneration cross-sections were taken into account:

- uncertainty of regenerator thickness: $\sim 10\%$
- error on the selection and reconstruction efficiencies: $\sim 1\%$
- shapes of the simulated distributions: $\sim 2\%$
- nuclear interactions contamination: negligible

The thickness of the regenerating surfaces are known with 10% accuracy, determined by their manufacturer:

- Be: $\Delta x_t = (50 \pm 5)\mu$m,
- BP: $\Delta x_t = (500 \pm 50)\mu$m,
- DC: $\Delta x_t = (750 \pm 75)\mu$m for carbon and $\Delta x_t = (150 \pm 15)\mu$m for aluminium.

The errors on the selection and reconstruction efficiencies were taken as $\sim 1\%$ [21] and the uncertainty in the shape of the simulated distributions was estimated to about $\sim 2\%$.

Finally, nuclear interactions contamination was in detailed studied based on the MonteCarlo simulations and their fraction was estimated to $\sim$ 0.5% (Sec. 5.3). Thus the uncertainty originating from the estimation of this background source can be neglected.

Addition of the above discussed systematic errors in quadrature results in a total systematic error of about 10%. This leads to the following final result:

$$\begin{aligned} \sigma_{reg}^{Be} &= (50.0 \pm 0.7^{stat} \pm 5.0^{syst})\text{mbarn} \\ \sigma_{reg}^{BP} &= (77.6 \pm 0.3^{stat} \pm 7.8^{syst})\text{mbarn} \\ \sigma_{reg}^{DC} &= (75.7 \pm 0.3^{stat} \pm 7.6^{syst})\text{mbarn} \end{aligned}$$

8.5 Results for aluminium and carbon

Using the values obtained in the previous section one can extract the cross-sections for the regeneration in aluminium and carbon, solving a set of equations:

$$\sigma_t \sum w_{Nt} = \sum \sigma_N w_{Nt}$$

where weights w_{Nt} are denoted as:

$$w_{Nt} = \frac{\rho_{Nt} \cdot \Delta x_t}{A_N}$$

and t =BP, DC are regenerators, $N = Be,\ C,\ Al$ the regenerating materials, A_N is the molar mass of an element N, ρ_{Nt} denotes density of an element N in the regenerator t and Δx_t is the thickness of the layer made of element t. Applying the above formula one obtains that:

$$\sigma_{Al} = \frac{\sigma_{\text{BP}} \cdot (w_{\text{BP},Be} + w_{\text{BP},Al}) - \sigma_{Be} \cdot w_{\text{BP},Be}}{w_{\text{BP},Al}}, \tag{8.6}$$

$$\sigma_C = \frac{\sigma_{\text{DC}} \cdot (w_{\text{DC},C} + w_{\text{DC},Al}) - \sigma_{Al} \cdot w_{\text{DC},Al}}{w_{\text{DC},C}}. \tag{8.7}$$

The appropriate weights w_{Nt} are equal to:

$$\begin{aligned} w_{\text{BP},Be} &= \frac{1.85 \cdot 62\%}{9} \cdot 0.05 = 0.006372, \\ w_{\text{BP},Al} &= \frac{2.7 \cdot 38\%}{27} \cdot 0.05 = 0.0019, \\ w_{\text{DC},Al} &= \frac{2.7}{27} \cdot 0.015 = 0.0015, \\ w_{\text{DC},C} &= \left(\frac{1.25 \cdot 40\%}{12} + \frac{1.72 \cdot 60\%}{12} \right) \cdot 0.075 = 0.009575. \end{aligned}$$

Substituting all appropriate values into formula (8.6) and (8.7) one obtains:

$$\begin{aligned} \sigma_{reg}^{Al} &= (170 \pm 3^{stat} \pm 38^{syst})\text{mbarn}, \\ \sigma_{reg}^{C} &= (61 \pm 1^{stat} \pm 11^{syst})\text{mbarn}, \end{aligned}$$

where statistical and systematic errors were calculated as:

$$\delta\sigma_{Al} = \sqrt{\left(\delta\sigma_{\text{BP}} \cdot \frac{w_{\text{BP},Be} + w_{\text{BP},Al}}{w_{\text{BP},Al}} \right)^2 + \left(\delta\sigma_{Be} \cdot \frac{w_{\text{BP},Be}}{w_{\text{BP},Al}} \right)^2}$$

and similarly for $\delta\sigma_C$.

9. Conclusions

This thesis aimed at determination of the neutral kaon regeneration cross-section in beryllium for momentum of $p_K \approx 110$ MeV/c, what is crucial for the realization of the KLOE-2 physics program regarding quantum interferometry. This goal was obtained by analyzing data from regeneration of the K_S mesons from the K_L mesons in the cylindrical beam pipe (Be) (made of beryllium) of the KLOE detector. Also the regeneration cross-sections for the KLOE drift chamber inner wall (DC) made of carbon and aluminium and the spherical beam pipe (BP) made of alloy of beryllium and aluminium were evaluated. In addition to the primary aim also the corresponding cross-sections for aluminium and carbon were extracted from the previous ones.

The K_L mesons were produced in the center of the KLOE detector in the collision region of e^+ and e^- beams of the DAΦNE collider that worked at the ϕ resonance peak ($\sqrt{s} \approx 1020$ MeV/c). The data sample comprising of $\sim 3.4 \cdot 10^8$ reconstructed neutral kaon pairs was used in this analysis. The K_L mesons were identified based on primary identification of the K_S meson decays into $\pi^+\pi^-$ close to the interaction point. Next, the number of regenerated events $\phi \to K_S K_L \to \pi^+\pi^- K_S^{reg} \to \pi^+\pi^-\pi^+\pi^-$ was extracted by fitting to the data the simulated distributions of the vertex position of the K_L meson decays into $\pi^+\pi^-$. In this distributions events corresponding to $K_L \to K_S$ regeneration manifest themselves as peaks at the positions of regenerators. The fit of the simulated distributions of signal and background to the data was performed and finally the regeneration cross-sections were determined based on the extracted number of regenerated events and number of the K_L mesons passing through the regenerator.

Obtained in this analysis results for all regenerators are as follows:

$$\begin{aligned}
\sigma_{reg}^{Be} &= (50.0 \pm 0.7^{stat} \pm 5.0^{syst})\text{mbarn}, \\
\sigma_{reg}^{BP} &= (77.6 \pm 0.3^{stat} \pm 7.8^{syst})\text{mbarn}, \\
\sigma_{reg}^{DC} &= (75.7 \pm 0.3^{stat} \pm 7.6^{syst})\text{mbarn}, \\
\sigma_{reg}^{Al} &= (170 \pm 3^{stat} \pm 38^{syst})\text{mbarn}, \\
\sigma_{reg}^{C} &= (61 \pm 1^{stat} \pm 11^{syst})\text{mbarn}.
\end{aligned}$$

These values can be compared with existing experimental results and theoretical evaluations for kaon momentum of about ~ 110 MeV/c, listed in Tab. 9.1.

In order to plot derived cross-sections as a function of the atomic weight for BP and DC one can determine an average atomic weight defined as:

$$\langle A_t \rangle = \frac{\sum A_N \cdot w_{Nt}}{\sum w_{Nt}}.$$

For beryllium, carbon and aluminium one has that: $A_{Be} = 9$, $A_C = 12$, $A_{Al} = 27$, whereas for BP and DC, after substituting appropriate values for ρ_t, A_N and Δx_t, one obtains:

value	material	reference
(55.1 ± 7.7)mbarn	Be	CMD-2 (1999) [39]
(40.7 ± 7.9)mbarn	Be	theory (1996) [38]
(44.2 ± 8.6)mbarn	C	theory (1996) [38]
(18.6 ± 3.6)mbarn	Al	theory (1996) [38]
$(59.6 \pm 0.6^{stat} \pm 6.0^{syst})$mbarn	BP	KLOE (2006) [21]
$(60.2 \pm 0.8^{stat} \pm 6.0^{syst})$mbarn	DC	KLOE (2006) [21]

Table 9.1: Available data and theoretical evaluations for the K_S incoherent regeneration cross–sections at kaon momentum ∼110MeV/c.

$\langle A_{BP} \rangle = 13.13$ and $\langle A_{DC} \rangle = 14.03$. All the results are presented in Fig. 9.1, where the linear fit was performed to the results from this analysis for Be, C, BP, DC and Al. The assumed linear dependence is based on the fact that for cross-sections corresponding to higher particles' momenta this kind of behavior is observed, as it is shown in [38].

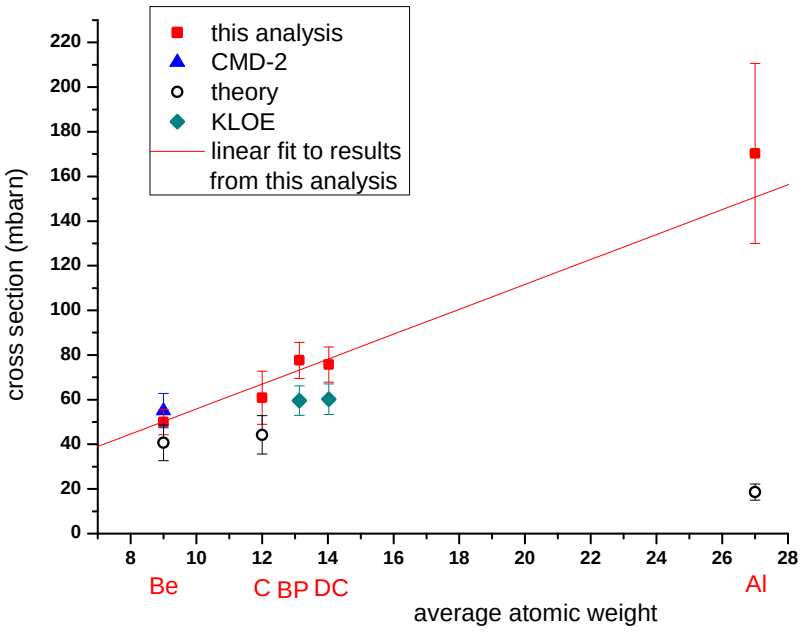

Figure 9.1: Experimental and theoretical regeneration cross-sections situation for kaon momentum ∼110MeV/c. The linear fit to the results obtained from this analysis was also performed.

The result of this thesis for beryllium: $\sigma_{reg}^{Be} = (50.0 \pm 0.7^{stat} \pm 5.0^{syst})$mbarn is between the one evaluated theoretically: (40.7 ± 7.9)mbarn and the only existing measurement: (55.1 ± 7.7)mbarn from the CMD-2 detector. It is worth to stress that both experimental results agree with each other within uncertainties.

One can see that for BP and DC the values extracted in this analysis from KLOE 2004-2005 data: $\sigma_{reg}^{BP} = (77.6 \pm 0.3^{stat} \pm 7.8^{syst})$mbarn and $\sigma_{reg}^{DC} = (75.7 \pm 0.3^{stat} \pm 7.6^{syst})$mbarn

are comparatively large with the one obtained in 2006 from KLOE 2001-2002 data: $\sigma_{reg}^{BP} = (59.6 \pm 0.6^{stat} \pm 6.0^{syst})$mbarn and $\sigma_{reg}^{DC} = (60.2 \pm 0.8^{stat} \pm 6.0^{syst})$mbarn. This difference may be due to the fact that in the previous analysis, because of the lower luminosity, it was impossible to disentangle between signals from the cylindrical and spherical beam pipes and the polar angle cut (Sec. 7.2) was not performed. Also the fit shapes were assumed to be Gaussian whereas in this analysis they were taken as determined using the MonteCarlo simulations.

The extracted result for carbon obtained in this analysis: $\sigma_{reg}^{C} = (61 \pm 1^{stat} \pm 11^{syst})$mbarn agrees within uncertainties with theoretical value: (44.2 ± 8.6)mbarn. However, there is large discrepancy between the regeneration cross-section determined for aluminium: $\sigma_{reg}^{Al} = (170 \pm 3^{stat} \pm 38^{syst})$mbarn and that from the theoretical prediction: (18.6 ± 3.6)mbarn. There are several reasons for this. On the one hand, using only theoretical cross-sections for beryllium (40.7 mbarn) and aluminium (18.6 mbarn) one gets an unreasonable low cross-section for BP that is equal to 35.6 mbarn and calculated from:

$$\sigma_{BP} = \frac{\sigma_{Al} \cdot w_{\mathrm{BP},Al} + \sigma_{Be} \cdot w_{\mathrm{BP},Be}}{w_{\mathrm{BP},Al} + w_{\mathrm{BP},Be}},$$

where the values for weights w can be found in Sec. 8.5. On the other hand, the result for Al is very sensitive to variations of measured cross-sections for Be and BP, from which it was extracted. For comparison, the plot (Fig. 9.2) was made, where in the vertical axis

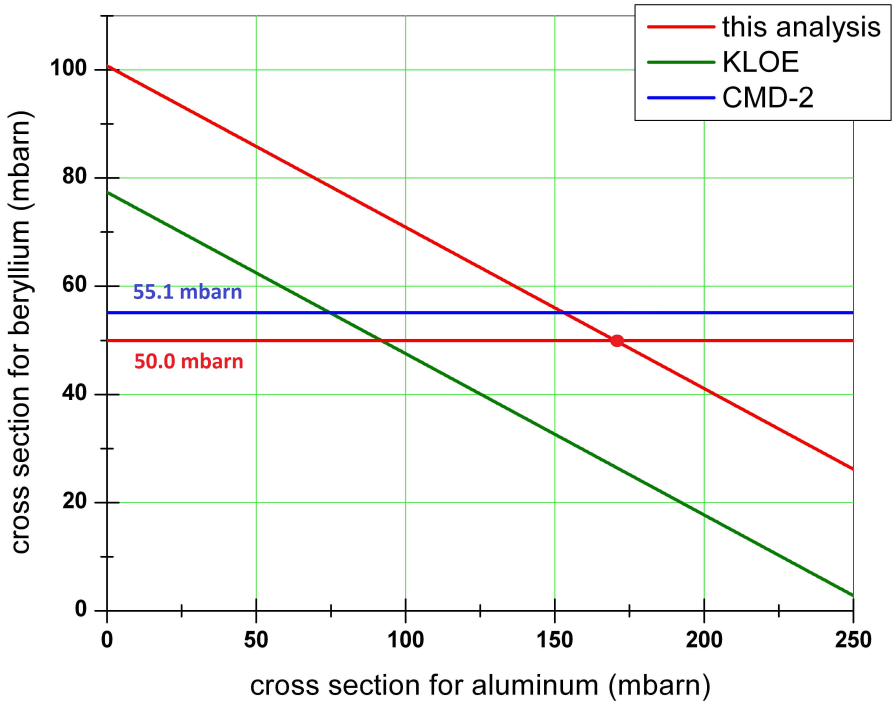

Figure 9.2: Cross-section for beryllium versus cross-section for aluminum. The red lines are based on the results from this analysis where the horizontal one is for Be and the slope corresponds to BP. The blue line is CMD-2 result for Be and the green one corresponds to the old KLOE result for BP.

the cross-section for beryllium is presented and in the horizontal axis the cross-section for aluminum. The red lines are the results from this analysis where the horizontal one is for Be measurement and the slope is described based on the BP regeneration cross-section:

$$\sigma_{Be} = \frac{\sigma_{\mathrm{BP}} \cdot (w_{\mathrm{BP},Be} + w_{\mathrm{BP},Al}) - \sigma_{Al} \cdot w_{\mathrm{BP},Al}}{w_{\mathrm{BP},Be}},$$

The green line corresponds to the old KLOE result for BP and the blue one is CMD-2 result for Be. It can be seen that it is almost impossible to accommodate the theoretical prediction of $\sim$ 20 mbarn for Al cross-section with the experimental data, while the data themselves suggest much higher value (approximately in the range 100-200 mbarn).

In the original note of [38], authors explained that the theoretical prediction of regeneration cross-section for aluminum, in the kaon momentum range of 100-200 MeV/c, is expected to change abruptly. They advised the reader about possibility that their predictions could be not correct and should be taken with care. Thus, the result presented here, being in the case of C and Al the first measurement of regeneration cross-sections at P = 110 MeV/c, do not seem to confirm this theoretical prediction. The linear fit presented in Fig. 9.1 is intended only to guide the eye of the reader and might represent a reasonable approximation of the behavior of the regeneration cross-section as a function of the atomic weight in the shown range.

A. The optical theorem

In quantum physics, the scattering amplitude is the amplitude of the outgoing spherical wave relative to the incoming plane wave in the scattering process. A large distance away from the scatterer it is given approximately by the wave function [35]:

$$\psi(r) \approx e^{ikz} + f(\vartheta)\frac{e^{ikr}}{r}, \tag{A.1}$$

where r is the coordinate vector, e^{ikz} is the incoming plane wave with the wave vector k along the z axis, $\frac{e^{ikr}}{r}$ is the outgoing spherical wave, ϑ is the scattering angle and $f(\vartheta)$ is the scattering amplitude. All higher terms are negligible since they vanish more quickly than $\frac{1}{r^2}$. For large values of z the binomial theorem $\left((x+y)^n = \sum_{k=0}^{n} \binom{n}{k} x^{n-k}y^k\right)$ gives:

$$r = \sqrt{x^2+y^2+z^2} \approx z + \frac{x^2+y^2}{2z} \tag{A.2}$$

The intensity is proportional to the square of the amplitude $\psi(r)$ hence implying approximation (A.2) in (A.1), one obtains:

$$\begin{aligned}
|\psi(r)|^2 &= \left|e^{ikz} + \frac{f(\vartheta)}{r}e^{ikz}e^{ik(x^2+y^2)/2z}\right|^2 = \left(e^{ikz} + \frac{f(\vartheta)}{r}e^{ikz}e^{ik(x^2+y^2)/2z}\right)\cdot \\
&\cdot \left(e^{-ikz} + \frac{f^*(\vartheta)}{r}e^{-ikz}e^{-ik(x^2+y^2)/2z}\right) = \\
&= 1 + \frac{f^*(\vartheta)}{r}e^{-ik(x^2+y^2)/2z} + \frac{f(\vartheta)}{r}e^{ik(x^2+y^2)/2z} + \frac{f(\vartheta)f^*(\vartheta)}{r^2} \approx \\
&\approx 1 + \frac{f^*(\vartheta)}{z}e^{-ik(x^2+y^2)/2z} + \frac{f(\vartheta)}{z}e^{ik(x^2+y^2)/2z} + \frac{|f(\vartheta)|^2}{z^2}.
\end{aligned}$$

If we neglect the $\frac{1}{z^2}$ term and use the fact that $A + A^* = 2\ \Re e A$ we have:

$$|\psi(r)|^2 \approx 1 + 2\ \Re e\frac{f(\vartheta)}{z}e^{ik(x^2+y^2)/2z}$$

Now one can integrate over a screen in the $x-y$ plane for small angles $f(\vartheta) \approx f(0)$, where $f(0)$ is the amplitude of the wave scattered to the center of a distant screen. One obtains:

$$\int_{-\infty}^{+\infty} |\psi(r)|^2\, da \approx A + 2\ \Re e\frac{f(0)}{z}\int_{-\infty}^{+\infty} e^{ikx^2/2z}dx \int_{-\infty}^{+\infty} e^{iky^2/2z}dy,$$

where A is the integrated area of the surface. The exponential parts can be treated as Gaussians so:

$$\int_{-\infty}^{+\infty} |\psi(r)|^2\, da \approx A + 2\ \Re e\frac{f(0)}{z}\left(\sqrt{\frac{z}{ik}}\cdot\sqrt{2\pi}\right)^2 = A - \Im m f(0)\frac{4\pi}{k}.$$

This is the difference of the amount of energy that would reach the screen without scattering A, lessened by an amount $\Im m f(0)\frac{4\pi}{k}$. This amount is the total energy scattered because of

conservation of energy, thus it is the total effective scattering cross-section of the scatterer. The optical theorem is usually written in the form:

$$\sigma_T = \Im m f(0) \frac{4\pi}{k}. \tag{A.3}$$

B. Recoil momentum and energy of the nucleus in the kaon scattering

To calculate the recoil momentum of the nucleus Δp and regenerated K_S momentum p_S values one can consider the four-momentum vector conservation of kaons and the scattering centers:

$$P_L + S = P_S + S', \tag{B.1}$$

where four-momentum vectors for K_L and K_S are denoted by P_L and P_S, respectively, and for the scattering center it is S before and S' after the collision. At the beginning, the scattering center was at rest so $S = (M, 0)$ and K_L four-momentum was: $P_L = (E_L, \vec{p}_L)$. After the collision situation changed to: $P_S = (E_S, \vec{p}_S)$ and $S' = (E', \vec{p}\,') = (M + (E_L - E_S), \vec{p}_L - \vec{p}_S)$. Using these notations one can see that:

$$(P_L - P_S)^2 = (E_L - E_S)^2 - (\vec{p}_L - \vec{p}_S)^2 = (E' - M)^2 - \vec{p}\,'^2. \tag{B.2}$$

Mass of the scattering center is significantly large with respect to the kaon mass, so one has that $S^2 = S'^2$ so $M^2 = E'^2 - \vec{p}\,'^2$ and the formula (B.2) reads:

$$(E_L - E_S)^2 - (\vec{p}_L - \vec{p}_S)^2 \approx 2M(M - E') = 2M(E_S - E_L). \tag{B.3}$$

Hence:

$$(E_L - E_S)^2 - (\vec{p}_L - \vec{p}_S)^2 + 2M(E_L - E_S) = 0, \tag{B.4}$$

where $E_L - E_S$ is the recoil energy of the target and $\vec{p}_L - \vec{p}_S$ is the recoil momentum. Since M is much bigger than E_L and E_S ($M \gg E_{L,S}$) so:

$$2M(E_L - E_S) = 0, \tag{B.5}$$

and then $E_S \approx E_L$:

$$\begin{aligned} p_L^2 + m_L^2 &= p_S^2 + m_S^2 \\ (p_L - p_S)(p_L + p_S) &= -(m_L - m_S)(m_L + m_S) \\ p_L - p_S &= -\Delta m \frac{m_L + m_S}{p_L + p_S}. \end{aligned} \tag{B.6}$$

Finally, taking into account that $m_L \approx m_S$ and $p_L + p_S \approx 2 \cdot p_L$, the equation (B.6) reads:

$$\Delta p = \Delta m \frac{m_L}{p_L}. \tag{B.7}$$

Since $\Delta m \approx 3.5 \cdot 10^{-6}$ eV and the KLOE momentum for K_L is equal to $p_L \approx 110$ MeV/c, the recoil momentum of nucleus is of the order:

$$\Delta p \approx 15.8 \cdot 10^{-6} \text{ eV/c}. \tag{B.8}$$

Taking into account that $\Delta E \ll M$ one can derive from equation (B.4) that the recoil energy $\Delta E = E_L - E_S$ is approximately equal to:

$$\Delta E \approx \frac{(\Delta p)^2}{2M}. \tag{B.9}$$

For heavy nucleus ($A \approx 100$), $M \approx 100$ GeV and for $p_L = 0.1$ GeV/c one obtains:

$$\Delta E \approx 10^{-22} \text{ eV/c}^2. \tag{B.10}$$

C. K_L impact point on the regenerator

In order to obtain coordinates of the K_L meson impact point on the regenerator (that at KLOE can be cylinder or sphere) one has to calculate coordinates of point of intersection of line with sphere and cylinder.

In three dimensions, a line is the set of points (x, y, z) which may be described by the following parametric equations in which $A = (x_A, y_A, z_A)$ is any point on the line and the directional vector $\vec{u} = [u_1, u_2, u_3]$ is parallel to the line:

$$\begin{cases} x = x_A + t \cdot u_1 \\ y = y_A + t \cdot u_2 \quad \text{where } t \in \Re e \ . \\ z = z_A + t \cdot u_3 \end{cases} \tag{C.1}$$

A sphere with center (x_0, y_0, z_0) and radius r is the set of points (x, y, z) such that:

$$(x - x_0)^2 + (y - y_0)^2 + (z - z_0)^2 = r^2, \tag{C.2}$$

whereas an equation for a cylinder with radius ρ and hight h reads:

$$\begin{cases} x^2 + y^2 = \rho^2 \\ -h \leq z \leq h \end{cases} . \tag{C.3}$$

Both pairs of equations (C.1), (C.2) and (C.1), (C.3) are system of four equations with four unknowns (x, y, z, t). Solving this for sphere one obtains two points of intersection:

$$\begin{aligned} t_{1,2} &= \frac{-1}{u_1^2 + u_2^2 + u_3^2}\Big(u_1 \cdot x_A + u_2 \cdot y_A + u_3 \cdot z_A \pm \\ &\pm \sqrt{(u_1 \cdot x_A + u_2 \cdot y_A + u_3 \cdot z_A)^2 - (u_1^2 + u_2^2 + u_3^2) \cdot (x_A^2 + y_A^2 + z_A^2 - r^2)}\Big). \end{aligned}$$

These two results are presented schematically in Fig. C.1, where the directional vector is also shown.

One can see that only one result, t_2, is in the proper direction:

$$\begin{aligned} t_2 &= \frac{-1}{u_1^2 + u_2^2 + u_3^2}\Big(u_1 \cdot x_A + u_2 \cdot y_A + u_3 \cdot z_A + \\ &- \sqrt{(u_1 \cdot x_A + u_2 \cdot y_A + u_3 \cdot z_A)^2 - (u_1^2 + u_2^2 + u_3^2) \cdot (x_A^2 + y_A^2 + z_A^2 - r^2)}\Big). \end{aligned}$$

Hence the correct coordinates of the intersection point with a sphere are:

$$\begin{cases} x = x_A + t_2 \cdot u_1 \\ y = y_A + t_2 \cdot u_2 \\ z = z_A + t_2 \cdot u_3 \end{cases} .$$

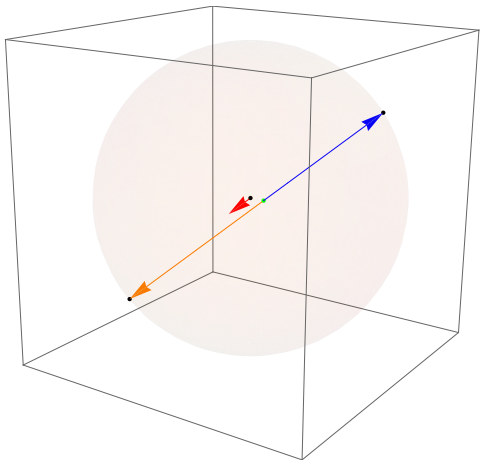

Figure C.1: Two points of intersection of line with sphere shown as vectors (orange and blue ones). The unitary direction vector (red) is also presented.

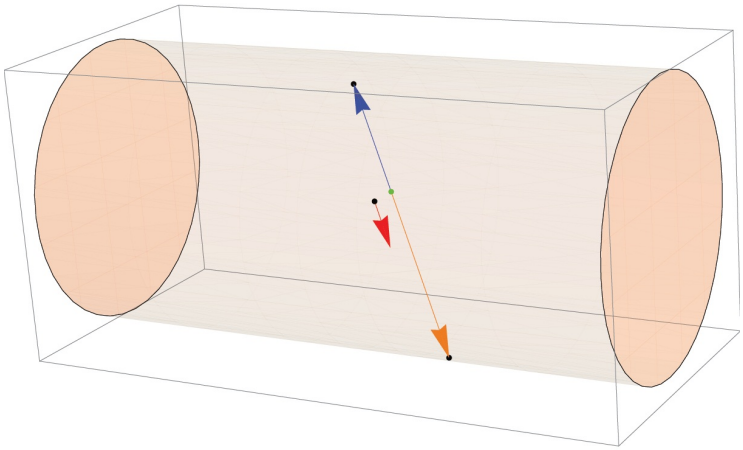

Figure C.2: Two points of intersection of line with cylinder shown as vectors (orange and blue ones). The unitary direction vector (red) is also presented.

If now one solves the system of equations (C.1) and (C.3) for a cylinder, one gets:

$$t_{3,4} = \frac{-u_1 \cdot x_A - u_2 \cdot y_A \mp \sqrt{\rho^2 \left(u_1^2 + u_2^2\right) - (u_2 \cdot x_A - u_1 \cdot y_A)^2}}{u_1^2 + u_2^2}.$$

These two results are presented schematically in Fig. C.2.

Here also only one result, t_4, is in the proper direction:

$$t_4 = \frac{-u_1 \cdot x_A - u_2 \cdot y_A + \sqrt{\rho^2 \left(u_1^2 + u_2^2\right) - (u_2 \cdot x_A - u_1 \cdot y_A)^2}}{u_1^2 + u_2^2}$$

and the coordinates of the intersection point with a cylinder are:

$$\begin{cases} x = x_A + t_4 \cdot u_1 \\ y = y_A + t_4 \cdot u_2 \\ z = z_A + t_4 \cdot u_3 \end{cases}.$$

In order to calculate the K_L impact point on the regenerator, one has to use the K_L *tag* as an directional vector:

$$\vec{u} \equiv \frac{\vec{p}_{K_L}^{\,tag}}{\left|\vec{p}_{K_L}^{\,tag}\right|}$$

and as point A, the ϕ decay point:

$$A \equiv \vec{x}_{\phi}.$$

One also has to substitute values for r and ρ, appropriate for the KLOE regenerators, and coordinates of a center of the sphere equal to $(x_0, y_0, z_0) = (0, 0, 0)$.

D. Fitting with finite MonteCarlo statistics

Most of the following text is based on paper [43] so more interested readers are referred to this article.

Analysis of results from particle physics experiments often involves estimation of the composition of a data sample, based on the MonteCarlo simulations of the various sources. To do so, one can fit to the data simulated MonteCarlo shapes of these sources by requiring that they "fit the best". However, the χ^2 minimization technique is inappropriate because data values are binned in such a way that the number of data points in many bins are small. Hence, a maximum likelihood using Poisson statistics is often used, taking into account that MonteCarlo statistics used are finite.

The common problem is a determination the proportions P_j of the different sources in the data. There is no analytic form available for the distributions of these sources, only samples of "data" generated by the MonteCarlo simulation. Therefore, one has to bin the data, dividing them into n bins, where in every bin the number of events in the real data is d_i. The number f_i of events in ith bin, originating from m sources, read:

$$f_i = N_D \sum_{j=1}^{m} P_j a_{ji}/N_j \tag{D.1}$$

where a_{ji} is the number of MonteCarlo events from source j in bin i. N_D is the total number of events in the data sample and N_j the total number in the MonteCarlo sample for source j, both defined as:

$$N_D = \sum_{i=1}^{n} d_i, \quad N_j = \sum_{i=1}^{n} a_{ji}. \tag{D.2}$$

The P_j are then the actual proportions and should sum to unity. Writing $p_j = N_D P_j/N_j$, one obtains:

$$f_i = \sum_{j=1}^{m} p_j a_{ji}. \tag{D.3}$$

One approach is to estimate p_j by adjusting them to minimize:

$$\chi^2 = \sum_i \frac{(d_i - f_i)^2}{d_i} \tag{D.4}$$

but this assumes that the distribution for d_i is Gaussian and it is only good approximation at large numbers. If many d_i are small, one has to consider Poisson distribution and then the probability for observing a particular d_i reads:

$$e^{-f_i} \frac{f_i^{d_i}}{d_i!}. \tag{D.5}$$

Thus, the estimates of the proportions p_j are found by maximizing the total likelihood ($\mathcal{L} = \prod_{i=1}^{n} e^{-f_i} \frac{f_i^{d_i}}{d_i!}$) or its logarithm (the term $\ln d_i!$ is skipped because it does not depend on f_i):

$$\ln \mathcal{L} = \sum_{i=1}^{n} d_i \ln f_i - f_i. \tag{D.6}$$

However, this does not account for the fact that the MonteCarlo samples used may also be finite size, leading to statistical fluctuations in the a_{ji}.

The correct way to view this problem is as follows. For each source, in each bin, there is some expected number of events A_{ji} and then:

$$f_i = \sum_{j=i}^{m} p_j A_{ji}. \tag{D.7}$$

Hence, the total likelihood which is to be maximized is the combined probability of the observed d_i and a_{ji}:

$$\ln \mathcal{L} = \sum_{i=1}^{n} d_i \ln f_i - f_i + \sum_{i=1}^{n} \sum_{j=1}^{m} a_{ji} \ln A_{ji} - A_{ji}. \tag{D.8}$$

To find the maximum one has to differentiate equation (D.8) and set the derivatives to zero. One obtains two sets of equations:

$$\sum_{i=1}^{n} \frac{d_i A_{ji}}{f_i} - A_{ji} = 0 \quad \forall j \tag{D.9}$$

$$\frac{d_i p_j}{f_i} - p_j + \frac{a_{ji}}{A_{ji}} - 1 = 0 \quad \forall i, j \tag{D.10}$$

Equation (D.10) can be rewritten as:

$$1 - \frac{d_i}{f_i} = \frac{1}{p_j}(\frac{a_{ji}}{A_{ji}} - 1) \quad \forall i, j \tag{D.11}$$

while defining:

$$t_i = 1 - \frac{d_i}{f_i} \tag{D.12}$$

it reads:

$$A_{ji} = \frac{a_{ji}}{1 + p_j t_i}. \tag{D.13}$$

Hence, if d_i is not equal to zero then:

$$\frac{d_i}{1 - t_i} = f_i = \sum_j p_j A_{ji} = \sum_j \frac{p_j a_{ji}}{1 + p_j t_i}. \tag{D.14}$$

If these n equations are satisfied with defined A_{ji} then all the $m \times n$ equations (D.10) are satisfied.

For a given set of p_j the algorithm solves equations (D.14) for the t_i (D.12), giving the A_{ji} (D.13).

E. Evaluation of the contributions for the cross-section formula

1. **Average** $\left\langle \frac{1}{\sin\theta} \right\rangle$

   Angular distribution of K_L meson in ϕ rest frame is proportional to $\sin^2\theta^*$, where θ is K_L polar angle, and it reads [21]:

   $$\frac{dN}{d\Omega^*} = \frac{dN}{d\varphi d\cos\theta^*} \propto \sin^2\theta^*, \tag{E.1}$$

   where φ is azimuthal angle of K_L. Hence, the average value of $\frac{1}{\sin\theta}$ for the cylindrical regenerators is calculated taking into account K_L angular distribution as [21]:

   $$\left\langle \frac{1}{\sin\theta} \right\rangle = \frac{\int_{\theta_{min}}^{\pi-\theta_{min}} \frac{1}{\sin\theta} \cdot \sin^2\theta d\cos\theta}{\int_{\theta_{min}}^{\pi-\theta_{min}} \sin^2\theta d\cos\theta} = \frac{\sin\theta_{min}\cos\theta_{min} - \theta_{min} + \pi/2}{2(\cos\theta_{min} - \cos^3\theta_{min}/3)}, \tag{E.2}$$

   where θ_{min} is minimal angle for regeneration to occur, schematically presented for the cylindrical beam pipe regenerator in Fig. E.1. In fact, because of the polar angle cut applied in Sec. 7.2, this angle for all regenerators is equal to:

   $$\theta_{min} = 60 \text{ deg} \approx 1.047 \text{ rad}$$

   Hence, substituting this value into formula (E.2) one obtains:

   $$\left\langle \frac{1}{\sin\theta} \right\rangle = 1.044. \tag{E.3}$$

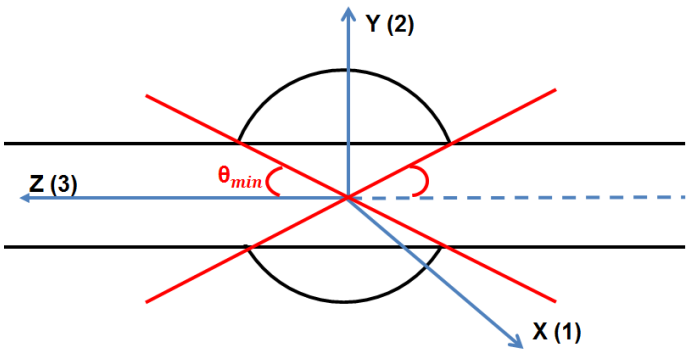

Figure E.1: Schematic presentation of θ_{min} angle for the cylindrical beam pipe.

2. **Average density of scattering centers**

   One can calculate, for all three regenerators, the average value of $\langle n_t \cdot \Delta x_t \rangle = \left\langle \frac{N_A \cdot \rho_t \cdot \Delta x_t}{A_t} \right\rangle$ which is a denominator in the cross-section formula (8.1):

- **DC**

$$\langle n_t \cdot \Delta x_t \rangle_{DC} = \left\langle \tfrac{1}{\sin\theta} \right\rangle \cdot N_A \left[\tfrac{\rho_{Al}}{A_{Al}} \cdot \Delta x_{Al} + \left(\tfrac{\rho_{C_1}}{A_C} \cdot 40\% + \tfrac{\rho_{C_2}}{A_C} \cdot 60\% \right) \cdot \Delta x_C \right] =$$
$$= 1.044 \cdot 6.022 \cdot 10^{23} \left[\tfrac{2.70}{27} \cdot 0.015 + \left(\tfrac{1.25}{12} \cdot 0.4 + \tfrac{1.72}{12} \cdot 0.6 \right) \cdot 0.075 \right] =$$
$$= 6.960 \cdot 10^{21} \mathrm{cm}^{-2}$$

- **BP**

$$\langle n_t \cdot \Delta x_t \rangle_{BP} = N_A \left(\tfrac{\rho_{Al}}{A_{Al}} \cdot 38\% + \tfrac{\rho_{Be}}{A_{Be}} \cdot 62\% \right) \cdot \Delta x_{BP} =$$
$$= 6.022 \cdot 10^{23} \left(\tfrac{2.70}{27} \cdot 0.38 + \tfrac{1.85}{9} \cdot 0.62 \right) \cdot 0.05 =$$
$$= 4.982 \cdot 10^{21} \mathrm{cm}^{-2}$$

- **Be**

$$\langle n_t \cdot \Delta x_t \rangle_{Be} = \left\langle \tfrac{1}{\sin\theta} \right\rangle \cdot N_A \left(\tfrac{\rho_{Be}}{A_{Be}} \cdot \Delta x_{Be} \right) =$$
$$= 1.044 \cdot 6.022 \cdot 10^{23} \left(\tfrac{1.85}{9} \cdot 0.005 \right) =$$
$$= 0.6459 \cdot 10^{21} \mathrm{cm}^{-2}$$

3. **K_L mean decay length**

   K_L mean decay length is calculated as:

$$\lambda_L = \tau_L \cdot \beta_L \cdot c,$$

   where $\tau_L = 51.16$ ns, $c = 29.98$ cm/ns and β_L reads:

$$\beta_L = \frac{|\vec{p}_{K_L}|}{E_{K_L}} = \frac{|\vec{p}_{K_L}|}{\sqrt{m_{K^0}^2 + |\vec{p}_{K_L}|^2}}.$$

   Since $m_{K^0} \approx 498$ MeV, and for KLOE momenta of K_L $|\vec{p}_{K_L}| \approx 110$ MeV/c, one obtains:

$$\begin{aligned} \beta_L &\approx 0.22, \\ \lambda_L &\approx 331 \text{ cm}. \end{aligned}$$

4. **Average path length of the K_L meson until the regenerating surface**

   The average path length of K_L until the regenerating surface $\langle l \rangle$ can be calculated using value of $\left\langle \frac{1}{\sin\theta} \right\rangle$ (point 1) for the regenerators situated at $\rho_{DC} = 25$ cm, $r_{BP} = 10$ cm and $\rho_{Be} = 4.4$ cm and substituting the value of λ_L (point 3):

   - **DC**

$$\langle l \rangle_{DC} = \rho_{DC} \left\langle \frac{1}{\sin\theta} \right\rangle = 25 \text{ cm} \cdot 1.044 = 26.089 \text{ cm} \quad \Rightarrow \quad \mathrm{e}^{-\langle l \rangle_{DC}/\lambda_L} = 0.9243$$

   - **BP**

$$\langle l \rangle_{BP} = 10 \text{ cm} \quad \Rightarrow \quad \mathrm{e}^{-\langle l \rangle_{BP}/\lambda_L} = 0.9703$$

- **Be**

$$\langle l \rangle_{Be} = \rho_{Be} \left\langle \frac{1}{\sin\theta} \right\rangle = 4.4 \text{ cm} \cdot 1.044 = 4.592 \text{ cm} \quad \Rightarrow \quad \mathrm{e}^{-\langle l \rangle_{Be}/\lambda_L} = 0.9862$$

5. **Efficiencies**

The total efficiency for identification of $K_S^{reg} \to \pi^+\pi^-$ decays reads:

$$\varepsilon_{tot} = \varepsilon_{rec} \cdot \varepsilon_{sel} \cdot \varepsilon_{tag}^{bias},$$

where ε_{rec} is reconstruction efficiency, ε_{sel} selection efficiency and ε_{tag}^{bias} is *tag bias* efficiency, explained below.

- **The *tag bias* efficiency** [41]

The tagging procedure (Sec. 5.2) is not perfect, because the tagging efficiency depends slightly on the evolution of K_L. All the events in which K_L interacts in the calorimeter, escapes the detector, or decays into any final state are included. The difference in tagging efficiency in each case depends on the tagging algorithm and the minimization of such differences is used to optimize the tagging criteria. To correct for this effect, one defines the *tag bias* for the detection of K_L decays to a final state k as the ratio of the tagging efficiency for $K_L \to k$ in the fiducial volume to the overall tagging efficiency, determined without regard to the evolution of the K_L. The *tag bias* for channel k is thus:

$$\varepsilon_{tag}^{bias} = \frac{\varepsilon_{tag_k}}{\varepsilon_{tag_{tot}}}$$

and for regenerated events into $\pi^+\pi^-$ is equal to:

$$\varepsilon_{tag}^{bias} = 0.987$$

- **Reconstruction and selection efficiency**

Reconstruction and selection efficiencies $\varepsilon_{rec} \cdot \varepsilon_{sel}$ are obtained from the MonteCarlo simulations for the appropriate fiducial volumes (Sec. 8.1) as a ratio between the number of *reconstructed* regenerated events passing the selection and the number of *generated* regenerated events. The obtained values are equal to:

$$\begin{aligned} \mathbf{Be-BP} \quad &: \quad \varepsilon_{rec} \cdot \varepsilon_{sel} = 0.4250 \\ \mathbf{DC} \quad &: \quad \varepsilon_{rec} \cdot \varepsilon_{sel} = 0.5069 \end{aligned}$$

6. **Regeneration probability**

For the calculation of the regeneration probabilities that read:

$$P_{reg} = \frac{N_{reg}^{fit}}{\varepsilon_{tot} \cdot N_{K_L}^{tag} \cdot \mathrm{e}^{-\langle l \rangle/\lambda_L}}$$

one has to know the number of tagged K_L ($N_{K_L}^{tag}$), the number of regenerated events obtained from the fit (N_{reg}^{fit}) for all three regenerators and substitute values of exponential factor $\mathrm{e}^{-\langle l\rangle/\lambda_L}$ (point 4) and total efficiencies ε_{tot} (point 5). The first two are listed below:

- **Number of tagged** K_L: $N_{K_L}^{tag}$=344 551 947
- **Number of regenerated events obtained from the fit** (Sec. 8.2):

$$\begin{aligned} DC &: N_{reg_{DC}}^{fit} = 70357 \\ BP &: N_{reg_{BP}}^{fit} = 64662 \\ Be &: N_{reg_{Be}}^{fit} = 5487 \end{aligned}$$

Finally, for the appropriate regenerators, one obtains:

- **DC**

$$P_{reg}^{DC} = \frac{N_{reg_{DC}}^{fit}}{\varepsilon_{tot}^{DC}\cdot N_{K_L}^{tag}\cdot \mathrm{e}^{-\langle l\rangle_{DC}/\lambda_L}} = 5.269\cdot 10^{-4}$$

- **BP**

$$P_{reg}^{BP} = \frac{N_{reg_{BP}}^{fit}}{\varepsilon_{tot}^{BP}\cdot N_{K_L}^{tag}\cdot \mathrm{e}^{-\langle l\rangle_{BP}/\lambda_L}} = 3.866\cdot 10^{-4}$$

- **Be**

$$P_{reg}^{Be} = \frac{N_{reg_{Be}}^{fit}}{\varepsilon_{tot}^{Be}\cdot N_{K_L}^{tag}\cdot \mathrm{e}^{-\langle l\rangle_{Be}/\lambda_L}} = 3.227\cdot 10^{-5}$$

7. **Statistical errors**

The statistical error is calculated as:

$$\begin{aligned} \delta\sigma_{reg} &= \frac{1}{\varepsilon_{tot}\cdot\langle n_t\cdot\Delta x_t\rangle}\sqrt{\left(\frac{\delta N_{reg}^{fit}}{N_{K_L}}\right)^2+\left(\frac{N_{reg}^{fit}}{N_{K_L}^2}\delta N_{K_L}\right)^2}\approx \\ &\approx \frac{1}{\varepsilon_{tot}\cdot\langle n_t\cdot\Delta x_t\rangle}\cdot\frac{\delta N_{reg}^{fit}}{N_{K_L}} = \frac{\sqrt{N_{reg}^{fit}}}{N_{K_L}\cdot\varepsilon_{tot}\cdot\langle n_t\cdot\Delta x_t\rangle} \end{aligned}$$

Substituting all appropriate values one obtains:

- **DC**

$$\delta\sigma_{reg}^{DC} = 0.29 \text{ mbarn}$$

- **BP**

$$\delta\sigma_{reg}^{BP} = 0.31 \text{ mbarn}$$

- **Be**

$$\delta\sigma_{reg}^{Be} = 0.67 \text{ mbarn}$$

Bibliography

[1] G. D. Rochester, C. C. Butler, *Evidence for the existence of new unstable elementary particles*, Nature London **160** (1947) 855

[2] M. Gell-Mann, *Isotopic Spin and New Unstable Particles*, Phys. Rev. **92** (1953) 833

[3] T. Nakano, K. Nishijima, *Charge independence for V-particles*, Prog. Theor. Phys. **10** (1953) 581

[4] M. Gell-Mann, A. Pais, *Behavior of neutral particles under charge conjugation*, Phys. Rev. **97** (1955) 1387

[5] Donald H. Perkins, *Introduction to high energy physics*, Cambridge University Press (2000) 226

[6] T. D. Lee, C. N. Yang, *Question of Parity Conservation in Weak Interactions*, Phys. Rev. **104** (1956) 254

[7] L. D. Landau, *On the conservation laws for weak interactions*, Zh. Eksp. Teor. Fiz. **32** (1957) 405

[8] J. H. Christenson, J. W. Cronin, V. L. Fitch and R. Turlay, *Evidence for the* 2π *decay of the* K_2^0 *meson*, Phys. Rev. Lett. **13** (1964) 138

[9] V. Weisskopf, E. P. Wigner, *Calculation of the neutral brightness of spectral lines on the basis of Dirac's theory*, Z. Phys. **63** (1930) 54-73

[10] A. Di Domenico, *Neutral kaon interferometry at a* ϕ*-factory*, Frascati Physics Series **43** (2007) 1-38

[11] R. A. Bertlmann, B. C. Hiesmayr, *Strangeness measurements of kaon pairs, CP violation and Bell Inequalities*, Frascati Physics Series **43** (2007) 197-216

[12] G. Venanzoni, *Status of KLOE-2*, CPC(HEP & NP) **33(X)**(2009) 16

[13] G. Amelino-Camelia et al. (KLOE-2 Collaboration), *Technical Design Report of the Inner Tracker for the KLOE-2 experiment*, arXiv:1002.2572v1 (2010)

[14] G. Amelino-Camelia et al. (KLOE-2 collaboration), *Physics with the KLOE-2 experiment at the upgraded DA*Φ*NE*, arXiv:1003.3868v3 (2010)

[15] F. Ambrosino et al. (KLOE Collaboration), *First observation of quantum interference in the process $\phi \to K_S K_L \to \pi^+\pi^-\pi^+\pi^-$: A test of quantum mechanics and CPT symmetry*, Physics Letters **B 642** (2006) 315-321

[16] A. Di Domenico (KLOE Collaboration), *CPT Symmetry and Quantum Mechanics Tests in the Neutral Kaon System at KLOE*, Foundations of Physics **40** (2010) 852-866

[17] A. Einstein, B. Podolsky, N. Rosen, *Can quantum mechanical description of physical reality be considered complete?*, Phys. Rev. **47** (1935) 777

[18] Particle Data Group: http://pdg.lbl.gov/2009/reviews/rpp2009-rev-phys-constants.pdf

[19] KLOE web page: http://www.lnf.infn.it/kloe

[20] M. Testa, Ph. D. Thesis, Universita degli Studi di Roma "La Sapienza" (2005)

[21] S. Bocchetta, Diploma Thesis, Universita Di Roma Tre (2006)

[22] J. Zdebik, Master Thesis, Jagiellonian University, arXiv:0811.1377v1 (2008)

[23] S. Boccheta, Ph. D. Thesis, Universita Di Roma Tre (2009)

[24] T. Twarog, Diploma Thesis, Jagiellonian University (2010)

[25] R. Boni, F. Marcellini, F. Sannibale, M. Vescovi, G. Vignola, *Dafne LINAC Operational Performance*, Frascati (1998)

[26] F. Sannibale, M. Vescovi, R. Boni, F. Marcellini, G. Vignola: *Dafne LINAC commissioning results*, DAFNE technical note nr BM-2, Frascati (1997)

[27] J. Lee-Franzini, P. Franzini, *A Flavor of KLOE*, Frascati (2007)

[28] P. Franzini, M. Moulson, *The Physics of DAΦNE and KLOE*, arXiv:hep-ex/0606033v2 (2006)

[29] M. Adinolfi et al. (KLOE collaboration), *The tracking detector of the KLOE experiment*, Nucl. Instrum. Methods **A 488** (2002) 51

[30] M. Adinolfi et al. (KLOE collaboration), *The KLOE electromagnetic calorimeter*, Nucl. Instrum. Methods **A 482** (2002) 364

[31] Danilo Domenici, *The upgrade of the KLOE detector: KLOE2*, Frascati Physics Series **44** (2007)

[32] S.Cerioni, *Inner Tracker, Layout-Integration-Installation study*, KLOE-2 General Meeting INFN-Bari (2009)

[33] A. Pais, O.Piccioni, *Note on the decay and absorption of the θ^0*, Physical Review **100** (1955) 1487

[34] R. H. Good et al., *Regeneration of neutral K mesons and their mass difference*, Physical Review **124** (1961) 1223

[35] Roger G. Newton, *Optical theorem and beyond*, American Journal of Physics **44** (1976) 639

[36] K. Kleinknecht, $K_L - K_S$ *regeneration*, Fortschritte der Physik **21** (1973) 57

[37] F. Ceradini, A. Di Domenico, A. Ferrari, *Measurement of neutral kaon regeneration cross sections in the first month of KLOE data taking*, KLOE memo N.169/98 (1998)

[38] R. Baldini, A. Michetti, K_L *interactions and* K_S *regeneration in KLOE*, KLOE note LNF-96/008 (IR) (1996)

[39] E.P. Solodov (CMD-2 collaboration), *Study of the rare* K^0_S, K^0_L, K^+, K^- *decays at* ϕ *resonance with the CMD-2 detector*, Proceedings at 29th International Conference on High-Energy Physics (ICHEP 98), World Scientific (1998)

[40] S. Di Falco, *The* K^0_L *tagging algorithm*, KLOE memo N.173 (1998)

[41] M. Antonelli et al., *Measurements of the Absolute Branching Ratios for Dominant* K_L *Decays, the* K_L *Lifetime, and* V_{us} *with the KLOE Detector*, KLOE Memo N.302 (2005)

[42] F. Ambrosino et al., *Data handling, reconstruction, and simulation for the KLOE experiment*, Nucl. Instrum. Methods **A534** (2004) 403–433

[43] R. Barlow, C. Beeston, *Fitting using finite Monte Carlo samples*, Computer Physics Communications **77** (1993) 219-228